

THERMAL ANALYSIS, PHASE EQUILIBRIA, AND SUPERCONDUCTING
PROPERTIES IN MgB_2 AND CARBON DOPED MgB_2

DISSERTATION

Presented in Partial Fulfillment of the Requirements for the Degree Doctor of Philosophy
in the Graduate School of The Ohio State University

By

Scot David Bohnenstiehl

Graduate Program in Materials Science and Engineering

The Ohio State University

2012

Dissertation Committee:

Dr. Michael D. Sumption, co-advisor

Dr. Suliman Dregia, co-advisor

Dr. John Morral

Copyright by
Scot David Bohnenstiehl
2012

ABSTRACT

In this work, the low temperature synthesis of MgB_2 from Mg/B and MgH_2/B powder mixtures was studied using Differential Scanning Calorimetry (DSC). For the Mg/B powder mixture, two exothermic reaction events were observed and the first reaction event was initiated by the decomposition of Mg(OH)_2 on the surface of the magnesium powder. For the MgH_2/B powder mixture, there was an endothermic event at ~ 375 °C (the decomposition of MgH_2 into H_2 and Mg) and an exothermic event ~ 600 °C (the reaction of Mg and B). The Kissinger analysis method was used to estimate the apparent activation energy of the Mg and B reaction using DSC data with different furnace ramp rates.

The limitations of MgB_2 low temperature synthesis led to the development of a high pressure induction furnace that was constructed using a pressure vessel and an induction heating power supply. The purpose was to not only synthesize more homogeneous MgB_2 samples, but also to determine whether MgB_2 melts congruently or incongruently. A custom implementation of the Smith Thermal Analysis method was developed and tested on aluminum and AlB_2 , the closest analogue to MgB_2 . Measurements on MgB_2 powder and a high purity Mg/B elemental mixture confirmed that MgB_2 melts incongruently and decomposes into a liquid and MgB_4 at ~ 1445 °C at 10

MPa via peritectic decomposition. Another measurement using a Mg/B elemental mixture with impure boron suggested that ~0.7 wt% carbon impurity in the boron raised the incongruent melting temperature to ~1490-1500 °C.

Lastly, the solubility limit for carbon in MgB₂ was studied by making samples from B₄C and Mg at 1530 °C, 1600 °C and 1700 °C in the high pressure furnace. All three samples had three phases: Mg, MgB₂C₂, and carbon doped MgB₂. The MgB₂C₂ and carbon doped MgB₂ grain size increased with temperature and the 1700 °C sample had needle-like grains for both phases. The presence of the ternary phase, MgB₂C₂, suggested that the maximum doping limit for carbon in MgB₂ had been reached. The 1530 °C sample was characterized by Electron Probe Microanalysis at the University of Oregon and the average carbon concentration was estimated to be ~5.9 at%. Further investigation using TEM found MgO inclusions in the 1530 °C sample which were not detected with X-ray diffraction.

ACKNOWLEDGEMENTS

I would like to thank Dr. Sumption and Dr. Collings for their advice and support along with the Office of High Energy Physics at the U.S. Department of Energy for providing the funding under Grant Number DE-FG02-95ER40900. Much appreciation also goes to my co-workers in the lab who have been very helpful and were always ready to assist with the high pressure furnace. I would also like to thank Henk Colijn, Cameron Begg, Dan Huber, Steve Bright, Ross Baldwin and Ken Kushner. This dissertation would also not have been possible without my fiancé, Kelly, who has been very supportive throughout the entire process. Last but not least, I would like to thank Dr. Dregia for his advice, criticism, and skepticism. He has been invaluable to me both personally and professionally.

VITA

- 2004B. S. Metallurgical & Materials
Engineering, Montana Tech of the
University of Montana
- 2008M. S. Materials Science & Engineering, The
Ohio State University
- 2008 to presentGraduate Research Associate, Department
of Materials Science and Engineering, The
Ohio State University

Publications

S. D. Bohnenstiehl, M. A. Susner, Y. Yang, E. W. Collings, M. D. Sumption, M. A. Rindfleisch and R. Boone, "Carbon Doping of MgB₂ by Toluene and Malic-Acid-in-Toluene," *Physica C*, vol. 471, pp. 108-111, 2011.

S. D. Bohnenstiehl, M. D. Sumption, M. Majoros, M. Tomsic, M. Rindfleisch, J. Phillips, J. Yue, E. W. Collings, "Wind and React MgB₂ Rotor Coils," *AIP Conference Proceedings*, vol. 986, pp. 382 – 387, 2008.

S. D. Bohnenstiehl, S. A. Dregia, M. D. Sumption and E. W. Collings, "Thermal Analysis of MgB₂ Formation," *IEEE Transactions on Applied Superconductivity*, vol. 17 (2, Pt. 3), pp. 2754-2756, 2007.

M. D. Sumption, S. D. Bohnenstiehl, F. Buta, M. Majoros, S. Kawabata, M. Tomsic, M. Rindfleisch, J. Phillips, J. Yue and E. W. Collings, "Wind and react and react and wind MgB₂ solenoid, racetrack and pancake coils," *IEEE Transactions on Applied Superconductivity*, vol. 17 (2, Pt. 2), pp. 2286-2290, 2007.

M. Bhatia, M. D. Sumption, S. D. Bohnenstiehl, S. A. Dregia, E. W. Collings, M. Tomsic and M. A. Rindfleisch, "Superconducting Properties of SiC Doped MgB₂ Formed Below and Above Mg's Melting Point," *IEEE Transactions on Applied Superconductivity*, vol. 17 (2, Pt. 3), pp. 2750-2753, (2007).

M. D. Sumption, M. Bhatia, F. Buta, S. D. Bohnenstiehl, M. Tomsic, M. A. Rindfleisch, J. Yue, J. Phillips, S. Kawabata and E. W. Collings, "Multifilamentary MgB₂-based solenoidal and racetrack coils," *Physica C*, vol. 458, pp. 12-20, 2007.

M. D. Sumption, M. Bhatia, F. Buta, S. D. Bohnenstiehl, M. Tomsic, M. A. Rindfleisch, J. Yue, J. Phillips, S. Kawabata and E. W. Collings, "Solenoidal coils made from monofilamentary and multifilamentary MgB₂ strands," *Superconducting Science and Technology*, vol. 18, pp. 961-965, 2005.

Fields of Study

Major Field: Materials Science and Engineering

TABLE OF CONTENTS

ABSTRACT.....	i
ACKNOWLEDGEMENTS.....	iii
VITA.....	iv
LIST OF TABLES.....	ix
LIST OF FIGURES.....	x
CHAPTER 1: REVIEW OF MgB ₂	1
1.1 Structure and Bonding.....	1
1.2 Superconducting and Normal State Properties.....	3
1.3 Mg-B Phase Diagram.....	4
1.4 Synthesis.....	9
1.4.1 Filament Synthesis.....	9
1.4.2 Bulk Samples.....	11
1.4.3 Thin Films.....	13
1.4.4 Single Crystals.....	14
1.5 Doping.....	15

CHAPTER 2: CHARACTERIZATION TECHNIQUES.....	20
2.1 X-ray Diffraction.....	20
2.2 Scanning Electron Microscopy and Transmission Electron Microscopy	21
2.3 Electron Probe Microanalysis (EPMA).....	22
2.4 Vibrating Sample Magnetometry	22
2.5 A.C. Susceptibility	23
CHAPTER 3: DSC OF LOW TEMPERATURE MgB ₂ FORMATION.....	24
3.1 Description of DSC Apparatus.....	24
3.2 DSC of MgB ₂ Formation from Mg and B.....	27
3.2.1 Mg Surface Oxidation Investigation.....	30
3.3 DSC of MgB ₂ Formation from MgH ₂ and B.....	33
3.4 Kinetic Analysis of MgH ₂ /B reaction	36
3.5 Limitations of Low Temperature Synthesis	39
CHAPTER 4: DETERMINATION OF THE INCONGRUENT MELTING TEMPERATURE OF MgB ₂	41
4.1 Description of High-Pressure High-Temperature Furnace	41
4.2 Smith Thermal Analysis Implementation	48
4.3 Smith Thermal Analysis of Aluminum	51
4.4 Smith Thermal Analysis of AlB ₂	54

4.5 Smith Thermal Analysis of MgB ₂	58
4.6 Thermal Analysis of Mg-B Mixtures	65
4.6.1 High Purity Boron	65
4.6.2 Low Purity Boron	71
4.7 A.C. Susceptibility	79
4.8 Environmental Degradation of MgB ₂ Ingots	80
CHAPTER 5: HOMOGENEOUS CARBON DOPING OF MgB ₂	84
5.1 Synthesis.....	84
5.2 Microstructure	85
5.3 Superconducting Properties.....	93
SUMMARY AND CONCLUSIONS	101
APPENDIX A: SMITH THERMAL ANALYSIS PROTOCOL	104
APPENDIX B: STANDARD RAMP/DWELL/COOL PROTOCOL.....	107
LIST OF REFERENCES	108

LIST OF TABLES

Table 1. EPMA data on MgB ₄ Phase.....	76
Table 2. EPMA data on MgB ₂ Phase.....	77
Table 3. Measured Peritectic Temperatures for MgB ₂	78
Table 4. EPMA data on MgB ₂ C ₂	89
Table 5. EPMA data on Mg(B _{1-x} C _x) ₂	89

LIST OF FIGURES

Figure 1. MgB ₂ structure with Mg (light) and B (dark) viewed along <i>c</i> axis (top) and <i>a</i> axis (bottom) [5] (reproduced with permission from the American Physical Society).	2
Figure 2. Mg-B Phase Diagrams for 1, 10, and 100 MPa [39] (reproduced with permission from Elsevier).....	8
Figure 3. Partially reacted boron fibers that were in liquid Mg at 1000 °C for 1 min. (a), 2 min. (b), 3 min. (c), and 5 min. (d) [41] (reproduced with permission from Elsevier)	10
Figure 4. <i>T_c</i> of Doped MgB ₂ Single Crystals [59] (reprinted with permission from Elsevier).....	17
Figure 5. TA Instruments DSC 2920 (reproduced with permission of TA Instruments) .	25
Figure 6. Melting transition of lead (99.99%) at various ramp rates.....	26
Figure 7. DSC run of Mg/B powder mixture at 10 °C/min.	28
Figure 8. DSC run of Mg powder at 10 °C/min. with 425 °C event (inset)	29
Figure 9. Exothermic events in decomposed MgH ₂ after air exposure	31
Figure 10. XRD of MgH ₂ Powder	32
Figure 11. XRD of MgH ₂ after decomposition.....	33
Figure 12. DSC of MgH ₂ /B powder mixture and various ramp rates.....	35
Figure 13. X-ray Diffraction of MgB ₂ from MgH ₂ /B powder mixture after DSC run.....	36
Figure 14. Kissinger Analysis of MgB ₂ Formation	38
Figure 15. Fracture SEM Image of MgB ₂ PIT wire reacted at 700 °C for 0.5 hr.....	40
Figure 16. Pressure Vessel and Lepel 5 kW Power Supply.....	43

Figure 17. Water cooled copper coil for induction heating	44
Figure 18. Susceptor Assembly (only one thermocouple shown)	46
Figure 19. Susceptor Assembly	47
Figure 20. STA run on aluminum.....	52
Figure 21. STA run on aluminum with derivative.....	54
Figure 22. Al-B phase diagram [99] (reproduced with permission from Elsevier).....	55
Figure 23. STA run on AlB ₂ powder	57
Figure 24. STA run on AlB ₂ powder with derivative	58
Figure 25. STA run on MgB ₂ powder with derivative.....	60
Figure 26. STA run on MgB ₂ powder with derivative (enlarged)	61
Figure 27. Microstructure of MgB ₂ ingot after STA run	62
Figure 28. X-ray Diffraction of MgB ₂ Ingot from STA run.....	64
Figure 29. Programmed Run for Mg/B Elemental Mixture with High Purity Boron.....	66
Figure 30. Programmed Run for Mg/B Elemental Mixture with derivative.....	67
Figure 31. Backscatter SEM Image of Mg/B Ingot (dark cores are MgB ₄)	69
Figure 32. X-ray Diffraction of Mg/B Ingot with High Purity Boron	70
Figure 33. Programmed run of Mg/B elemental mixture with low purity boron	72
Figure 34. Programmed run of Mg/B elemental mixture with low purity boron and derivative.....	73
Figure 35. Backscatter SEM Image of Mg/B ingot with low purity boron	74
Figure 36. X-ray Diffraction of Mg/B Ingot with Low Purity Boron.....	75
Figure 37. Location of EPMA Electron Beam (MgB ₄ core)	76

Figure 38. Location of EPMA Electron Beam (MgB_2)	77
Figure 39. A.C. Susceptibility of all three ingots	80
Figure 40. Environmental degradation of Mg/B ingot from low purity boron.....	81
Figure 41. A.C. Susceptibility (real) of original ingot and pested powder (1000 Hz and 10 Oe applied field)	82
Figure 42. A.C. Susceptibility (imaginary) of original ingot and pested powder (1000 Hz and 10 Oe applied field).....	83
Figure 43. 1530 °C sample with $\text{Mg}(\text{B}_{1-x}\text{C}_x)_2$ (grey) and MgB_2C_2 (dark).....	86
Figure 44. 1600 °C sample with Mg (white), $\text{Mg}(\text{B}_{1-x}\text{C}_x)_2$ (grey) and MgB_2C_2 (dark)....	87
Figure 45. 1700 °C sample with Mg (white), $\text{Mg}(\text{B}_{1-x}\text{C}_x)_2$ (grey) and MgB_2C_2 (dark)....	87
Figure 46. X-ray Diffraction of 1530 °C Ingot.....	88
Figure 47. Location of EPMA Electron Beam for MgB_2C_2 and $\text{Mg}(\text{B}_{1-x}\text{C}_x)_2$	90
Figure 48. TEM image of sample from 1530 °C Ingot (HAADF)	91
Figure 49. Oxide Inclusion in TEM.....	92
Figure 50. EDS Analysis of MgO Inclusion.....	92
Figure 51. A.C. Susceptibility (real) of 1700 °C Ingot.....	96
Figure 52. A.C. Susceptibility (imaginary) of 1700 °C Ingot.....	97
Figure 53. VSM M-H loop of 1700 °C Ingot	98
Figure 54. VSM M-H loop of 1700 °C Ingot (zoom).....	99
Figure 55. Upper Critical Field of Carbon Doped MgB_2 and pure MgB_2	100

CHAPTER 1: REVIEW OF MgB₂

In 2001, MgB₂ was discovered to be a superconductor with a T_c of 39 K which has resulted in a tremendous effort towards using the material in superconducting applications [1]. Unfortunately, this material has several processing problems that have made it difficult to obtain sufficient connectivity and homogeneity necessary for many conductor applications. This chapter will review the structure, properties, synthesis and doping of MgB₂ along with the Mg-B phase diagram.

1.1 Structure and Bonding

Magnesium diboride was originally labeled Mg₃B₂ until the compound was reanalyzed in 1954 and the correct stoichiometry was determined to be MgB₂ [2-3]. The crystal structure can be described as hexagonal boron layers intercalated with magnesium atoms (Fig. 1), and the asymmetric unit cell consists of magnesium at (0,0,0) and boron at (1/3, 2/3, 1/2) and (2/3, 1/3, 1/2). It has the same space group as most diborides (*P6/mmm*) with lattice parameters of $a=0.3085$ nm and $c=0.3521$ nm. No structural transformations have been reported under temperature or pressure. However, at very high pressure (190 GPa), it has been predicted that an orthorhombic structure would be more stable, but this has not been confirmed [4].

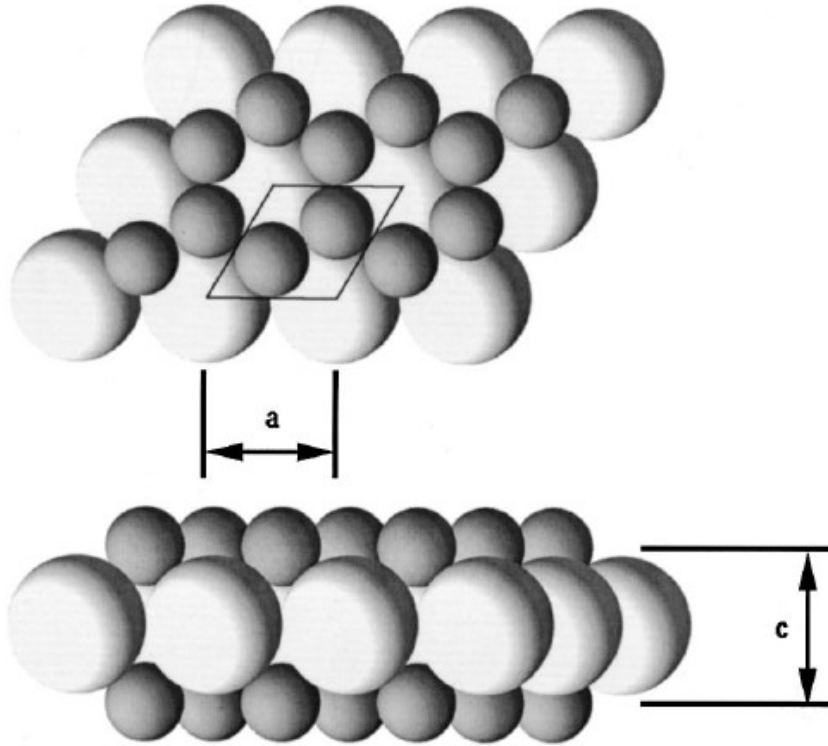


Figure 1. MgB_2 structure with Mg (light) and B (dark) viewed along c axis (top) and a axis (bottom) [5] (reproduced with permission from the American Physical Society).

Electronic structure calculations predicted that the boron-boron bonds would be substantially covalent, but the magnesium-boron bonds would be more ionic [6–9]. This prediction was substantiated by single crystal diffraction data where difference Fourier maps indicated a high electron density between the boron atoms and a reduced electron density around the magnesium atoms [10]. The hexagonal boron layers are similar to graphite where hybrid sp^2 orbitals form in the plane leading to strong covalent bonding. In addition, the B p_z orbitals along the c axis create a π bond similar to graphite.

1.2 Superconducting and Normal State Properties

The most likely mechanism for superconductivity in MgB₂ is an electron-phonon interaction at low temperatures. This is supported by T_c measurements on MgB₂ synthesized from different boron isotopes: ¹¹B (T_c of 39 K) and ¹⁰B (T_c of 40 K) [11]. Boron has a natural isotopic composition of 80% ¹¹B and 20% ¹⁰B, so MgB₂ made from natural boron has a T_c near the ¹¹B value (39 K). The increase in T_c with the lighter boron isotope suggests that some phonon mode in the boron layer is responsible for the high T_c . One particular phonon mode that has been identified as contributing to the high T_c is the E_{2g} mode which is a stretching of 2-D boron network in the plane [12].

The hexagonal symmetry implies that many material properties are anisotropic including the thermal expansion coefficient and electrical resistivity (both larger along the c axis) [5], [13]. For superconducting applications, the most important anisotropic property is the upper critical field, B_{c2} which is lower if the field is oriented parallel to the c axis (3.5 T) compared to orthogonal to the c axis (17 T) [14–17]. Unfortunately, this B_{c2} anisotropy affects polycrystalline samples that have a random grain orientation with respect to magnetic field [18]. This can lead to percolation phenomena since those grains that are oriented with the c axis nearly orthogonal to the magnetic field will still be superconducting even when most other grains are non-superconducting.

The highest measured upper critical field has been used to estimate a coherence length $\xi = 4$ nm near 0 K [19]. The unit cell dimensions of MgB₂ are approximately 10

times smaller than 4 nm so the superconducting properties should not be affected by grain boundaries, at least at low temperatures.

1.3 Mg-B Phase Diagram

The Mg-B phase diagram is not well known due to the volatility of magnesium in comparison to boron. Although magnesium melts at 650 °C and boils at 1100 °C, boron does not even melt until 2092 °C. Also, all of the known compounds in the Mg-B system are stable well beyond the magnesium boiling point. This makes it very difficult to manufacture homogeneous dense samples since it is not possible to use any melting process. It is also not possible to use traditional thermal analysis methods such as Differential Thermal Analysis (DTA) or Differential Scanning Calorimetry (DSC) which usually only operate at standard pressure (0.1 MPa). There are high pressure DTA/DSC instruments, but they are limited in temperature to a few hundred degrees. Thus most of the data on this system has come from magnesium/boron mixtures that were sealed in refractory metal containers (typically tantalum) and reacted at high temperature.

The compounds that are known to be stable at room temperature are MgB₂, MgB₄, MgB₇, and possibly MgB₁₂ or MgB₂₀. The MgB₂ structure has already been discussed. The MgB₄ structure is orthorhombic and was solved using single crystal data [20]. The MgB₇ structure, also known as Mg₂B₁₄, is also orthorhombic [21-22]. Although MgB₂, MgB₄ and MgB₇ are accepted as part of the Mg-B phase diagram, the compounds richer in boron are uncertain. Adasch et al. were successful in growing a single crystal of

MgB₁₂ in a Cu-B-Mg melt contained in a BN crucible, but they noted that MgB₇ and MgB₂₀ were also present [23]. Brutti et al. reported that they were unsuccessful in synthesizing MgB₁₂ and instead obtained MgB₇ and MgB₂₀ [24]. They proposed a structure for the MgB₂₀ compound based on Rietveld refinement of powder diffraction data. The structure is very similar to pure boron and may represent a solid solution of magnesium in pure boron. This compound could be the same as a single crystal recently grown with the composition MgB_{17.4} [25]. It also has a structure very similar to pure boron. Other proposed boron rich phases include Mg₂B₂₅ [26] and Mg₅B₄₄ [21]. Since the boron-rich phases are unconfirmed and not relevant for MgB₂, only MgB₄ and MgB₇ will be discussed further.

There have been claims that MgB₂ is stable over a range of compositions from stoichiometric to magnesium-poor [27–29]. Serquis et al. claimed that MgB₂ is stable with up to 5% vacancies on the Mg site resulting in T_c decreasing from 39 K to 37 K [29]. However, Hinks et al. prepared a series of magnesium-rich and magnesium-poor samples but did not detect any significant change in lattice parameters or superconducting properties [30]. This discrepancy may be due to boron purity issues or perhaps inhomogeneous samples. Of course, it is possible that at very high temperatures there may be a range of compositional stability, but at the present time all the magnesium borides are considered to be line compounds. For MgB₂, this means that if the sample is completely homogeneous, the overall composition will be either magnesium-rich or magnesium-poor since it is very difficult to prepare a line compound with the exact stoichiometric composition.

Most of the thermodynamic data on the Mg-B system has come from vapor pressure measurements using Knudsen effusion cell methods [31]. For this technique, the sample is put in a refractory container with a small hole in the lid and the whole assembly rests in a vacuum furnace. If the hole in the lid is small enough, then molecular flow conditions will ensure that the vapor in the cell is in thermodynamic equilibrium with the sample. The vapor pressure can be measured as a function of temperature and thus thermodynamic data can be collected. Brutti et al. measured the magnesium vapor pressure over several pre-reacted Mg-B mixtures using Knudsen Cell Mass Spectroscopy [32–34]. They collected data on an $\text{MgB}_2/\text{MgB}_4$ mixture between 600–850 °C since the pressure range of the instrument was limited to 10^{-11} - 10^{-4} bar. Based on an extrapolation of their data, they predicted that the decomposition temperature for MgB_2 at 0.1 MPa (standard pressure) would be 1615 °C with the overall formula $2\text{MgB}_2 = \text{MgB}_4 + \text{Mg}_{\text{vapor}}$. Cook et al. also used the Knudsen effusion method, but they measured the rate of mass loss using a thermogravimetric balance [35]. They also collected data on a $\text{MgB}_2/\text{MgB}_4$ mixture over the same temperature range, but their extrapolated decomposition temperature for MgB_2 at 0.1 MPa was 1268 °C, a significantly lower number. It is unclear why such a huge discrepancy exists, but it could be related to boron purity issues. Brutti et al. used 99.7% pure boron for their $\text{MgB}_2/\text{MgB}_4$ mixture, but Cook et al. used isotopically pure ^{11}B of 99.5% purity. The quoted purities are only for metals and do not include carbon which is known to substitute for boron in the MgB_2 structure and thus possibly influence these results.

Another source of thermodynamic data for the Mg-B system has been measurements on the enthalpy of formation of MgB_2 via isoperibol solution calorimetry. This measurement consists of dissolving MgB_2 in acid, measuring the increase in heat, and using a Hess cycle with data on dissolution of Mg and B to establish the difference as the heat of formation of MgB_2 . Of course, this method has the problem that the final data is only as reliable as the measurement on pure magnesium and boron. Cook et al. measured the enthalpy of formation of MgB_2 at 298 K to be -155.9 ± 14.2 kJ/mol [35]. This value is significantly higher than the literature value of -74.8 ± 3.8 kJ/mol [36].

Most of the proposed phase diagrams in the literature are based on computational predictions or extrapolations of experimental data to higher temperatures [33], [35], [37–39]. Given the disagreement in the experimental data, it is difficult to evaluate these phase diagrams without further information. The most extensive set of phase diagrams based on computational predictions are by Kim et al. [39] who predicted several Mg-B phase diagrams for different pressures (Fig. 2). They used density functional theory calculations to estimate the formation enthalpy of Mg-B compounds and combined that data with thermodynamic software to predict phase diagrams for 1 MPa, 10 MPa and 100 MPa. For 10 MPa, they predicted that MgB_2 melts incongruently into MgB_4 and a liquid at ~ 1740 °C. Their predicted phase diagram for 100 MPa is nearly identical suggesting that MgB_2 never melts congruently, even at 100 MPa. This is unfortunate since a congruently melting compound would be ideal for making dense homogeneous samples.

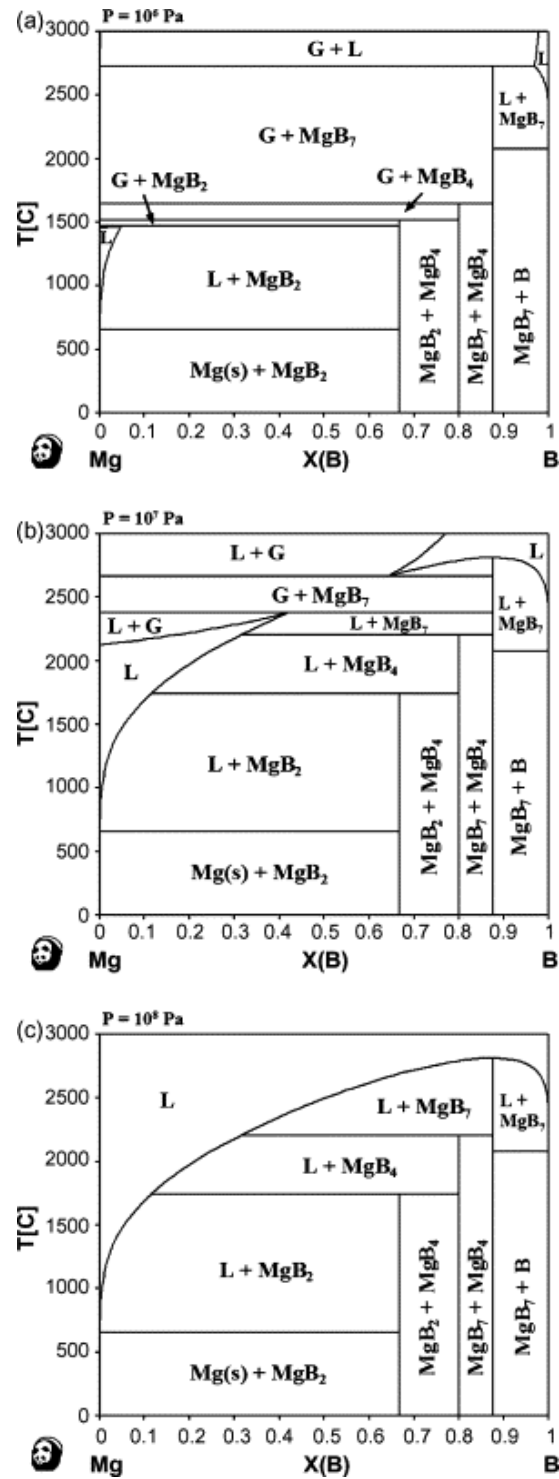


Figure 2. Mg-B Phase Diagrams for 1, 10, and 100 MPa [39] (reproduced with permission from Elsevier)

1.4 Synthesis

There are several synthesis routes that have been developed for MgB_2 including filament synthesis, powder reactions (bulk samples), Hybrid Physical-Chemical Vapor Deposition (HPCVD) for thin films, and high-pressure, high-temperature synthesis for single crystals. Each process has advantages and disadvantages for materials property measurements and applications development.

1.4.1 Filament Synthesis

Soon after MgB_2 was discovered to be superconducting, the synthesis of MgB_2 fibers was attempted by reacting boron fibers (100-200 μm diameter, 99.999% pure) with magnesium vapor in a sealed tantalum tube [40]. The boron fiber was converted to MgB_2 in about two hours at 950 °C, but the product was brittle and had extensive cracking. Although the process is not very useful for applications, it is useful for understanding the reaction progression of magnesium and boron to form MgB_2 .

As the Mg-B phase diagram suggests, the reaction of magnesium with boron will initially form MgB_7 , then MgB_4 , and finally MgB_2 . The formation of each subsequent compound is limited by solid state diffusion through the higher boride and the kinetics at the reaction interface between the higher boride and the lower boride. The best demonstration of this process was reported by DeFouw and Dunand who reacted boron fibers in liquid magnesium for various times and temperatures [41]. Cross sections for the

1000 °C heat treatment for 1, 2, 3 and 5 minutes demonstrate that MgB_7 forms initially on the circumference (Fig. 3). Then MgB_4 and finally MgB_2 progress through cracks around the circumference. These cracks are probably due to the molar volume differences between the boride phases combined with the general lack of ductility of borides. Unfortunately, this means that the reacted filaments are only a loosely connected structure and do not resemble the original continuous boron fiber.

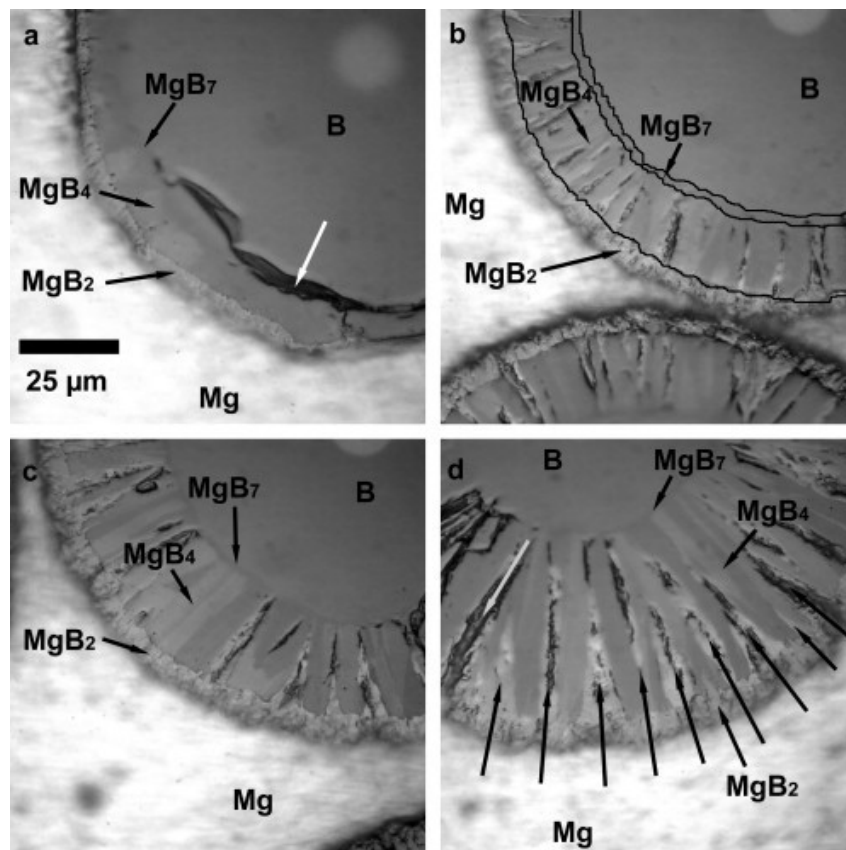


Figure 3. Partially reacted boron fibers that were in liquid Mg at 1000 °C for 1 min. (a), 2 min. (b), 3 min. (c), and 5 min. (d) [41] (reproduced with permission from Elsevier)

1.4.2 Bulk Samples

Most of the literature on MgB_2 is based on samples made from reacted Mg and B powder mixtures. Typically a mixture of micron-size boron powder and magnesium is reacted at 700-900 °C. The main advantage with this method is that the temperatures are far enough below the magnesium boiling point (1100 °C) to avoid significant magnesium vapor loss. This low temperature synthesis method only works if a fine boron powder is used since the kinetics with coarse boron are slow. This method is also common for manufacture of MgB_2 wire where a metal tube (typically iron or niobium) is filled with a Mg/B powder mixture and drawn down to an appropriate diameter (this process is called Powder-in-Tube or PIT wire) [42]. The wire is then heat treated at 700-900 °C to form the MgB_2 inside, but the wire must be in its final shape since MgB_2 is brittle and any movement after heat treatment will break the MgB_2 inside the tube[43]. An alternative is to pre-react the powder mixture and then fill a metal tube with the MgB_2 powder. A heat treatment afterwards can be used to “sinter” the MgB_2 grains to improve connectivity, but it is questionable whether any sintering really occurs [44]. Also, more detailed work on MgB_2 wires and tapes made from Mg/B powder mixtures has identified MgB_4 and MgB_7 inside the MgB_2 [45-46]. This suggests that the reaction is limited and does not go to completion, even with fine powders.

Oxide contamination is a major problem with MgB_2 made from Mg/B powder mixtures. Some of the MgO comes from the surface of the magnesium, but there is also a surface oxide on the boron (B_2O_3) which reacts with Mg to form MgB_2 and MgO [47].

The B_2O_3 can be removed beforehand by reducing it using hydrogen at high temperature but this makes handling more problematic afterwards since re-exposure to air would reform the oxide [48]. Another solution is to use boron with a large particle size, but this leads to slow reaction kinetics as discussed above.

The main difficulty with the powder approach is that it is impossible to achieve a fully dense sample. This is partly due to powder packing limitations, but even if a 100% dense mixture of Mg and B were possible, there would still be 25% porosity after the reaction due to the overall change in molar volume. This has prompted a new synthesis method called Reactive Liquid Magnesium Infiltration by Giunchi [49]. This process consists of packing boron powder around a solid magnesium rod in an iron tube. After packing, the iron tube is welded shut and heated, typically for 1 hr. at 900 °C. The magnesium melts and reacts with the boron to form a solid MgB_2 article of high density. However, it is difficult to make wire with this method so it has not been pursued in depth.

Another problem for the powder synthesis method is that there are a wide range of boron powder purities that have been used for making MgB_2 . This has a strong effect on the superconducting and normal state properties. For example, the Residual Resistivity Ratio (RRR) increased from 4 to 20 as the boron purity increased from 90% to 99.99% [50]. The T_c also improved and the transition to the normal state was more abrupt (ΔT_c decreased). The best superconducting properties are from MgB_2 made from high purity (99%) amorphous boron powder [51]. Unfortunately, the high purity boron is very expensive so lower purity boron is often used. The lower grade boron is manufactured using a mixture of Mg and B_2O_3 that is ignited with a spark to create a self-propagating,

uncontrolled reaction. The products are MgO and B powder along with other phases such as $\text{Mg}_2\text{B}_2\text{O}_5$ and $\text{Mg}_3\text{B}_2\text{O}_6$. The reacted mixture is then crushed and washed with HCl acid to remove MgO and other contaminants. After washing and drying, the boron purity is typically 86%, but it can be upgraded to 95-96% by heating to high temperature under vacuum to remove magnesium. These boron powders are often labeled as “amorphous” although X-ray diffraction indicates there are peaks that match crystalline boron. Unfortunately, much of the literature does not discuss the details of the type of boron that was used to make the MgB_2 making it difficult to evaluate competing claims regarding synthesis, structure, and properties.

A suggestion for making MgB_2 with lower porosity and better homogeneity is to make MgB_4 at high temperature and then react the MgB_4 with magnesium later to form MgB_2 [52]. Unfortunately, this approach still relies on solid state diffusion since the MgB_4 does not melt at low temperature. The slow kinetics of solid state diffusion would make it necessary to use a very fine MgB_4 powder or very long heat treatment schedules so the process would be of questionable value.

1.4.3 Thin Films

The difficulty of producing clean samples with no oxide as discussed above has led to alternative methods of synthesis including the production of MgB_2 thin films via Hybrid Physical Chemical Vapor Deposition (HPCVD) [53–55]. This approach uses diborane gas (B_2H_6) flowing over a heated substrate surrounded by magnesium chips. At

approximately 600 °C, the magnesium vapor reacts with the diborane gas to produce MgB_2 and H_2 . The thin films are epitaxial, have essentially zero oxide contamination, and have the highest RRR values of any MgB_2 produced to date. Carbon doped thin films have also been produced by adding a magnesium organometallic compound to the gas flow [56].

1.4.4 Single Crystals

The growth of MgB_2 single crystals is very challenging due to the volatility of magnesium. The most successful process has been a high pressure synthesis method that uses a geologic apparatus (anvil press) at approximately 1000-3000 MPa (10-30 kbar) and 1700-2200 °C using a graphite heater and pyrophyllite pressure medium [57–61]. The crystals are grown in a ternary Mg-B-N system by containing a Mg-B mixture in a boron nitride container. The Mg-B-N ternary phase diagram is not well known but the phases present after cool down include MgB_2 , BN, and MgNB_9 . The largest single crystals grown to date are platelets approximately 1.5 mm x 1 mm x 0.05 mm and have a T_c of 37-39 K.

The flux growth method has also been attempted using the ternary Mg-B-Cu system since the Cu-B system is a simple eutectic and there are no known Mg-B-Cu compounds [62]. The largest single crystals were 0.2 mm x 0.2 mm x 0.05 mm, but they had a broad superconducting transition temperature. However, for the $\text{Mg}_{30}\text{Cu}_{50}\text{B}_{20}$ composition they obtained MgB_2 surrounding MgB_4 particles which they identified as a

“peritectic rim.” This form of MgB₂ had a sharp T_c onset at 39.1 K and a ΔT_c of 1.3 K suggesting that this form of MgB₂ was much more homogeneous.

1.5 Doping

The low upper critical field for pure MgB₂ is not very useful for many superconducting applications so various approaches have been attempted to increase the upper critical field. One approach has been to dope the material which is based on the Werthamer-Helfand-Hohenberg theory [63]. This theory predicts that the upper critical field can be increased by doping (or alloying) to increase the normal state resistivity so that the mean free path in the normal state becomes less than the coherence length. For MgB₂, this can be accomplished by doping either on the boron site or the magnesium site.

There are several obstacles that make it difficult to synthesize doped MgB₂. Many possible dopants form their own borides instead. For example, the alkaline earth metals (Ca, Sr, and Ba) do not substitute on the Mg site but form hexaborides (CaB₆, SrB₆, and BaB₆). Another possibility is that a ternary phase will be more stable than the doped MgB₂ phase so little or no doping occurs. Even if doping for some given element is possible, it can be difficult to achieve a homogeneous solid solution at the low synthesis temperatures often used (600-900 °C). In much of the literature, a change in some transport property has been used as evidence of doping, but this is problematic since transport measurements are affected by purity, porosity, connectivity, homogeneity, etc. These are all known problems with pure MgB₂ let alone doped MgB₂. Cava et al. has

suggested that X-ray diffraction data be used to demonstrate a change in lattice parameters by more than three standard deviations between the doped specimen and a pure reference sample [64]. However, even if that criteria were satisfied, it can still be difficult to relate changes in superconducting properties to dopant additions if the sample is not homogeneous. For example, an inhomogeneous dopant may mean that there will be a range of T_c values depending on the dopant concentration in each MgB_2 grain. This makes it very problematic to know exactly what effects various dopants may have.

Those difficulties have been partially solved by using the high pressure method to grow doped MgB_2 single crystals [59]. These include carbon doped MgB_2 where carbon substitutes on the boron site and metal doped MgB_2 where Al, Li, Mn, and Fe substitute on the Mg site. All of these additions decrease T_c with increasing concentration but at varying rates (Fig. 4). Manganese decreases T_c considerably due to magnetic pair breaking of the superconducting Cooper pairs. Iron does not seem to have the same effect. Lithium doping is not surprising given the similar size to magnesium. Carbon and aluminum have extensive solubility in the MgB_2 structure, but aluminum decreases T_c at a slightly higher rate. Aluminum doping is not surprising given that AlB_2 and MgB_2 have the same structure and similar lattice parameters. At aluminum concentrations near 50%, an ordered structure forms and the c axis doubles meaning aluminum and magnesium alternate in the structure [65]. Unfortunately, aluminum lowers the upper critical field so it will not be discussed further.

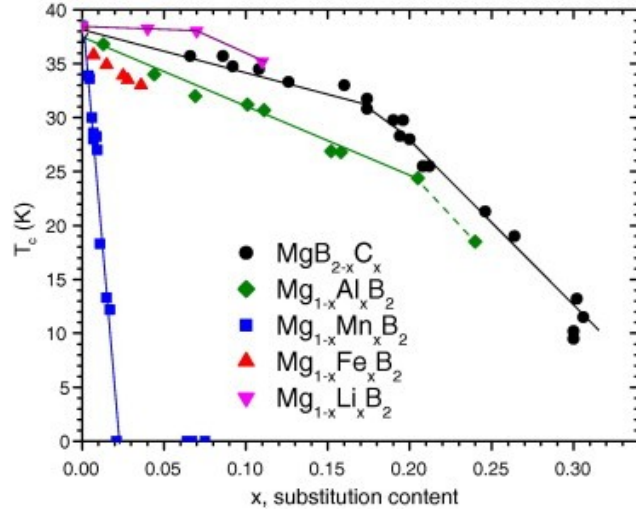


Figure 4. T_c of Doped MgB_2 Single Crystals [59] (reprinted with permission from Elsevier)

It is important to note that although the high pressure route has produced doped single crystals, the doping levels reached at high pressure may not match the doping levels possible at low pressure due to the different thermodynamic conditions. Also, the single crystals were grown in a quaternary system (Mg-B-N-X) at high temperature which may have different phase boundaries than the ternary Mg-B-X system (where X stands for dopant). For example, the solubility limit for carbon in the Mg-B-C system may be different than the solubility limit for carbon in the Mg-B-N-C system. Also, the solubility may change as a function of temperature which means the dopant concentration may change with cooling rate. All of these factors need to be considered before the doped single crystal results are used to interpret lower temperature/pressure samples.

The most studied dopant so far is carbon since it increases the upper critical field. Several methods have been tried to produce homogeneous carbon doped MgB_2 at low

temperatures. One popular approach has been to add nanometer-size SiC powder to the Mg/B powder mixture [66]. On heating, the SiC powder reacts with magnesium to form Mg_2Si and carbon, some of which takes part in the reaction of magnesium and boron to form carbon doped MgB_2 [67]. Alternatives include various organic compounds that are added to the Mg/B powder mixture [68-69]. However, all these additions suffer from the same problem, an inhomogeneous distribution of carbon. One solution has been to use boron carbide (B_4C) powder, but it requires much higher reaction temperatures than amorphous boron [70-71]. Temperatures of at least 1200 °C for 24 hours were required to achieve a sharp superconducting transition temperature of ~22 K. The sample contained four crystalline phases: Mg, MgB_2 , MgB_2C_2 and MgO. The presence of the ternary phase, MgB_2C_2 , suggests that the carbon solubility limit was exceeded for the Mg-B-C system. A carbon doping level of 10% was estimated based on neutron diffraction data but no additional supporting evidence of the carbon doping level was provided.

The production of a boron powder with a controllable amount of dopant has been pursued by Specialty Materials, Inc, the same producers of boron fibers [72]. An argon plasma is used to react a gaseous mixture of BCl_3 , H_2 , and CH_4 . The carbon doped boron powder is recovered from the reactor and HCl scrubbed from the exhaust. Although this approach has been successful at producing more homogeneous carbon doped MgB_2 , the high cost of the BCl_3 precursor makes this approach impractical for any cost-effective application [73].

Another interesting approach is to use two dopants by substituting boron with carbon and magnesium with a metal. This has been successfully achieved with carbon

and lithium in single crystals produced by the high pressure process [74]. Unfortunately, there appears to be no benefit for superconducting properties over that of carbon doped MgB_2 . The use of two dopants has also been attempted with carbon and titanium doped boron fibers [75]. However, only the carbon was an effective dopant since the titanium formed TiB_2 precipitates instead of substituting on the magnesium site in the MgB_2 structure.

CHAPTER 2: CHARACTERIZATION TECHNIQUES

The experimental techniques used for sample characterization included X-ray Diffraction, Electron Probe Microanalysis, Scanning Electron Microscopy, Transmission Electron Microscopy, Vibrating Sample Magnetometry, and A.C. Susceptibility. These techniques will be briefly described here. The thermal analysis techniques will be described in the appropriate chapter.

2.1 X-ray Diffraction

In this technique, a monochromatic X-ray beam strikes a polycrystalline sample that has one or more crystalline phases. The X-rays are diffracted from crystalline planes that satisfy the Bragg condition for coherent scattering ($n\lambda = 2d \sin \theta$ where $n=1,2,3,\text{etc.}$, λ is the X-ray wavelength, d is the crystalline plane spacing and θ is the diffraction angle). A detector registers the angle and intensity of the diffracted X-rays which provides the information for phase identification. All X-ray diffraction data for this dissertation was collected with a Scintag XDS-2000 diffractometer equipped with a Cu X-ray tube (wavelength of 1.54059 Å) operating at 45 kV and 20 mA. This instrument used the Bragg-Brentano geometry where the sample remains stationary, the x-ray source moves through an angle θ and the detector through an angle 2θ . Alignment of the instrument was checked with a LaB_6 powder standard that was NIST traceable. The

Powder Diffraction File (PDF2) database from the International Center for Diffraction Data was used for phase identification.

2.2 Scanning Electron Microscopy and Transmission Electron Microscopy

The Scanning Electron Microscope uses a high vacuum chamber to raster an electron beam over a material and the electrons have enough energy (typically 5-30 kV accelerating voltage) to generate secondary electrons, backscattered electrons, and x-rays which are used for imaging and chemical analysis. The Secondary Electron (SE) detector is used to detect electrons scattered from the sample surface so it is sensitive to topography. If the sample is flat, then backscattered electrons can be used to image compositional differences in the sample since the yield of backscattered electrons is sensitive to the local average atomic number. The X-rays from the sample can be detected with an Energy Dispersive Spectrometer which provides the X-ray energy and intensity of individual elements (EDS detectors are typically not sensitive to light elements such as boron since the X-ray fluorescent yield of boron is very low). The SEM images in this dissertation were collected with a Sirion SEM from FEI, Inc. with a typical accelerating voltage of 10 kV and working distance of 5 mm.

The Transmission Electron Microscope also operates under high vacuum except the electrons are transmitted through a very thin sample (<100 nm). The transmitted electrons are then imaged using a CCD detector, fluorescent plate, or special photographic film (diffraction information can also be recorded). There are several

methods for preparing very thin samples but the method used here was to use a focused ion beam that can carve out a ~4 micron x ~10 micron slice of material which is then thinned to be electron transparent. The TEM images presented here were collected by Henk Colijn on a Tecnai F20 TEM at 200 kV.

2.3 Electron Probe Microanalysis (EPMA)

This technique is similar to Scanning Electron Microscopy except the instrument is optimized for accurate, quantitative chemical analysis of 1-2 micron areas. The electron beam is designed to have high temporal stability so it generates a constant yield of X-rays from a spot on the sample which are then analyzed using a Wavelength-Dispersive Spectrometer (WDS). The WDS typically has better accuracy than the EDS detector used in SEM's and it uses a series of crystals to separate the X-rays by wavelength. There is no functioning EPMA at The Ohio State University so the EPMA data presented in this dissertation was collected by John Donovan at the University of Oregon using a Cameca SX100 EPMA instrument.

2.4 Vibrating Sample Magnetometry

The Vibrating Sample Magnetometer (VSM) measures the magnetic properties of a material by placing the sample in a static magnetic field and vibrating the sample at a fixed frequency near a pick-up coil. An oscillating voltage is induced in the pick-up coil

at the same frequency as the vibration of the sample and a lock-in amplifier it used to extract the signal due to the sample (calibration is used to convert that signal to an absolute value). The VSM data presented here was collected using the VSM option on the Physical Properties Measurement System (PPMS) from Quantum Design, Inc. This instrument was calibrated with a palladium standard at 2 Tesla and 298 K.

2.5 A.C. Susceptibility

The A.C. Susceptibility (or dynamic susceptibility) method is a technique for measuring the time dependent magnetic moment of a sample which can be considered to have a real (in-phase) component and imaginary (out-of-phase) component. A small alternating magnetic field is applied to the sample which may be superimposed on a constant (DC) magnetic field. The small alternating field causes a change in magnetization of the sample which is detected using a pick-up coil surrounding the sample. All A.C. Susceptibility data was collected with a Physical Properties Measurement System (PPMS) from Quantum Design, Inc. with an A.C. field of 10^{-3} Tesla (10 Oersted) at 1000 Hz. All temperature data was collected on heating with a scan rate of 0.5 K/min. after zero-field cooling.

CHAPTER 3: DSC OF LOW TEMPERATURE MgB₂ FORMATION

The low temperature reaction of Mg/B powder mixtures to form MgB₂ has not been studied extensively. There have been reports of two exothermic reactions on heating instead of a single exothermic reaction as might be expected [76–78]. The first exothermic reaction was observed near 500 °C and the second near 600 °C. One or both of these events must involve MgB₂ formation, but it is unclear why there are two exothermic reactions and not one. Thermal analysis using DSC was used to study these reactions and determine what factors influence MgB₂ formation.

3.1 Description of DSC Apparatus

The DSC data in this chapter was collected with a TA Instruments DSC 2920 (Fig. 5). This instrument is a Heat-Flux DSC that uses a constantan (55% Cu – 45% Ni) disk with two raised platforms for both a sample and a reference. Two Chromel¹ disks are welded underneath the platforms with Chromel wires attached. The two Chromel wires are used to measure a voltage that corresponds to a temperature difference between the sample and reference. This temperature difference is converted to a calorimetric quantity using a suitable calibration. Ideally, if there is no temperature difference then the measured voltage is zero, but this is difficult to realize in practice. The sample

¹ Chromel and Alumel are registered trademarks of Hoskins Manufacturing Company

temperature is measured using the Chromel wire, and an additional Alumel wire, underneath the sample platform. A furnace surrounding the constantan disc assembly is used for heating and cooling and it has a separate control thermocouple.

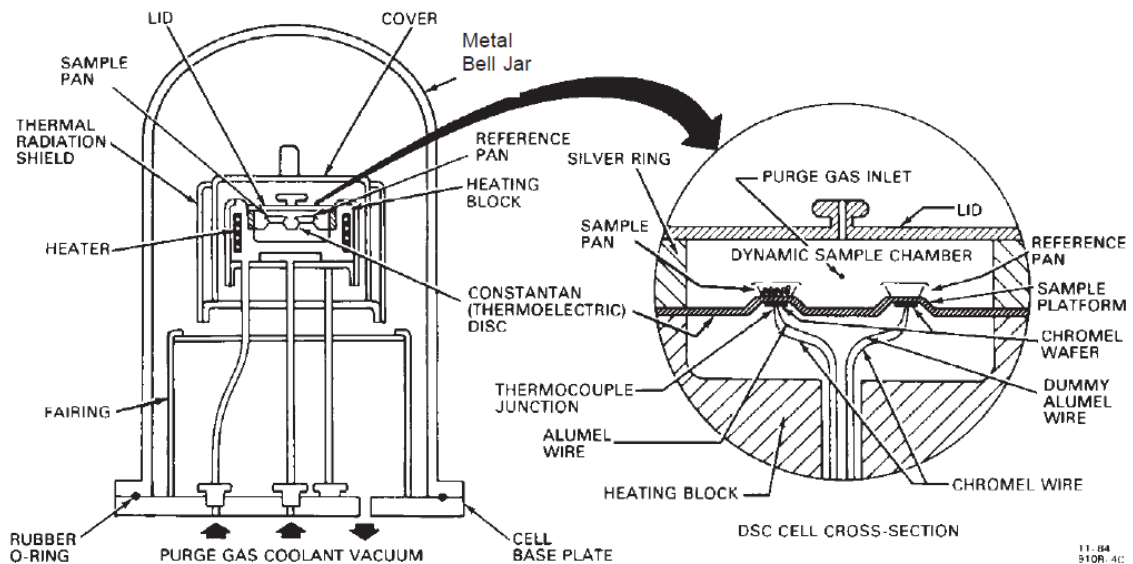


Figure 5. TA Instruments DSC 2920 (reproduced with permission of TA Instruments)

Most thermal analysis equipment has a thermal lag between the sensor and the sample. For the DSC 2920, the sample sits in a pan and lid on top of the thermal sensor which means the pan and sensor affect the heat flow in the instrument. For an exothermic event, heat from the sample must flow through the sample pan and constantan/Chromel junction before a change in the differential voltage is recorded. For an endothermic event, heat must flow through the constantan/Chromel junction and pan before it can affect the differential voltage. In both cases, there is a lag between the sample and the sensor.

The thermal lag constant of a DSC can be measured using the melting transition of a pure metal [79]. For this instrument, DSC data was collected on a 99.99% lead sample at ramp rates of 5, 7.5 and 10 °C/min. (Fig. 6). The melting transition had a clear onset at 327 °C, but the transition was spread over several degrees due to thermal lag. The peak corresponds to melting completion and it shifts to higher temperatures as the ramp rate increases. However, the slope from the onset to the peak remains the same. Based on this slope, the thermal lag constant for this DSC was estimated to be 0.067 K/mW.

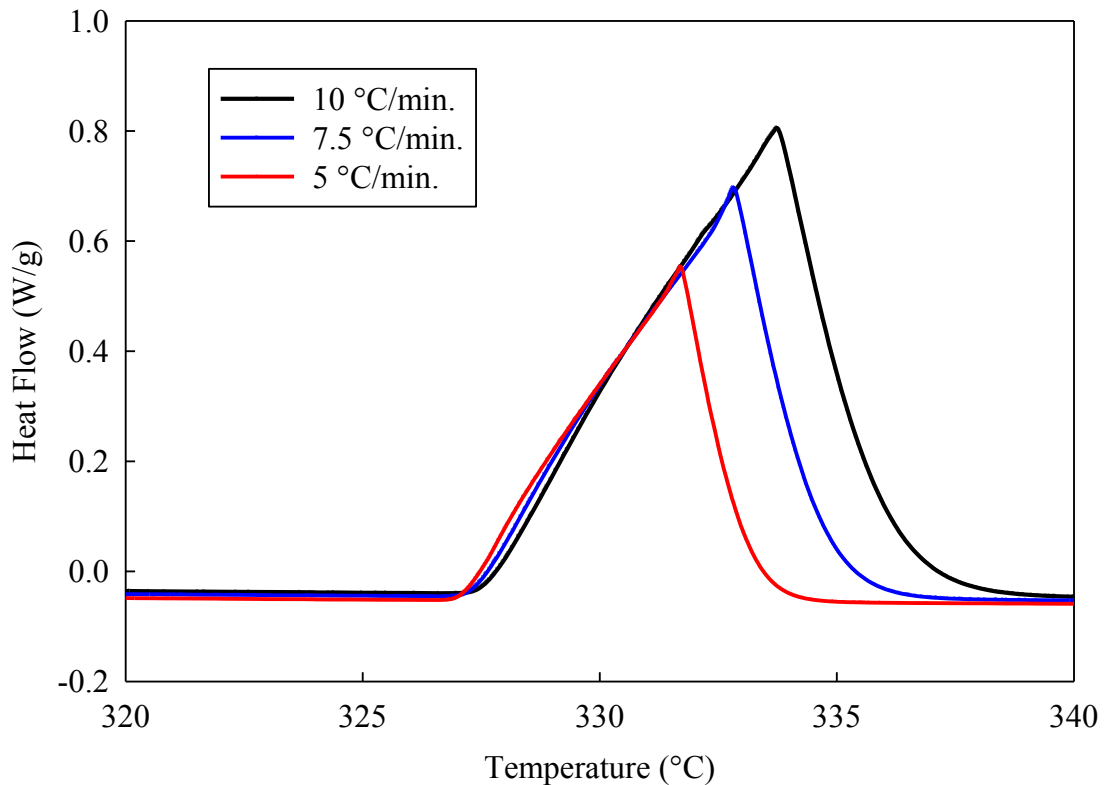


Figure 6. Melting transition of lead (99.99%) at various ramp rates

For this DSC study, iron pans and lids were made from iron foil (0.4 mm thickness) using a custom die since the standard aluminum pans alloy with magnesium (iron pans/lids were also used for the thermal lag measurement). They were matched in dimensions and weight as closely as possible so they would have the same thermal response. Two high purity metals, Pb (99.99%) and Mg (99.98%), were used for the temperature calibration of the DSC and to verify the heat flow calibration. All runs used high purity argon (99.998%) that was passed over titanium chips at 800 °C to remove trace impurities.

3.2 DSC of MgB₂ Formation from Mg and B

The Mg/B samples were made from a high purity amorphous boron powder (99%, Alfa Aesar, sub-micron particle size) since it provided the purest and most reactive form of boron available. The amorphous character of the powder was confirmed by XRD. Magnesium powder (98% pure, Alfa Aesar, -325 mesh) was used as the magnesium source. Both powders were checked for any reaction with the iron pans/lids, but no reactions were observed up to the 725 °C, the limit of the instrument. The powders were weighed in the stoichiometric ratio for MgB₂ formation and milled in a Spex Shaker mill with zirconia ball media. A 20 minute mill followed by a 1 hour cool and another 20 minute mill was used to avoid overheating. The powders were then stored in a dessicator under vacuum with P₂O₅ to avoid moisture contamination until they were used for DSC.

A DSC run of the Mg/B powder mixture had two exothermic events similar to the exothermic events noted in the literature (Fig. 7). The first exothermic event had an onset near 425 °C and the second at approximately 600 °C. The cooling data gave no indication of magnesium solidification which suggested that all the magnesium was consumed in the reaction. Perhaps the most interesting observation is that the reactions were essentially complete before the magnesium melting point of 650 °C. It is possible that the reaction was aided by transport of magnesium vapor, given that magnesium has an unusually high vapor pressure near the melting point (~2 torr) [80].

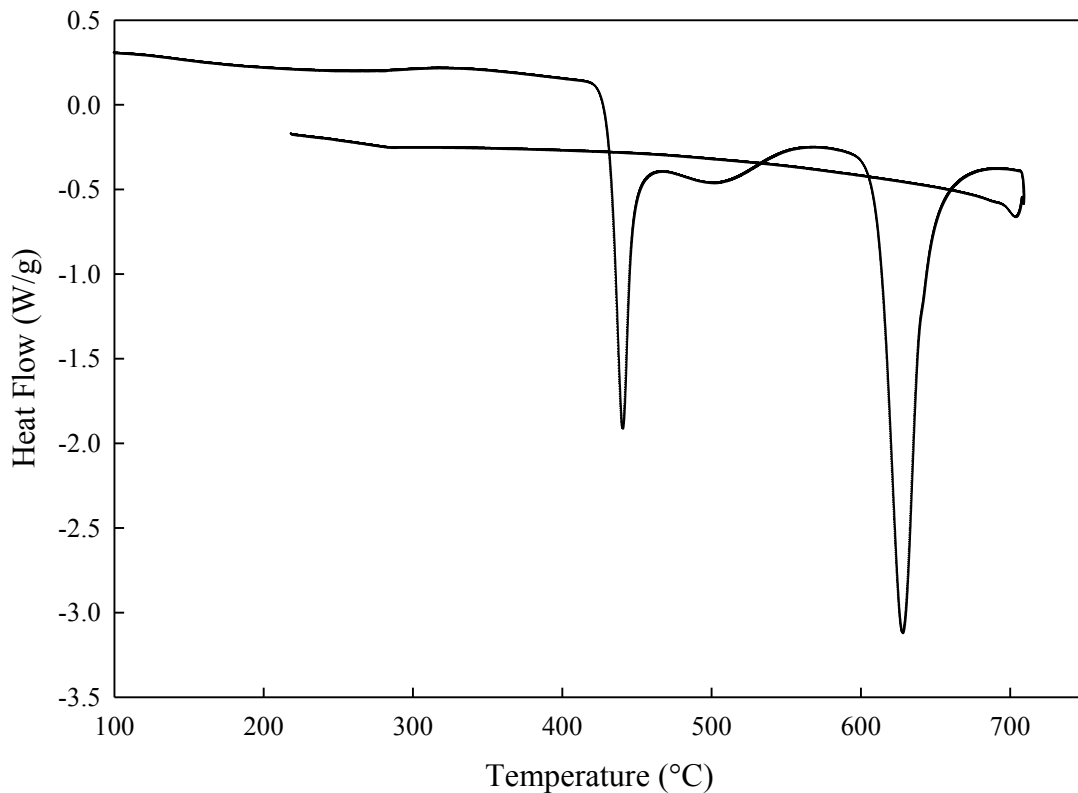


Figure 7. DSC run of Mg/B powder mixture at 10 °C/min.

When the Mg powder was checked for any reaction with the iron pan, it was noticed that besides melting and solidification, there was a small exothermic event near 425 °C (Fig. 8). This event did not reappear on cooling indicating it was some non-reversible event. A reaction with the iron pan was considered unlikely given that magnesium and iron are immiscible which is why iron was selected as a pan material. The proximity of this 425 °C event to the first exothermic event in the Mg/B powder mixture suggested that these two events were related.

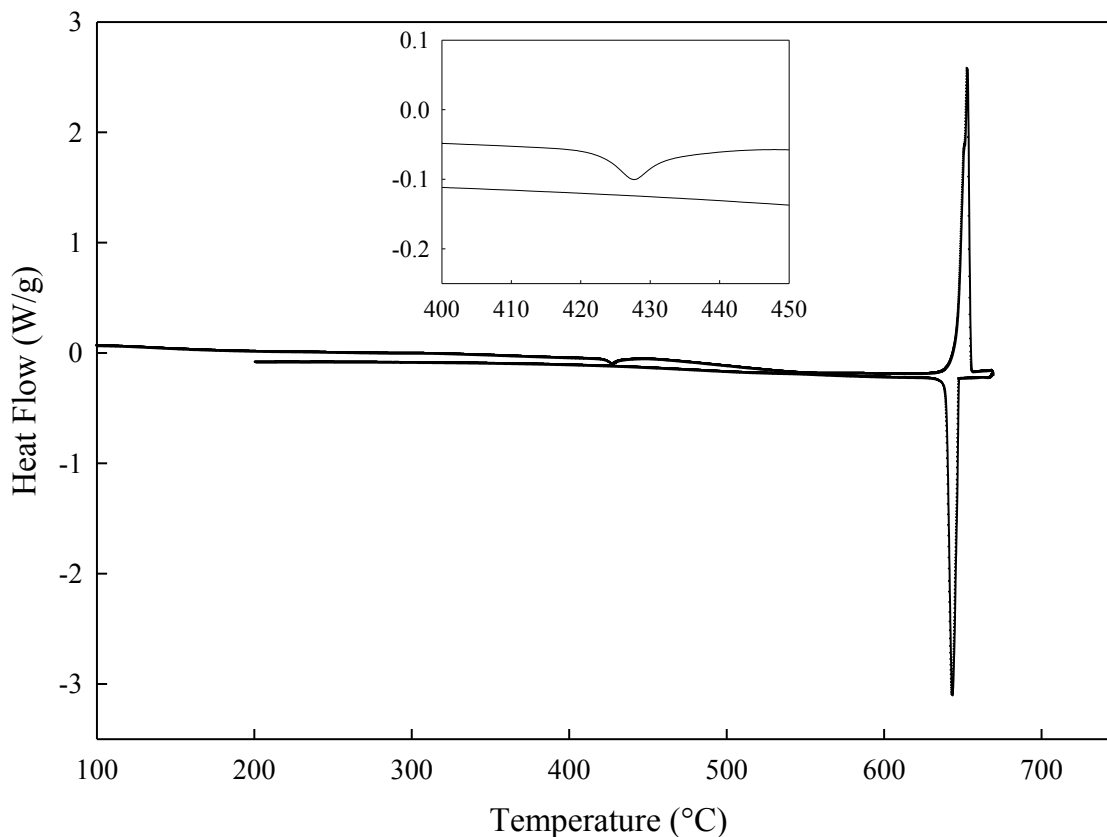


Figure 8. DSC run of Mg powder at 10 °C/min. with 425 °C event (inset)

3.2.1 Mg Surface Oxidation Investigation

One possible origin for the exothermic event in the magnesium powder was some kind of annealing or recrystallization of the powder. To test this idea, some of the magnesium powder was annealed in a sealed stainless steel tube under argon at 600 °C for 1 hour. After cooling to room temperature, the tube was opened and the magnesium powder was run in the DSC again, but the thermal event was still present. The next consideration was that some surface oxidation phenomenon was causing the exothermic event. However, in order to study surface oxidation in metal powders, it is useful to use as fine a powder as possible since the amount of surface oxide will be proportional to surface area. It was decided to try MgH₂ powder which decomposes into Mg and H₂ at approximately 375 °C. This provided a source of Mg powder with high surface area. The MgH₂ was decomposed in the DSC, but no thermal events were observed on cooling.

However, retesting the same sample the next day showed an exothermic event with an onset near 450 °C (Fig. 9). Two more DSC runs on the same sample showed that this event would reappear, although shifted to a higher temperature, if the sample was exposed to air after cooling. These thermal events were not observed if the sample was kept under argon suggesting that this thermal event was related to an oxidation phenomenon. The original magnesium powder was rechecked for this thermal behavior and it also had reproducible exothermic events near 425-450 °C, but only if exposed to air just like the decomposed MgH₂.

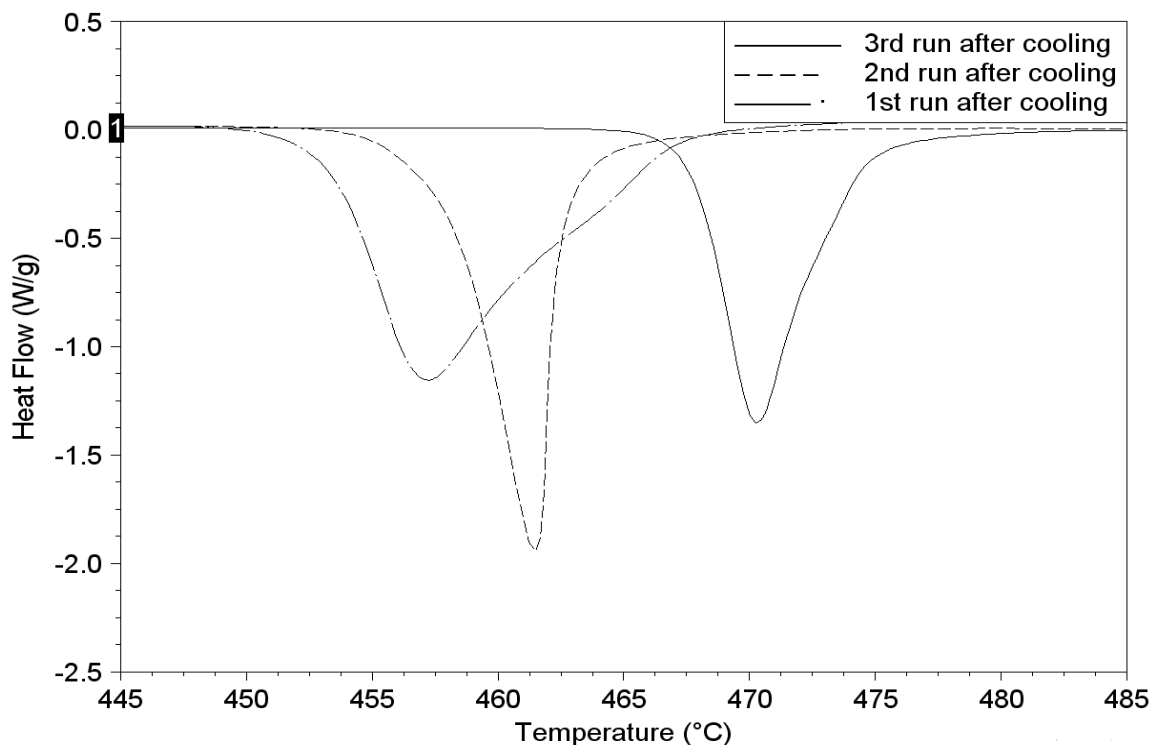


Figure 9. Exothermic events in decomposed MgH_2 after air exposure

Although the air sensitivity of the magnesium powder strongly suggested an oxidation process, it was unclear why the exothermic event would only appear in such a narrow temperature range. An X-ray diffraction (XRD) scan of the magnesium powder gave no indication of any other phases than pure magnesium. However, an XRD scan of the MgH_2 powder showed the presence of MgH_2 , Mg , and $\text{Mg}(\text{OH})_2$ (Fig. 10). The presence of $\text{Mg}(\text{OH})_2$ was unexpected and suggested that the MgH_2 was not properly stored under argon despite the packaging label. An XRD scan of the MgH_2 after decomposition in the DSC showed only the presence of Mg and MgO (Fig. 11) which suggested that $\text{Mg}(\text{OH})_2$ was responsible for these exothermic events. In fact, $\text{Mg}(\text{OH})_2$ is

known to decompose into MgO and H₂O in roughly this temperature range (depending on purity) [81]. Of course, Mg(OH)₂ decomposition is endothermic, not exothermic. The likely reason the events observed in the magnesium powder were exothermic is that the water from the Mg(OH)₂ decomposition reacted with the surrounding magnesium. Thus the overall reaction is $\text{Mg} + \text{Mg}(\text{OH})_2 \rightarrow 2 \text{MgO} + \text{H}_2$ which is exothermic.

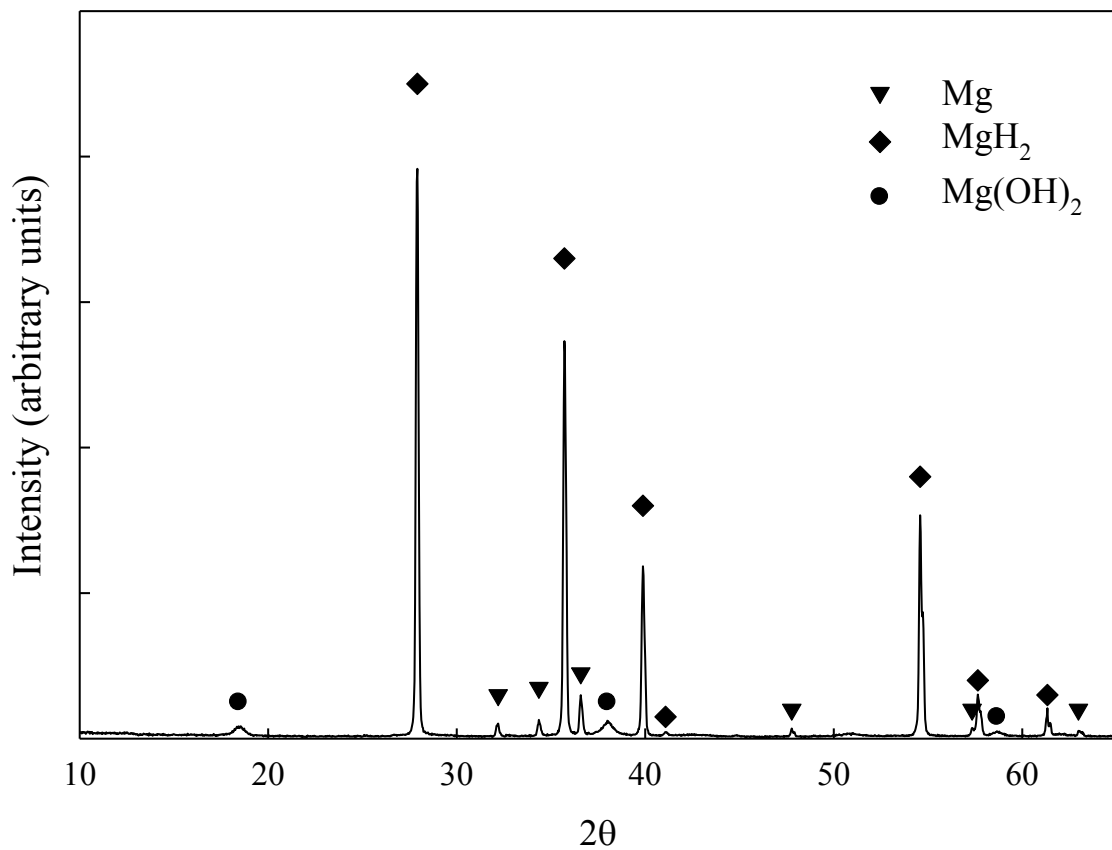


Figure 10. XRD of MgH₂ Powder

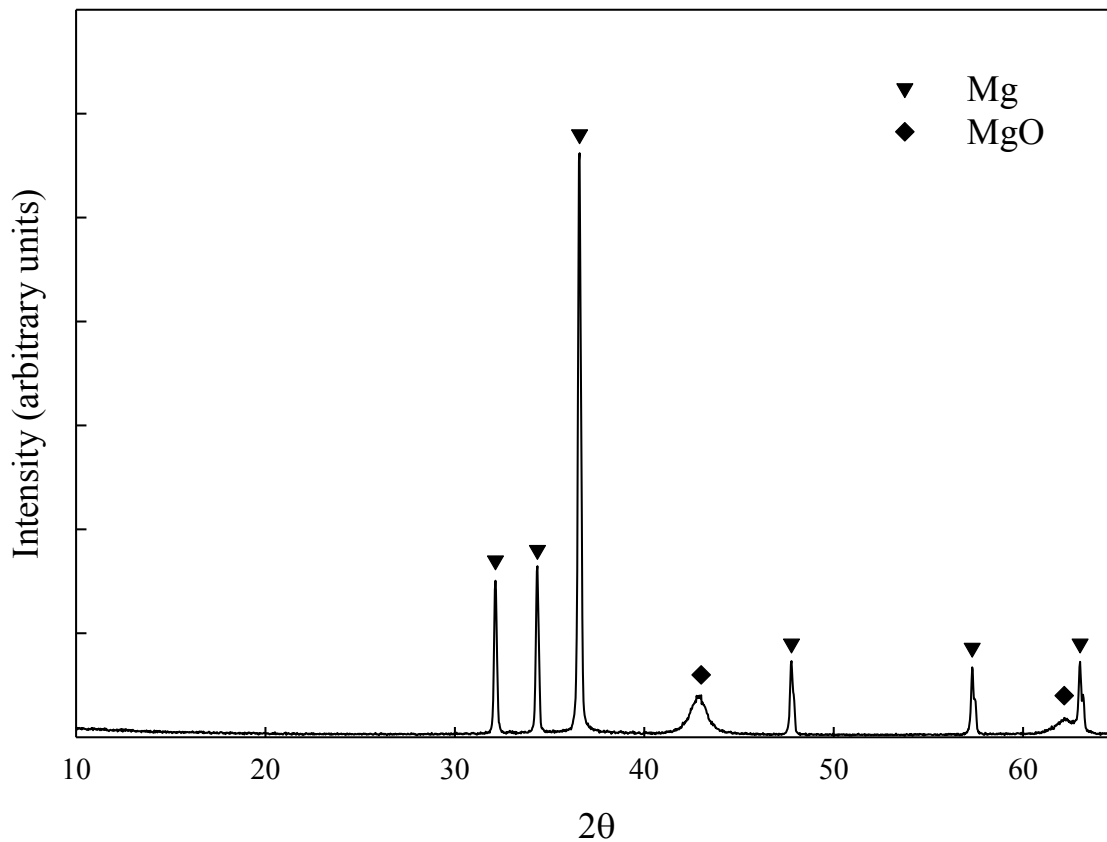


Figure 11. XRD of MgH₂ after decomposition

3.3 DSC of MgB₂ Formation from MgH₂ and B

Since the first exothermic reaction in the Mg/B powder mixture appeared to be initiated by Mg(OH)₂ decomposition, it was decided to try a MgH₂/B powder mixture using a clean source of MgH₂. The mixture was prepared using the same boron along with an unopened bottle of MgH₂ (98%, Alfa Aesar) which XRD confirmed to be

consisting only of MgH_2 . The powders were prepared in an identical fashion as the Mg/B mixture and also stored under P_2O_5 until used for DSC.

Several DSC runs were collected of the MgH_2/B powder mixture at ramp rates of 5, 7.5, 10, 12.5, and 15 $^\circ\text{C}/\text{min}$. under the same conditions as the Mg/B mixture (Fig. 12). The endothermic event beginning near 375 $^\circ\text{C}$ was MgH_2 decomposition. The exothermic event beginning near 575-600 $^\circ\text{C}$ was MgB_2 formation as confirmed by XRD of the post-reaction product (Fig. 13). This exothermic event appeared to be similar to the second exothermic event in the Mg/B powder mixture which supports the conclusion that the first exothermic event in the Mg/B powder mixture was initiated by $\text{Mg}(\text{OH})_2$ decomposition. Apparently, a clean source of Mg results in only one exothermic event for MgB_2 formation, at least with this boron powder. Also, MgB_2 formation occurred below the magnesium melting point (650 $^\circ\text{C}$), much like the Mg/B mixture. Interestingly, there appeared to be a small endothermic event at 620-640 $^\circ\text{C}$ that was superimposed on the larger reaction. It is unclear what this event was given that pure magnesium melts at 650 $^\circ\text{C}$. It is possible that the MgH_2 had some impurities which lowered the melting point, but in any case it did not seem to have a significant effect on the overall reaction.

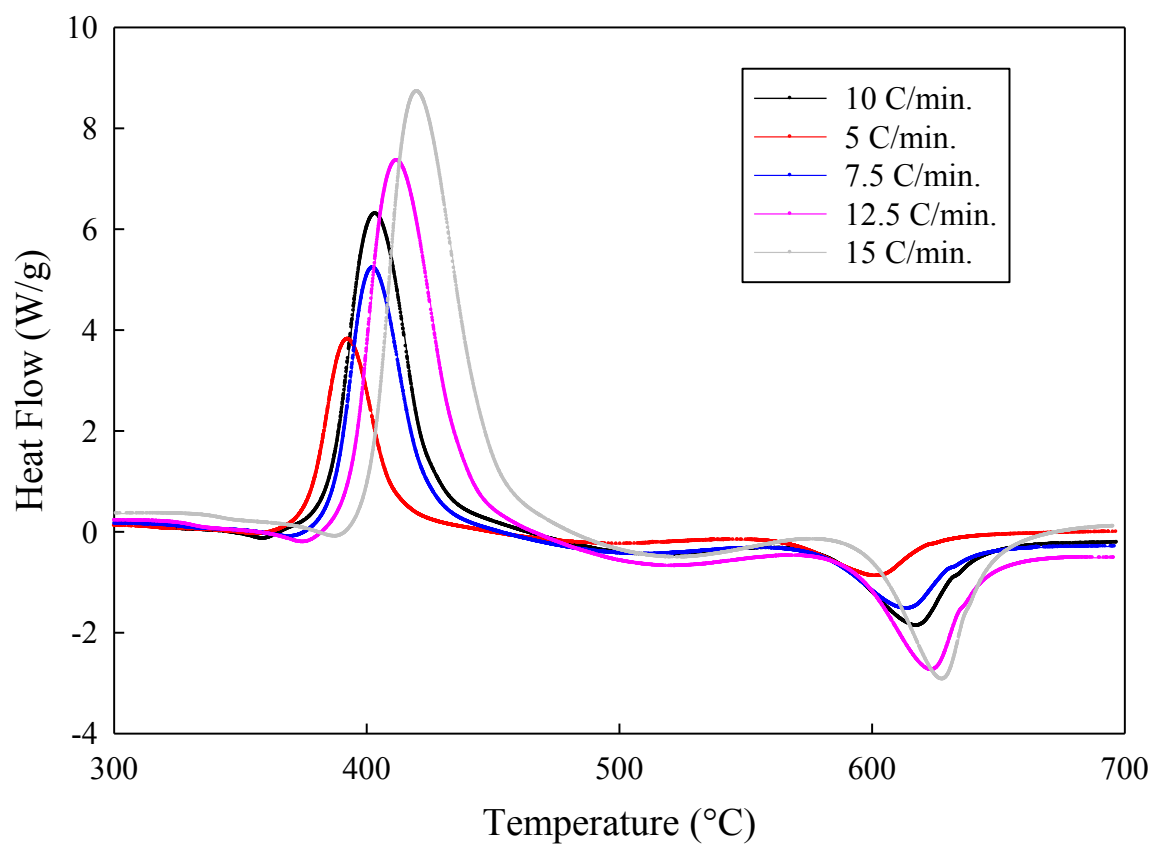


Figure 12. DSC of MgH₂/B powder mixture and various ramp rates

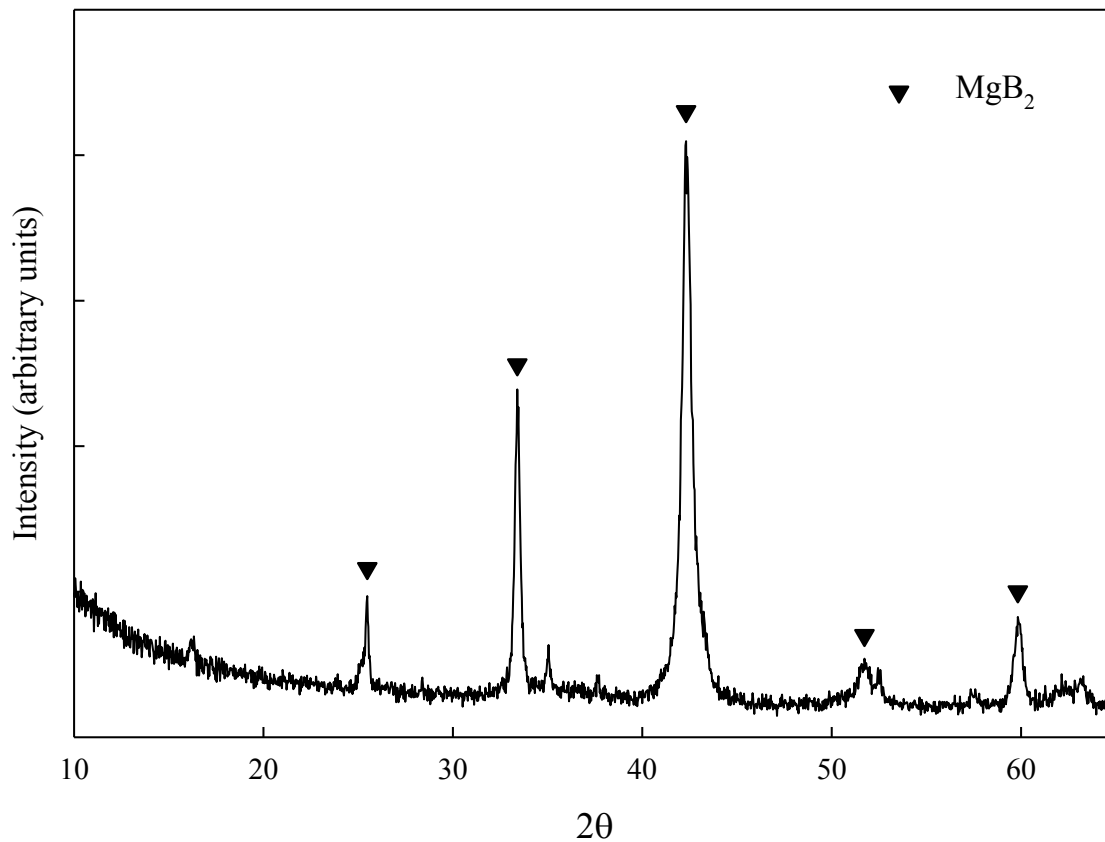


Figure 13. X-ray Diffraction of MgB_2 from MgH_2/B powder mixture after DSC run

3.4 Kinetic Analysis of MgH_2/B reaction

The DSC data at different ramp rates for the MgH_2/B mixture can be used to estimate the activation energy for MgB_2 formation using the Kissinger analysis method [80-81]. Of course, this analysis assumes that the reaction rate follows an Arrhenius temperature dependence, hence the activation energy. This assumption is sometimes questionable for heterogeneous systems, but it can be a useful approximation. For DSC,

the Kissinger analysis also assumes that the measured heat flow corresponds to the reaction rate and that the measured peak temperature corresponds to the maximum reaction rate. Also, the initial and final states of the reaction must be known which in this case corresponds to 0% MgB₂ and 100% MgB₂.

If a first order reaction is assumed, then the reaction rate equation is

$$\frac{dx}{dt} = A(1 - x)e^{-E/RT}$$

where dx/dt is the reaction rate, x is the fraction that has reacted, A is a pre-exponential factor, E is the activation energy, T is the temperature in Kelvin, and R is the gas constant [82]. If the maximum reaction rate is at the peak of the DSC curve, then the second derivative with respect to time will be zero assuming a constant heating rate.

$$\frac{d^2x}{dt^2} = \frac{dx}{dt} \left(\frac{E}{RT^2} \frac{dT}{dt} - Ae^{-E/RT} \right) = 0$$

By taking the term in the parentheses, setting it to zero, and taking the natural log of both sides, one can obtain the Kissinger analysis equation relating heating rate and peak reaction temperatures to the activation energy.

$$E = -R \left(\frac{d(\ln(\frac{\beta}{T^2}))}{d(\frac{1}{T})} \right) \quad \text{where} \quad \beta = \frac{dT}{dt}$$

The peak reaction temperatures from Fig. 12 were corrected for thermal lag in the DSC [79]. These corrections were estimated by multiplying the peak height (in mW) with the thermal lag constant (0.067 K/mW) to obtain a thermal lag correction that was subtracted from the peak temperature. The peak height was estimated using an extrapolation of the baseline of the DSC data as if no reaction had occurred. This

extrapolation introduced some error since the baseline of the DSC was not completely flat, but the thermal lag corrections were small since the thermal lag constant was small. A plot of the heating rate and corrected peak temperatures using the Kissinger analysis equation has a reasonably good fit to a straight line. Based on this data, the activation energy for the Mg/B reaction was approximately 239 kJ/mole.

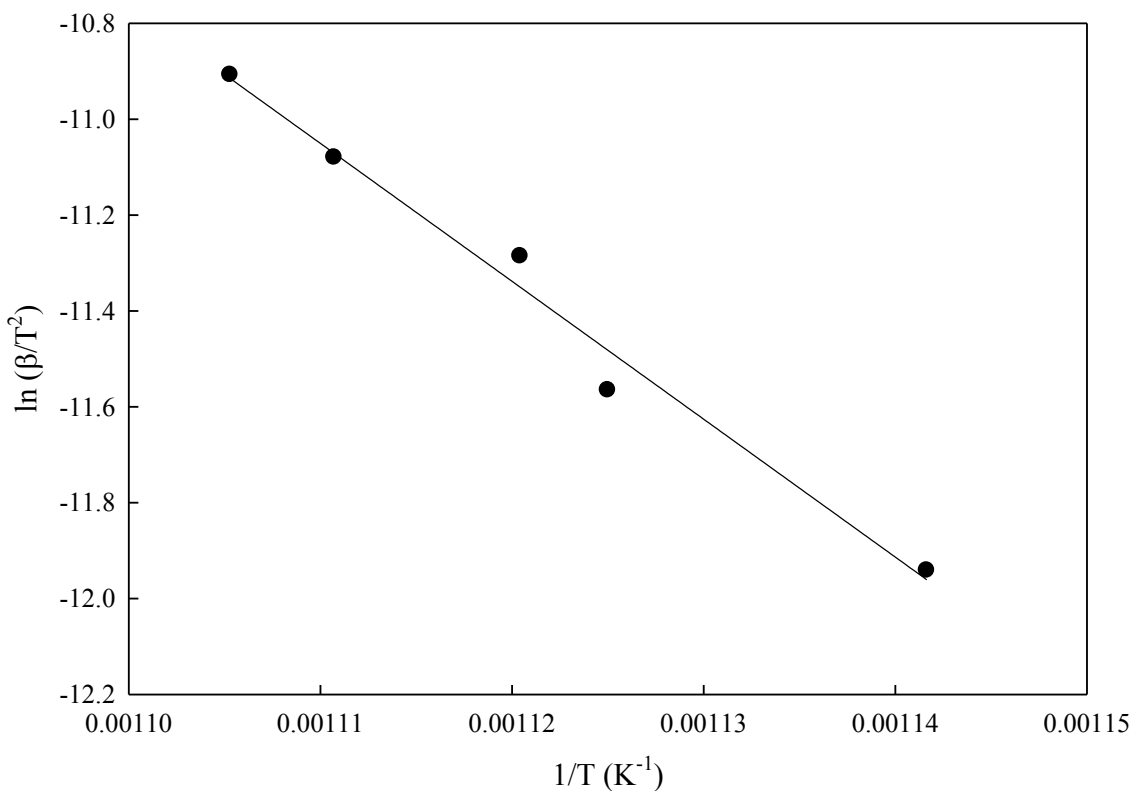


Figure 14. Kissinger Analysis of MgB₂ Formation

Although the Kissinger analysis offers a quantitative estimate of the activation energy for MgB₂ formation, it has limited utility and can even be misleading. It is based

on measurements of the macroscopic, not microscopic, heat flow in the sample. If MgB_2 were the only compound in the Mg-B phase diagram, then the reaction $\text{Mg} + 2\text{B} = \text{MgB}_2$ would be an accurate description. However, the actual reaction may be some multistep process that forms MgB_7 , MgB_4 , and finally MgB_2 . The Kissinger analysis only provides what might be called an “apparent activation energy” that encompasses all those individual reaction steps, whatever they may be. It also has limited utility since it only applies to the reaction of MgH_2 with this particular source of boron (sub-micron amorphous powder). It does not apply to other boron sources since reaction kinetics are affected by many variables including particle size, purity, morphology, surface area, etc. It also does not apply to the Mg/B mixture since that powder mixture had two exothermic reactions, not one.

3.5 Limitations of Low Temperature Synthesis

The main problem with the low temperature synthesis of MgB_2 is that it is impossible to manufacture a fully dense product. This is due to a combination of powder packing limitations and the fact that the molar volume of MgB_2 is less than the molar volume of the elemental constituents. The porosity issue is most readily apparent when viewing the microstructure of a post-reacted Powder-in-Tube MgB_2 wire using a fractured sample (Fig. 15). All throughout the sample, there are holes where the magnesium used to exist before it melted and reacted with the boron powder. This porous microstructure cannot be addressed by any powder processing method and thus there is a

fundamental limit to what can be accomplished in terms of sample homogeneity and density with the low temperature synthesis method of reacting powders.

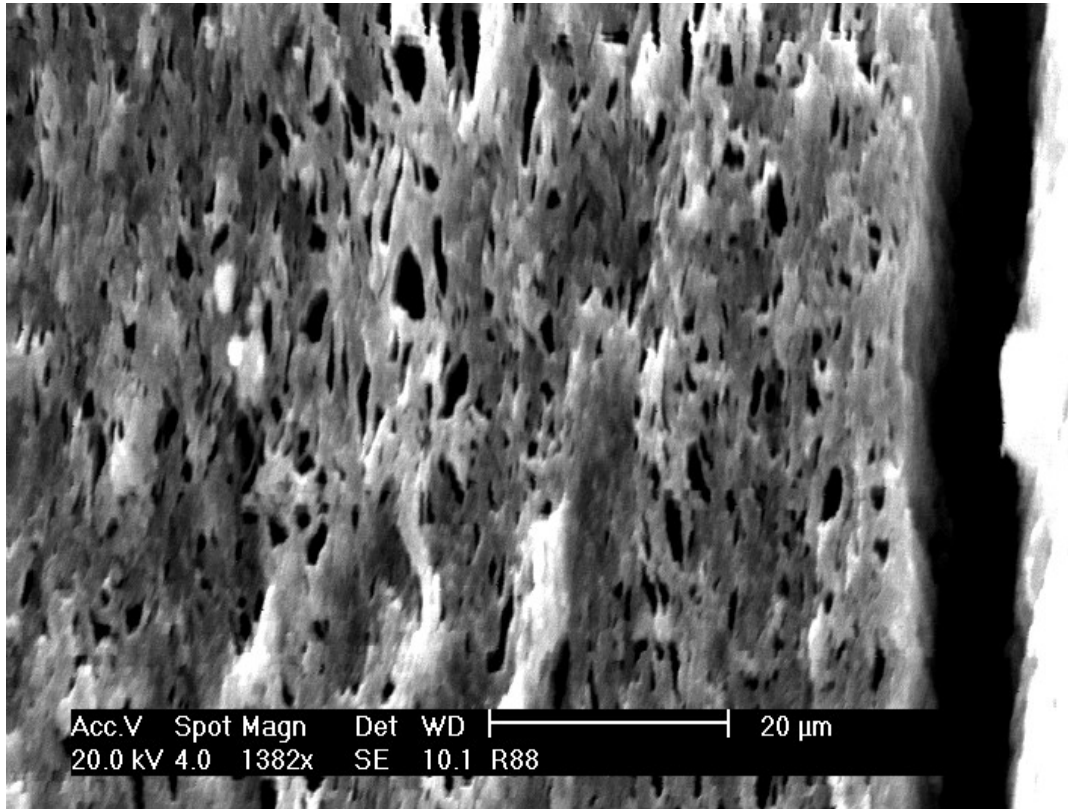


Figure 15. Fracture SEM Image of MgB₂ PIT wire reacted at 700 °C for 0.5 hr.

CHAPTER 4: DETERMINATION OF THE INCONGRUENT MELTING TEMPERATURE OF MgB_2

The poor quality of samples produced by the powder reaction process made it necessary to explore higher temperature synthesis methods that would produce homogeneous, dense samples. As discussed earlier, the main problem with higher temperatures for MgB_2 is the high vapor pressure of magnesium. This was solved by heating under high pressure to suppress magnesium vapor loss. Also, the high pressure furnace enabled the first experimental measurement of the incongruent melting temperature of MgB_2 .

4.1 Description of High-Pressure High-Temperature Furnace

The pressure vessel was taken from a non-functioning thermal analysis apparatus and consisted of two hemispherical halves that were bolted together (Fig. 16). The maximum certified pressure was 10 MPa (~1500 psi) so a 1500 psi pressure relief valve was installed along with a burst disc in case the pressure relief valve failed. The pressure relief valve and burst disc were passive devices that did not require human intervention to operate. Originally, the pressure vessel contained a resistively heated furnace, but it was ultimately abandoned for reliability reasons. Fortunately, induction heating proved to be much more reliable. This heating method operates by inducing a high frequency current in an electrically conductive material (called a susceptor) which generates resistive losses

that heat the material. Either the sample can be heated directly or a material surrounding the sample can be heated which then heats the sample.

A Lepel T-5-3 induction heating power supply with a maximum power output of 5 kW at 450 kHz was used for induction heating (Fig. 16). The power supply was either controlled manually using a potentiometer on the front panel, or automatically through a temperature controller on the front panel. A toggle switch on the front panel was used to select between manual and automatic control. The temperature controller was a Eurotherm 3504 with multiple thermocouple inputs and a high resolution output that used a 0-10 V signal to control the power supply. For safety reasons, the Eurotherm controller was limited to 50% maximum output signal (5 V) so the power supply would not exceed 2.5 kW output. This was found to be more effective than a software temperature limit for limiting the power level since thermocouples may report an incorrect temperature if they have a short in a low temperature area.



Figure 16. Pressure Vessel and LepeL 5 kW Power Supply

Induction heating requires a water cooled copper coil so the two ports at the top of the pressure vessel were modified to accept feedthroughs for copper tubing (6.3 mm dia.). The copper tubing was fabricated into a 9-turn coil (75 mm inside dia.) that was positioned in the middle of the vessel (Fig. 17). Outside the pressure vessel, the copper tubing was connected to the Lepel power supply which was in turn connected to a Haskris water chiller (not shown). Also, the Lepel power supply had a water over-temperature safety switch and water flow safety switch in case the water chiller failed.



Figure 17. Water cooled copper coil for induction heating

The susceptor assembly consisted of a graphite tube surrounded by graphite felt all in a closed-bottom fused silica tube (Fig. 18-19). The closed-end graphite tube (3.8 cm dia., 0.3 cm wall thickness, 15 cm length from Semco Carbon) contained the sample and this approach was found to be more effective than heating the sample directly. The graphite felt (6.3 mm thickness, GFA5, SGL Carbon Group) was used to reduce convection, conduction, and radiation heat losses so high temperatures could be reached with minimal power input (graphite felt does not couple to the induction heating power supply). A graphite plug was placed above the sample with a hole for a thermocouple and more graphite felt was packed on top. To reduce heat losses further, a ceramic cap with two holes for thermocouples was placed on top of the graphite felt. One thermocouple was inserted into a hole in the graphite tube wall and the other directly into the sample. The susceptor assembly rested on a stack of ceramic bricks which were adjusted in height so the graphite would be approximately in the center of the induction coil.

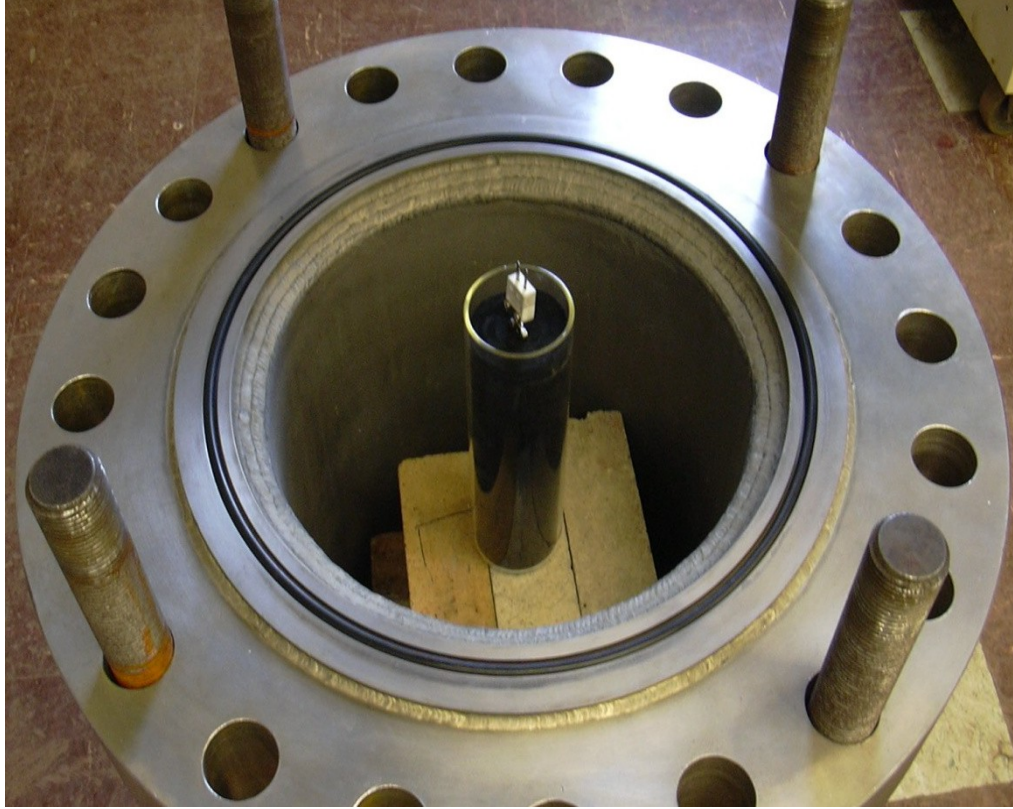


Figure 18. Susceptor Assembly (only one thermocouple shown)

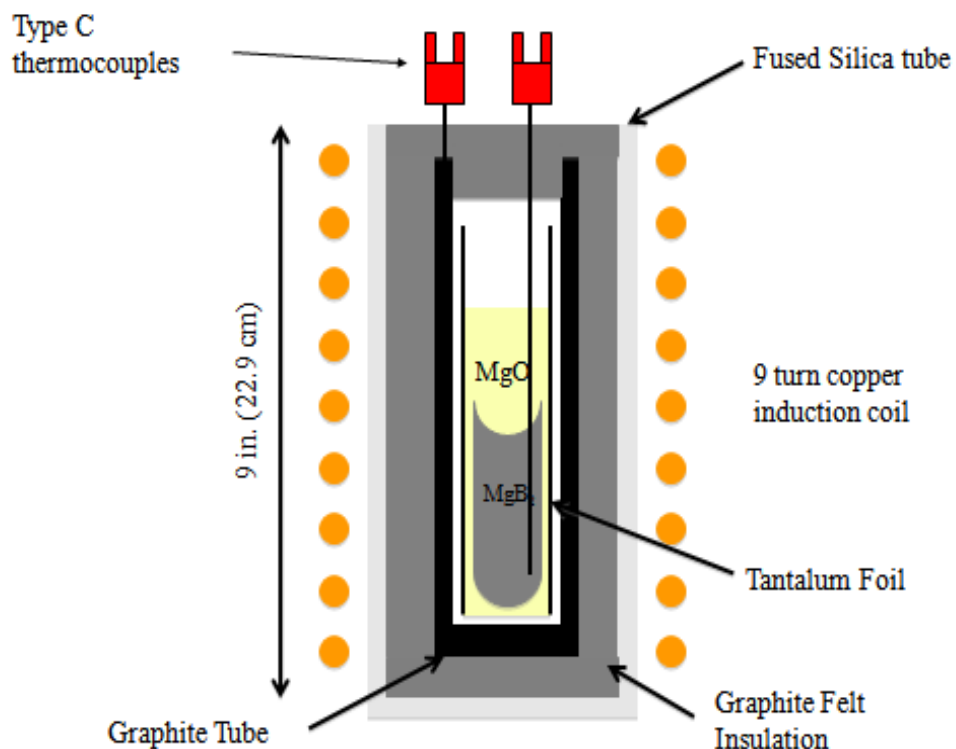


Figure 19. Susceptor Assembly

For sample containment, MgO crucibles (Ozark Technical Ceramics, 2.5 cm diameter, 7.6 cm length) were used up to 1700 °C and did not react with the Mg/B samples. The crucibles did contain ~3 wt% yttria (Y_2O_3) used as a sintering aid during manufacture, but there was no indication of yttrium contamination of the samples. Also, the crucibles appeared to be sensitive to thermal shock since they often cracked on heating/cooling. This problem was addressed by wrapping the crucibles with tantalum foil (0.3 mm thickness) which reduced the occurrence of cracking. The tantalum foil also prevented the MgO from touching the graphite which is known to reduce MgO at very high temperatures [84].

The thermocouples were custom made using Type C thermocouple wire (W-5%Re / W-26%Re, 0.13 mm diameter) from Concept Alloys, Inc., and high purity alumina 2-hole insulator (99.8%) from Omega Engineering, Inc. The thermocouple wire was certified to be within 1% of the standard tables for thermoelectric output via NIST-traceable standards [85]. Also, the thermocouples were surrounded by a tantalum sheath to protect the wire from reacting with the graphite, Mg/B samples, and magnesium vapor. For the thermocouple cold junctions, an ice bath in a vacuum-insulated dewar was found to be much more stable than the on-board cold junction compensation circuit on the temperature controller so the on-board compensation circuit was disabled.

4.2 Smith Thermal Analysis Implementation

Although MgB_2 has been predicted to melt incongruently, there has been no experimental measurement to date of the incongruent melting temperature. Thus it was uncertain what time/temperature program would produce homogeneous MgB_2 samples. Normally, Differential Thermal Analysis (DTA) would be a suitable experimental method to make such a measurement except most DTA instruments only operate at standard pressure (0.1 MPa or 1 atm). Some DTA instruments have high pressure capability but only operate at lower temperatures. Modifying a commercial DTA instrument for the high pressure furnace was deemed too difficult and unlikely to succeed. Fortunately, an alternative that proved satisfactory was the Smith Thermal Analysis (STA) method [86]. This experimental technique was developed by Cyril

Stanley Smith as an alternative to DTA for measuring the specific heat and phase equilibria of metal samples. Although there are no commercial instruments that use this method, it has been used in a number of phase diagram investigations using custom built equipment [87–97].

The basic idea of STA is that instead of heating/cooling the furnace at a constant rate, as in DTA/DSC, the furnace is controlled so that there is a constant temperature difference between the sample and the furnace. When the sample undergoes some transformation that absorbs heat (on heating) or releases heat (on cooling) resulting in a thermal arrest, then the control loop compensates to maintain a temperature difference. By maintaining a temperature difference, there is a constant heat flux either into or out of the sample during the transformation. This concept of incorporating the sample as part of the control loop for the furnace is a distinct departure from DTA/DSC where furnace heating/cooling is completely independent of the sample. In fact, the STA method is now classified as one of many Sample Controlled Thermal Analysis (SCTA) methods [98].

In the original implementation by Smith, a metallic sample was placed in a ceramic crucible with a thermocouple to measure the sample temperature. Another thermocouple was placed outside the crucible next to the furnace wall. Then an analog temperature controller was used to maintain a constant temperature difference between the sample thermocouple and the furnace thermocouple to maintain a constant heat flux. Of course, the thermal conductivity of the crucible varied with temperature so the heat flux was constant only over limited temperature ranges. Also, the thermal conductivity of

the crucible needed to be much lower than the sample so the temperature gradient would be localized to the crucible wall.

The main benefit of the STA method is that the sample remains closer to thermodynamic equilibrium during thermal arrests since the furnace stops ramping during those events. This is unlike DTA/DSC where thermal events appear to be spread over a range of temperatures since the furnace continues heating/cooling while the transformation is occurring (as seen in the previous chapter with the pure lead sample in DSC). However, the STA method is not a replacement for DTA/DSC since it cannot be used with samples that have spontaneous (non-equilibrium) reactions. For example, the STA method would not work with the Mg/B powders studied in the previous chapter. Basically, the control system cannot compensate for the sudden rise in temperature of the sample unless the exothermic reaction is so sluggish that it does not affect the stability of the control loop. Ideally, it should only be used on samples that are already pre-reacted or pre-alloyed.

In this STA implementation, the graphite thermocouple measured the “furnace” temperature and the sample thermocouple measured the sample temperature. The temperature difference was calculated in software and set as the control variable in the feedback control loop of the temperature controller. Manual power was used to increase the temperature to some intermediate value and then the system was switched to automatic control. In automatic control, the Eurotherm controller maintained some temperature difference set point which was adjusted to either start a heating or cooling run. All data were collected at one second intervals and logged to a computer using the

iTools software provided by Eurotherm. A more detailed description of the protocol used for this STA implementation can be found in Appendix I.

4.3 Smith Thermal Analysis of Aluminum

The STA control system was tested on aluminum (Sigma-Aldrich, 99.9%) since it has a high thermal conductivity, low melting point (660 °C), and a large latent heat at the solid/liquid transition. Aluminum pellets were loaded into an MgO crucible and a Type C thermocouple was inserted directly into the aluminum pellets. Then the vessel was repeatedly pumped down to approximately 50 mTorr and backfilled with argon (99.998%) to remove most of the air in the chamber (high pressure was not used for this run). Manual power was used to increase the temperature to >800 °C to melt all the aluminum (Fig. 20). After settling, the sample temperature was ~20 °C higher than the graphite temperature which was unexpected. The graphite tube may not have been optimally positioned in the induction coil so there may have been uneven coupling between the top and bottom of the graphite tube. The graphite thermocouple was at the top of the graphite tube, not at the bottom where the sample was located, which may be why the graphite temperature was lower than the sample temperature. In any case, this discrepancy was solved by using a temperature difference set point either higher or lower than 20 °C to enable heating and cooling.

The STA run was started by switching the system to automatic control with a temperature difference set point of 35 °C (Fig. 20). This started a cooling run that had an

effective cooling rate of 4 °C/minute. At 660 °C, the aluminum began to solidify resulting in a temperature arrest due to the release of latent heat. The control system responded by regulating power so the graphite thermocouple was at 625 °C in order to maintain the temperature difference set point of 35 °C. The temperature gradient eventually resulted in complete solidification by establishing a heat flux from the sample to the graphite. The key point is that the STA method regulated the system so that the heat flux was approximately constant which prolonged the thermal arrest.

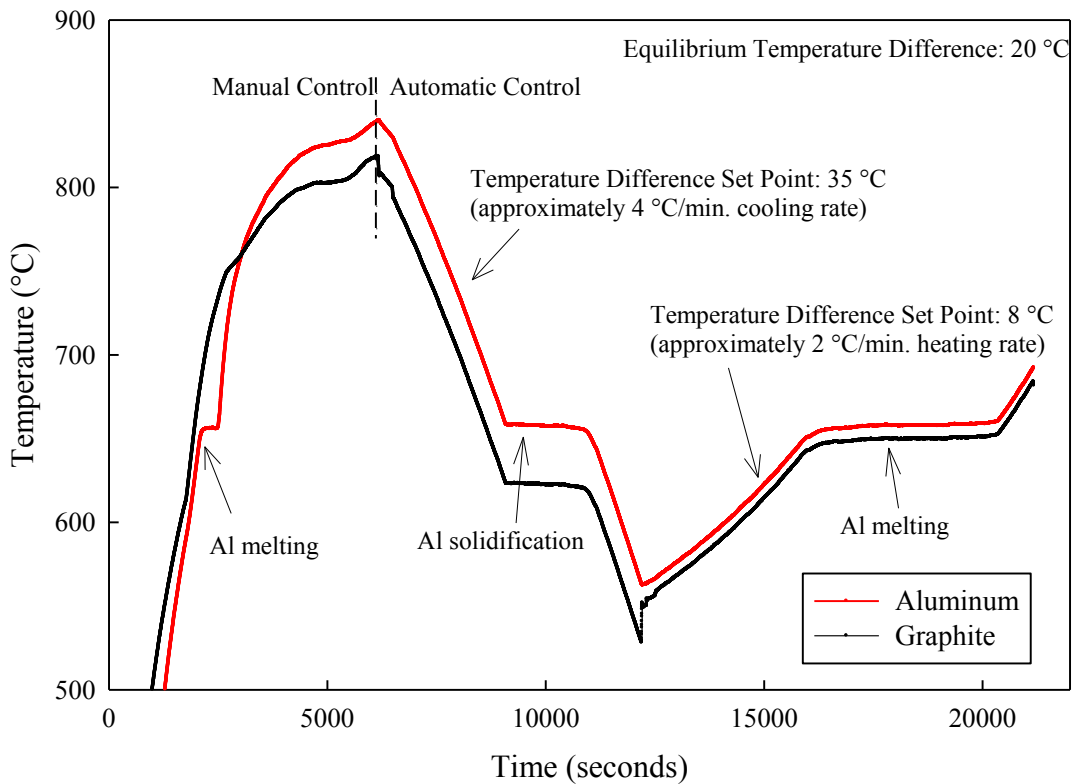


Figure 20. STA run on aluminum

After the aluminum had all solidified and the temperature reached ~550 °C, the temperature difference set point was changed from 35 °C to 8 °C in order to start a

heating run (Fig. 20). The 8° C set point was less than the equilibrium temperature difference of 20 °C which resulted in a heating rate of 2 °C/minute. The thermal arrest was extended for an even longer period of time due to the smaller temperature gradient. In fact, it is possible to extend thermal arrests for very long periods of time although there are practical limitations such as the finite number of bits of the analog-to-digital converter used in digital temperature controllers. It should also be mentioned that the furnace material itself should not have any phase transformations in the temperature range of interest which is the case for graphite. Also, the control system must be able to respond to any thermal arrests in the sample meaning the furnace must be able to change temperature relatively quickly, a distinct advantage with induction heating.

For the aluminum STA run, the thermal arrests were unambiguous due to the large latent heat of the transition. However, a derivative plot is also useful since it demonstrates that the derivative is zero at the melting/freezing transition which produces a square-well in the plot (Fig. 21). This plot is a discrete derivative which used 10 sec. time intervals as a quasi-smoothing function. The main point of this exercise was to demonstrate the STA method and verify the correct operation of the control system.

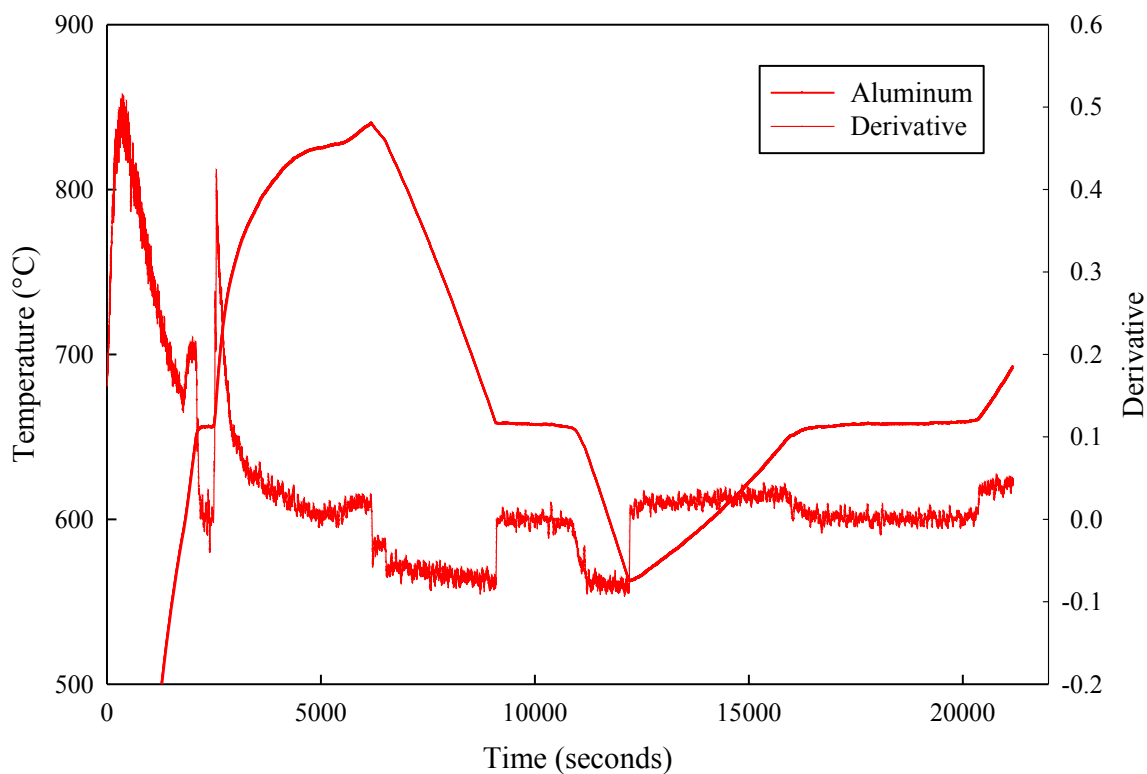


Figure 21. STA run on aluminum with derivative

4.4 Smith Thermal Analysis of AlB_2

The STA system was also tested with AlB_2 since it is the closest analogue to MgB_2 . The phase diagrams for Al-B and Mg-B are similar in that there are no boride phases between the pure metal and the diboride (Fig. 22) [99]. Also, AlB_2 melts incongruently into a liquid and a higher boride (AlB_{12}) and it has been predicted that MgB_2 melts incongruently into a liquid and a higher boride at high pressure (MgB_4) [39]. The equilibrium transformation can be represented as: $6 \text{AlB}_2 \leftrightarrow \text{AlB}_{12} + 5 \text{Al}_{\text{liquid}}$.

Recently, the incongruent melting temperature (peritectic temperature) of AlB_2 was estimated to be 972°C based on DSC data that was extrapolated to a zero heating rate.

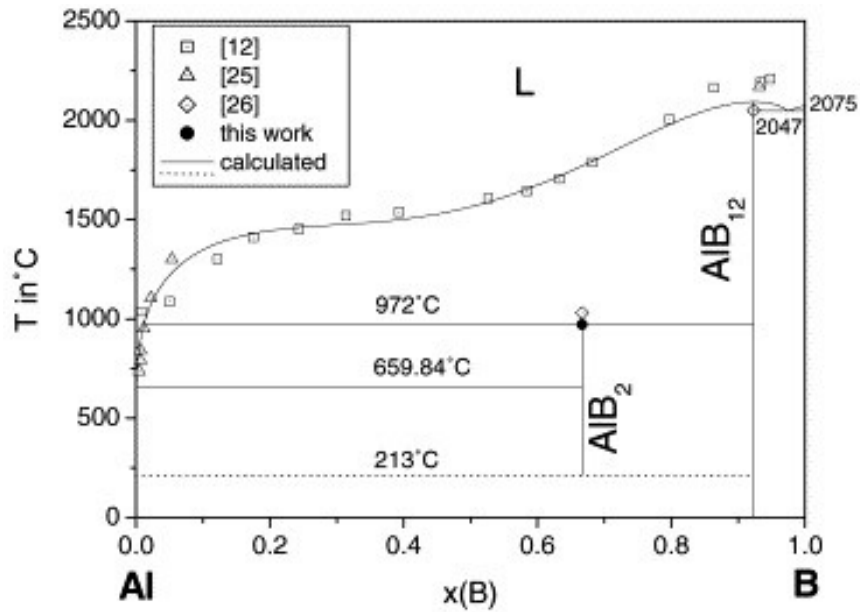


Figure 22. Al-B phase diagram [99] (reproduced with permission from Elsevier)

The authors of that study noted that the AlB_2 peritectic transformation was only observed on heating and never on cooling or subsequent heating runs [99]. The reason for the asymmetry between heating and cooling was probably due to the slow kinetics of peritectic transformations on cooling [100]. Upon cooling below the peritectic temperature, the AlB_{12} and liquid react to form AlB_2 which occurs via nucleation and growth of AlB_2 on the surface of the AlB_{12} particles/grains. That initial skin of AlB_2 slows down further transformation since solid state diffusion of Al and/or B must occur

through that initial skin to further react with the AlB_{12} core. Solid state diffusion is very slow compared to liquid state diffusion so it is common for systems that contain a peritectic to retain a high temperature (non-equilibrium) phase on cooling that would not be present in well annealed samples. Also, the nucleation of the low temperature phase (AlB_2 in this case) on cooling usually requires some amount of undercooling below the peritectic temperature. Thus the peritectic temperature is usually determined on heating rather than on cooling using well annealed samples.

For this STA run, AlB_2 powder (-325 mesh, Sigma-Aldrich) was loaded into an MgO crucible and a Type C thermocouple was inserted directly into the powder. The vessel was evacuated and backfilled with argon multiple times as with the aluminum run (high pressure was also not used for this run). Manual power was used to bring the temperature up to ~ 750 °C and the equilibrium temperature difference was the same as before, approximately 20 °C (Fig 23). A heating run was started by using a 15 °C temperature difference set point which resulted in a ramp rate ~ 2 °C/min. near 770 °C and ~ 5 °C/min. near 1000 °C. It is not clear why the ramp rate varied so much but it may have been due to different heat transfer conditions than the aluminum STA run. A thermal arrest was observed at ~ 1013 °C which is higher than the 972 °C value determined by Mirkovic et al. [99]. This discrepancy could be due to purity issues. Near 1100 °C, the induction power supply was shut off and data was collected on cooling. There was no indication of reformation of AlB_2 on cooling and in fact a small exothermic event was observed near 660 °C. That thermal signature was probably solidification of aluminum which agrees with the lack of any observed reformation of AlB_2 on cooling.

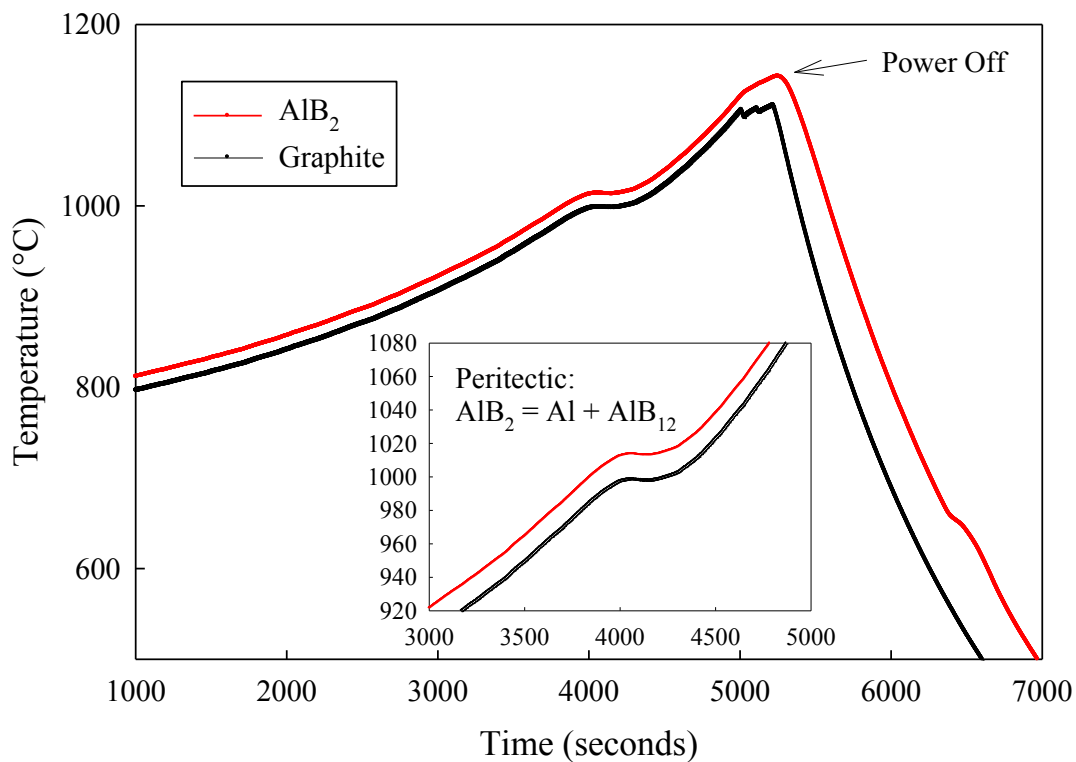


Figure 23. STA run on AlB_2 powder

Although the derivative plot is useful for identifying the AlB_2 peritectic, it does not make up for the fact that the thermal arrest in the AlB_2 was not as well defined as with the pure aluminum. There was no well defined square well in the derivative data so it is difficult to identify an unambiguous temperature for the peritectic. If the minimum in the derivative data is used as an approximation then the temperature was 1013 °C. The important point is that the peritectic was measured using the STA method on AlB_2 which is the closest analogue to MgB_2 .

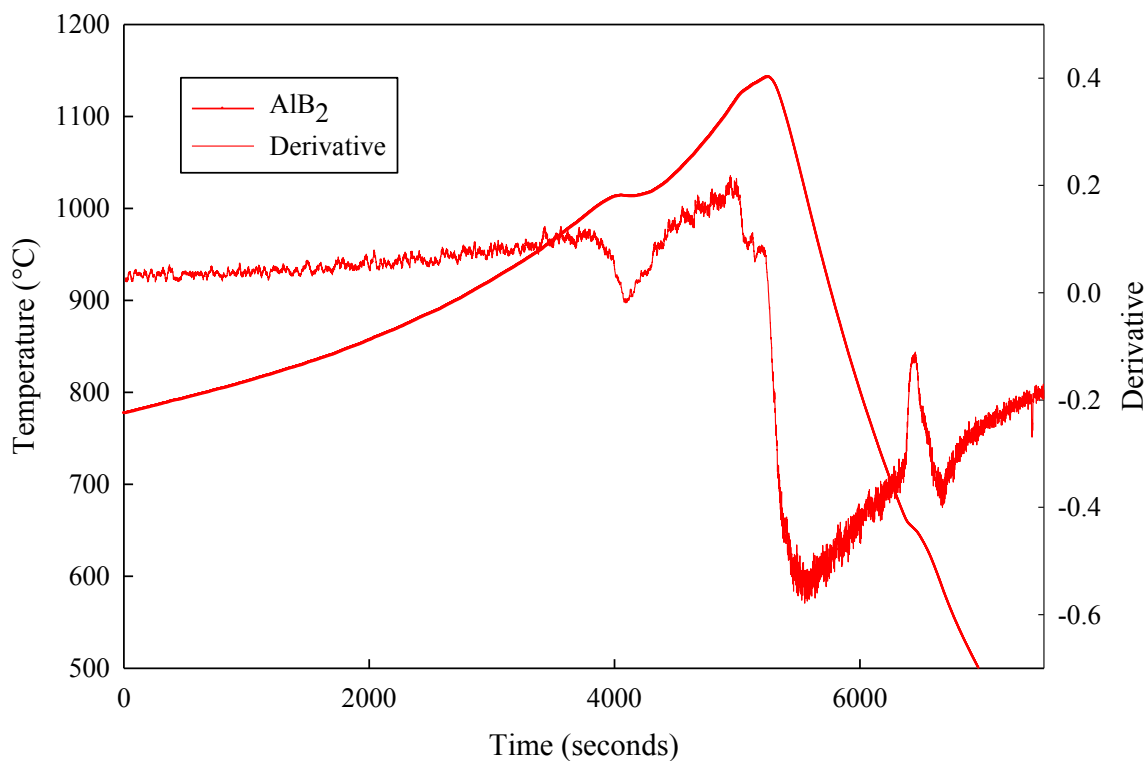


Figure 24. STA run on AlB_2 powder with derivative

4.5 Smith Thermal Analysis of MgB_2

The STA run for MgB_2 was similar to the AlB_2 run except high pressure was used to suppress magnesium vapor loss. During the development of the high pressure furnace, it was observed that there was still some magnesium loss even at high pressure. An easy procedure to check for magnesium loss was to weigh the crucible assembly before and after the run. Any weight loss was ascribed to magnesium loss if there were no broken or missing pieces from the crucible assembly. For this run, MgB_2 powder (-325 mesh,

Sigma-Aldrich) was weighed along with the crucible, tantalum foil, and thermocouple to obtain a total weight. A small amount of magnesium chips (99.98%, Sigma-Aldrich) were added to this sample to counter any magnesium vapor loss for an overall composition of $Mg_{35}B_{65}$. The MgB_2 powder was checked with X-ray Diffraction before the run and only MgB_2 and a small amount of MgO were detected.

Manual power was used to bring the temperature up to ~ 1250 °C on the graphite thermocouple and there was a ~ 80 °C difference between the sample and the graphite (Fig. 25). This ~ 80 °C difference was considerably greater than the 20 °C difference for the aluminum and AlB_2 STA runs. Also, the graphite temperature was higher than the sample temperature. The larger temperature gradient and the graphite/sample temperature reversal may have been due to different positioning of the graphite tube in the induction coil or different heat transfer conditions at high pressure. At ~ 1250 °C, automatic control was turned on with a temperature difference set point of 76 °C which produced a ramp rate of ~ 23 °C/min. The high ramp rate was intentional since data had to be collected before the internal gas temperature reached 75 °C, the limit of the high pressure furnace. A thermal arrest was observed on heating except it was even broader than with the AlB_2 STA run (Fig. 26). At 1700 °C (sample temperature), the internal gas temperature limit was reached so the power was shut off (the sample thermocouple failed intermittently on cooling for unknown reasons). A small exothermic event was observed on cooling at approximately 630 °C which may have been due to impure magnesium solidification (as seen in the derivative plot).

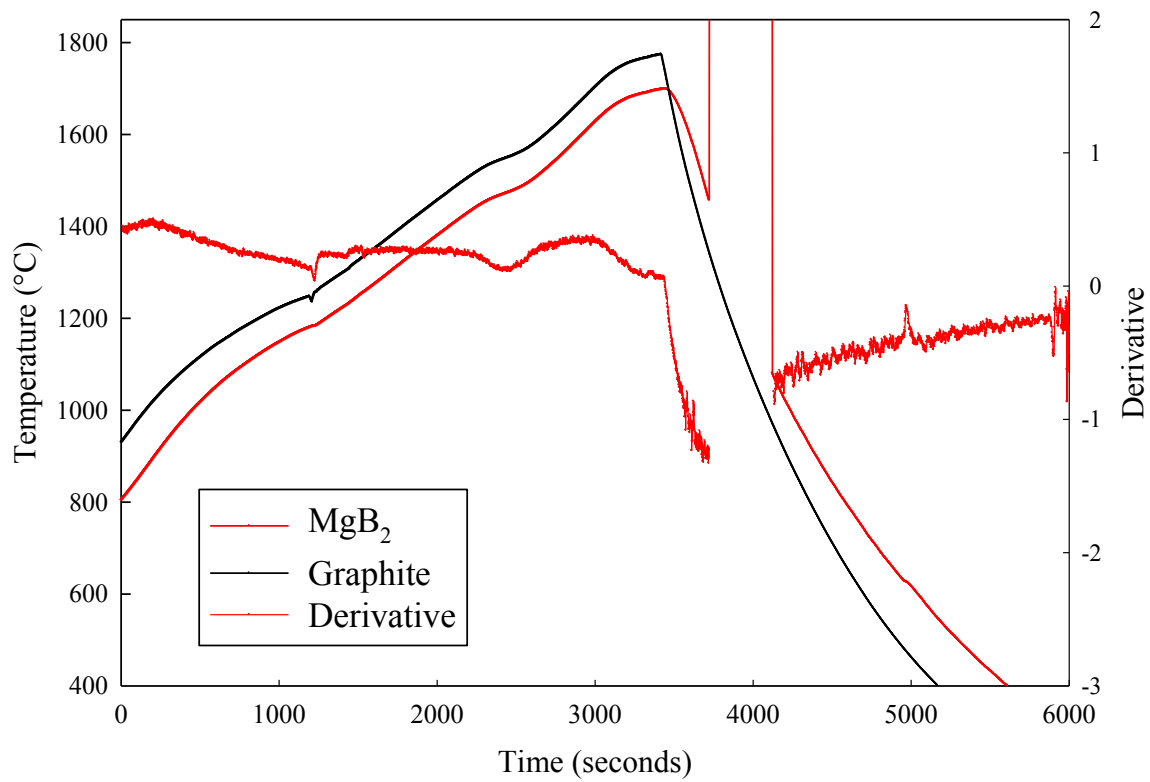


Figure 25. STA run on MgB₂ powder with derivative

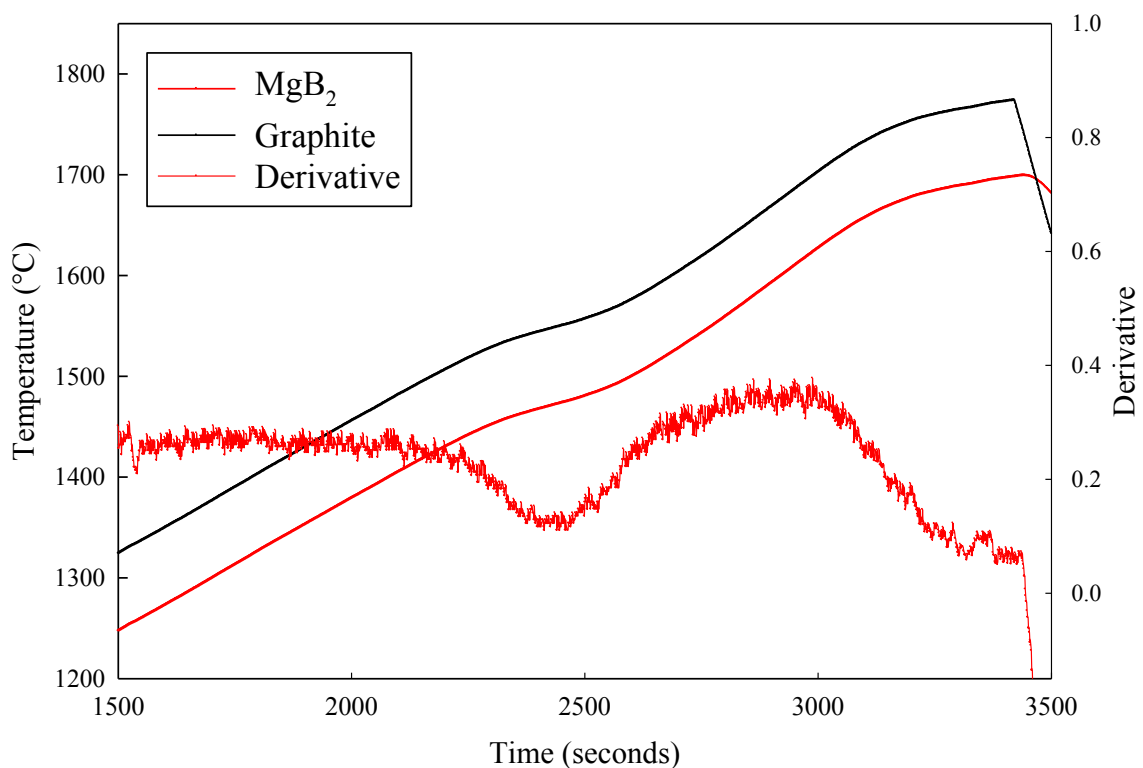


Figure 26. STA run on MgB₂ powder with derivative (enlarged)

After the STA run, the crucible assembly was weighed to obtain a final overall composition of $\sim\text{Mg}_{34}\text{B}_{66}$ assuming all the weight loss was due to magnesium. This was still more magnesium rich than the stoichiometric composition ($\text{Mg}_{33.3}\text{B}_{66.6}$). The sample thermocouple had failed at high temperature but there was no apparent dissolution of the sheath and the thermocouple was extracted from the sample without damaging the ingot. Most of the sample had fused together into a solid mass which was sectioned and

polished. There was considerable porosity but not enough to affect the mechanical integrity of the ingot.

The ingot microstructure as observed in the SEM with backscatter detector consisted of dark cores surrounded by a lighter matrix (Fig. 27). The dark cores were an indication of a phase with a lower average atomic number composition since backscatter electron yield is sensitive to the average atomic number. The EDS detector was used to examine the local chemical composition but only Mg and O peaks could be detected (EDS detectors are not sensitive to low atomic number elements such as boron). Large oxide inclusions were also noticeable (Fig. 27).

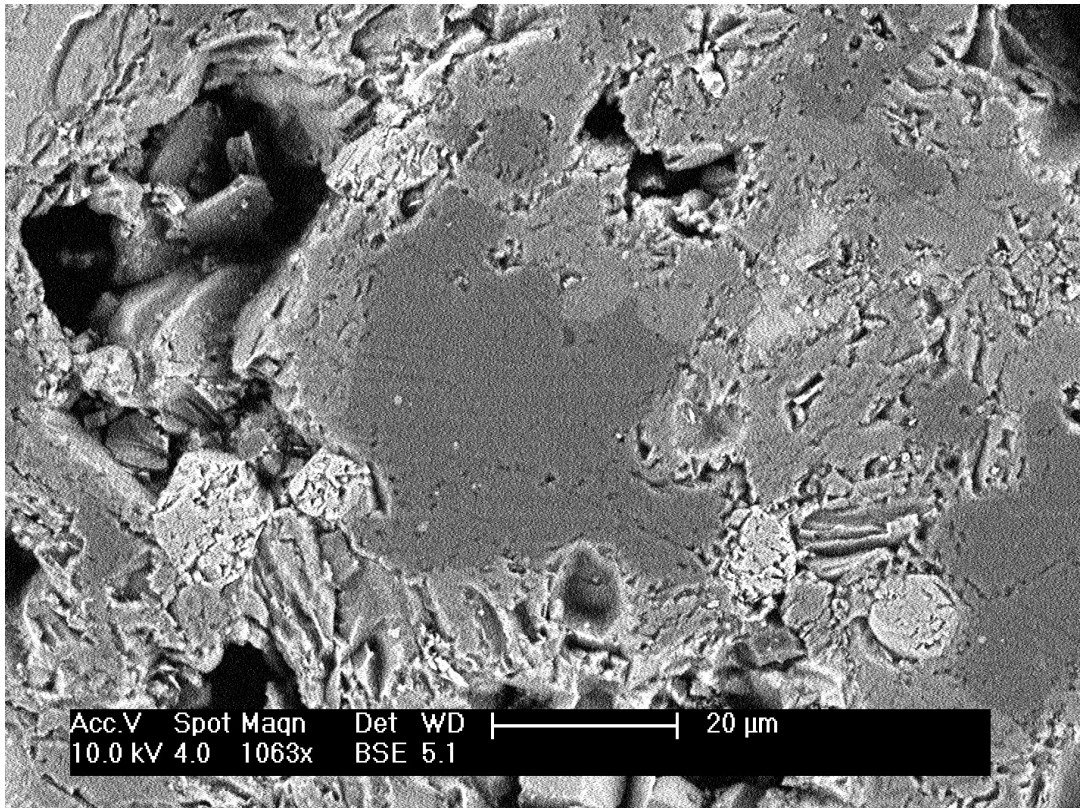


Figure 27. Microstructure of MgB₂ ingot after STA run

The X-ray diffraction data indicated the presence of Mg, MgB₂, MgB₄, and MgO (Fig. 28). Although the Mg, MgB₂ and MgO peaks matched the peak locations from the Powder Diffraction File database, the MgB₄ peaks were shifted to the right (indicating a smaller unit cell). It's not clear why only the MgB₄ would exhibit such an effect unless the MgB₄ phase had some impurities that changed the lattice parameters.

However, the presence of MgB₄ in the X-ray diffraction data and the dark cores observed in the SEM suggested that the thermal event observed on heating was the MgB₂ peritectic, especially since the starting material was MgB₂ powder and Mg. On heating above the peritectic, the MgB₂ would have decomposed into MgB₄ and a liquid. Then on cooling, the reverse transformation would have been limited by the slow kinetics of peritectic transformations which would explain the MgB₄ cores. Also, the overall composition was magnesium rich compared to the stoichiometric composition so the MgB₄ cannot be ascribed to magnesium vapor loss. Unfortunately, the thermal signature observed on heating was so broad that it was not possible to assign a well defined temperature to the peritectic. Also, there was a large amount of oxide contamination as seen in the X-ray diffraction data and the SEM. Either the oxide was originally from the MgB₂ powder or it may have come from oxygen impurities in the argon gas. In either case, the large amount of oxide and the general porosity of the sample did not provide a quality sample for further analysis.

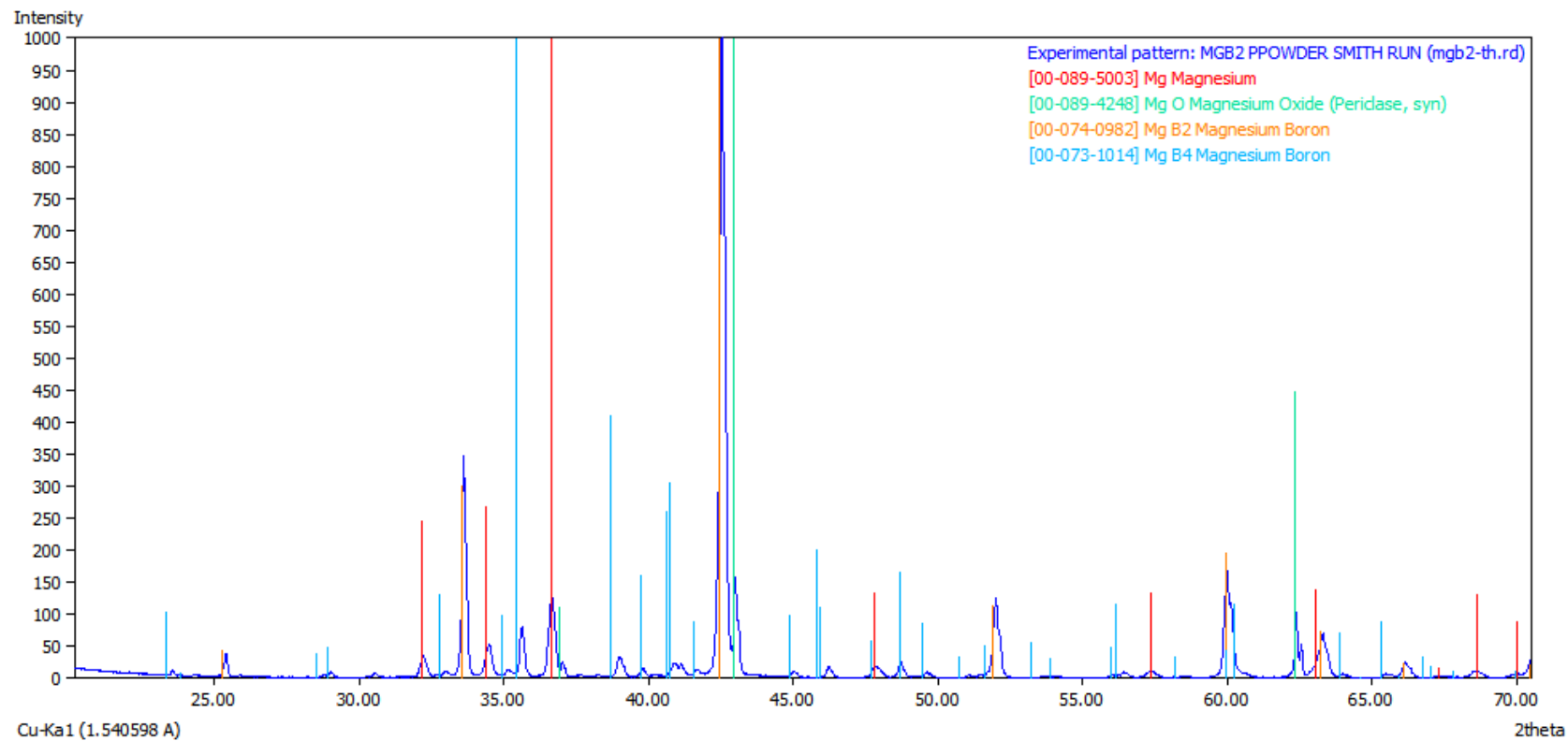


Figure 28. X-ray Diffraction of MgB₂ Ingot from STA run

4.6 Thermal Analysis of Mg-B Mixtures

The STA run with MgB_2 powder did not provide a well defined temperature for the peritectic so additional measurements were attempted using elemental mixtures of magnesium and boron that were reacted on heating. There were no successful STA runs with the elemental mixtures, but it was possible to use a standard ramp/dwell/cool sequence with the graphite thermocouple as the control thermocouple (the sample thermocouple was only used to record the sample temperature). Although the sample thermocouple often failed, it was not part of the control loop so it did not affect the heating/cooling program. The protocol used was very similar to that of the STA protocol (see Appendix B). The results presented here are the successful runs with a source of high purity boron and low purity boron.

4.6.1 High Purity Boron

For the high purity run, a coarse boron shot was used (99.9999%, -8 +20 mesh, Ceradyne) which was loaded into the bottom of an MgO crucible. Magnesium turnings (99.98%, Sigma-Aldrich) were placed on top of the boron and a thermocouple was inserted through the magnesium turnings into the boron. The overall composition was 60 at% Mg and 40 at% B which was very magnesium rich compared to the stoichiometric composition of MgB_2 . After loading the sample into the graphite susceptor, the pressure

vessel was bolted together, evacuated and pressurized to 10 MPa as with the MgB_2 powder STA run. Manual control was used to bring the temperature up to ~ 600 °C and then the automatic program was started (Fig. 29). This program used a 20 °C/min. ramp rate up to 1600 °C, followed by a 10 minute dwell, and a 20 °C/min. ramp rate down to 1000 °C, followed by a 5 minute dwell and then power was shut-off. The high ramp rate was necessary so data could be collected before the gas temperature exceeded the safe limits of operation for the high pressure furnace.

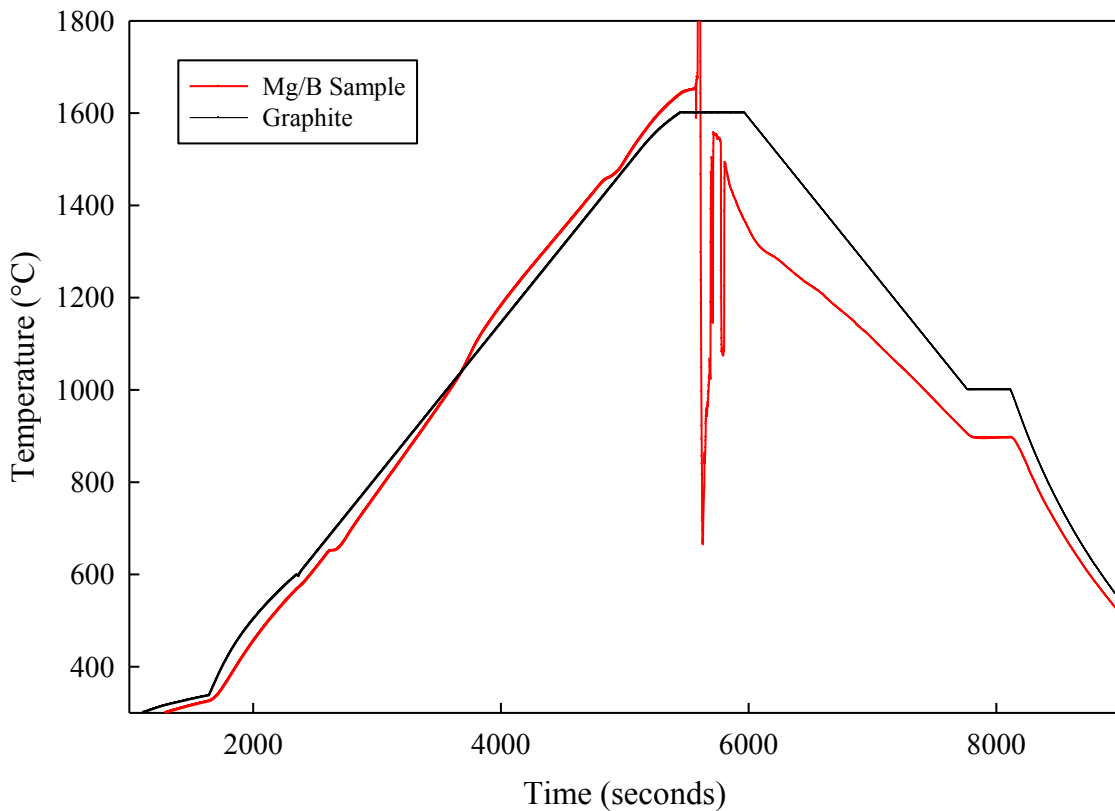


Figure 29. Programmed Run for Mg/B Elemental Mixture with High Purity Boron

At ~ 1000 °C, the sample temperature increased and then followed the same ramp rate as the graphite (this could have been due to the reaction of the magnesium with the boron). Then at ~ 1450 °C, there was a temperature lag in the sample indicating an endothermic event (Fig. 30). The derivative plot actually indicated two possible thermal events but they were not well separated. The sample temperature then increased up to ~ 1650 °C when the sample thermocouple failed.

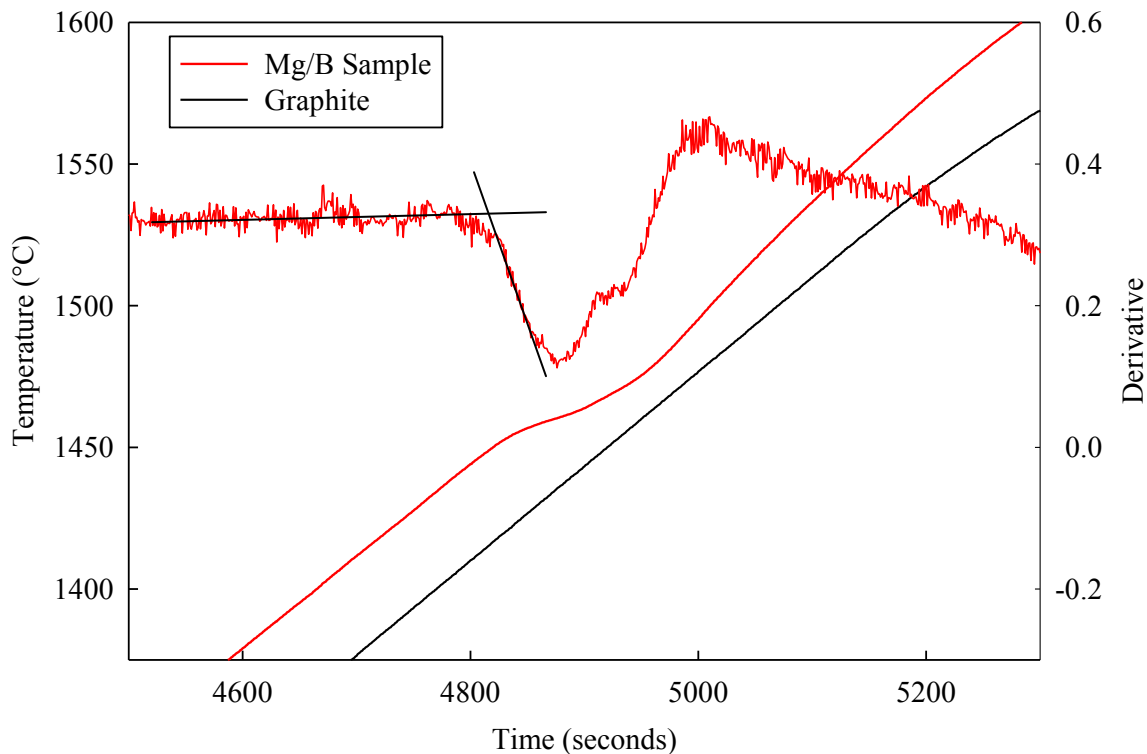


Figure 30. Programmed Run for Mg/B Elemental Mixture with derivative

After cool down, the sample was weighed, sectioned and polished. The weight loss changed the composition to 59 at% Mg and 41 at% B, but given the large excess of

magnesium it should not have had a significant effect. The sample thermocouple was embedded in the center of the ingot and it appeared that magnesium had penetrated through the tantalum sheath. Although the thermocouple was obviously attacked at high temperature, there was no indication of dissolution of the tantalum sheath or the thermocouple wires so the data collected on heating was believed to be reliable.

The backscatter images collected in the SEM indicated the presence of three phases consisting of dark cores, surrounded by a lighter phase all in a magnesium matrix (Fig. 31). Three phases were also confirmed by X-ray diffraction: MgB_2 , MgB_4 and Mg (Fig. 32). Based on the fact that backscatter electron yield is sensitive to average atomic number, the dark cores were most likely MgB_4 surrounded by MgB_2 . The presence of MgB_4 cores suggests that the ~ 1450 °C event was the peritectic decomposition of MgB_2 that had formed on heating. It is possible that the MgB_4 cores were due to an incomplete reaction between magnesium and boron that eventually would have become MgB_2 , but that would not explain the endothermic event on heating. Given that the ingot from the MgB_2 powder had similar MgB_4 cores and a similar endothermic event in that temperature range, it is more likely that the microstructure is a consequence of cooling through the peritectic temperature. An extrapolation of the baseline and the derivative slope was used to estimate the peritectic temperature as 1445 °C (Fig. 30). However, this value is probably an overestimate of the actual peritectic temperature since heating rates are known to affect phase equilibria temperatures that are measured in DTA [101]. In any case, the actual peritectic temperature for MgB_2 is considerably lower than the 1740 °C

value estimated by Kim et al. (note that their prediction of 1740 °C was for a pressure of 10 MPa, the same pressure as the high pressure furnace) [39].

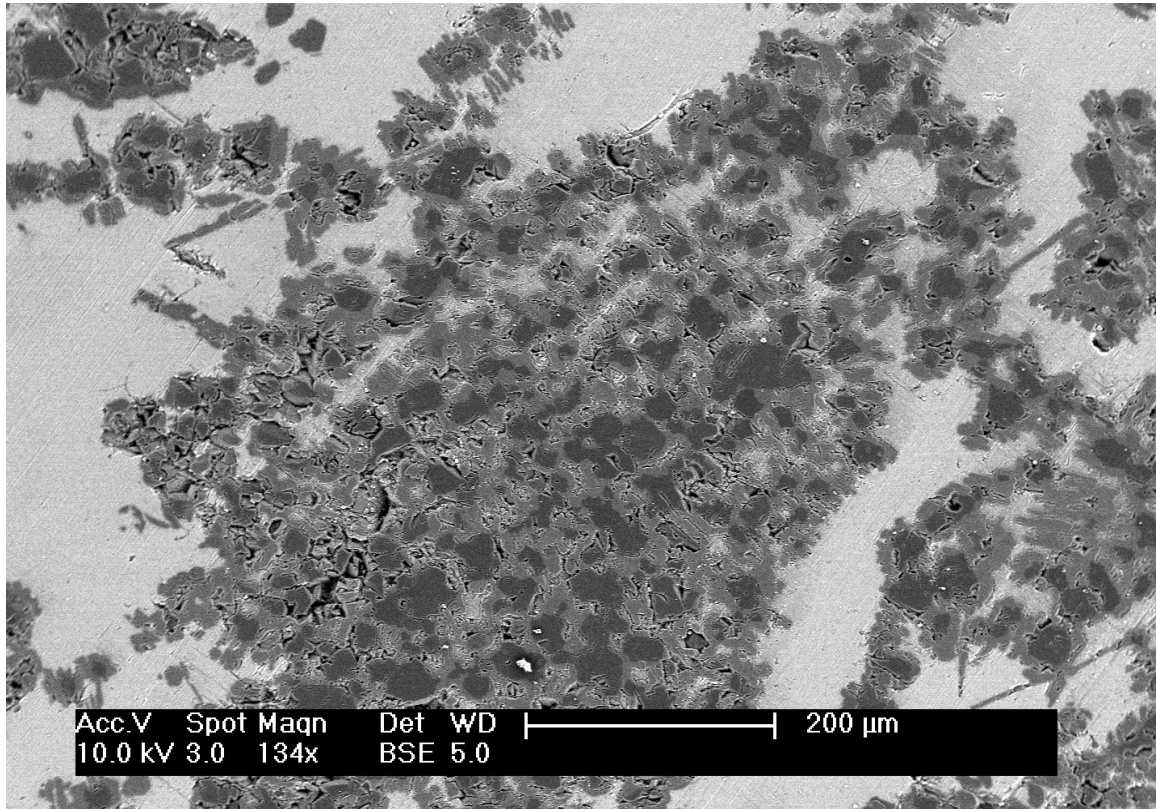


Figure 31. Backscatter SEM Image of Mg/B Ingot (dark cores are MgB₄)

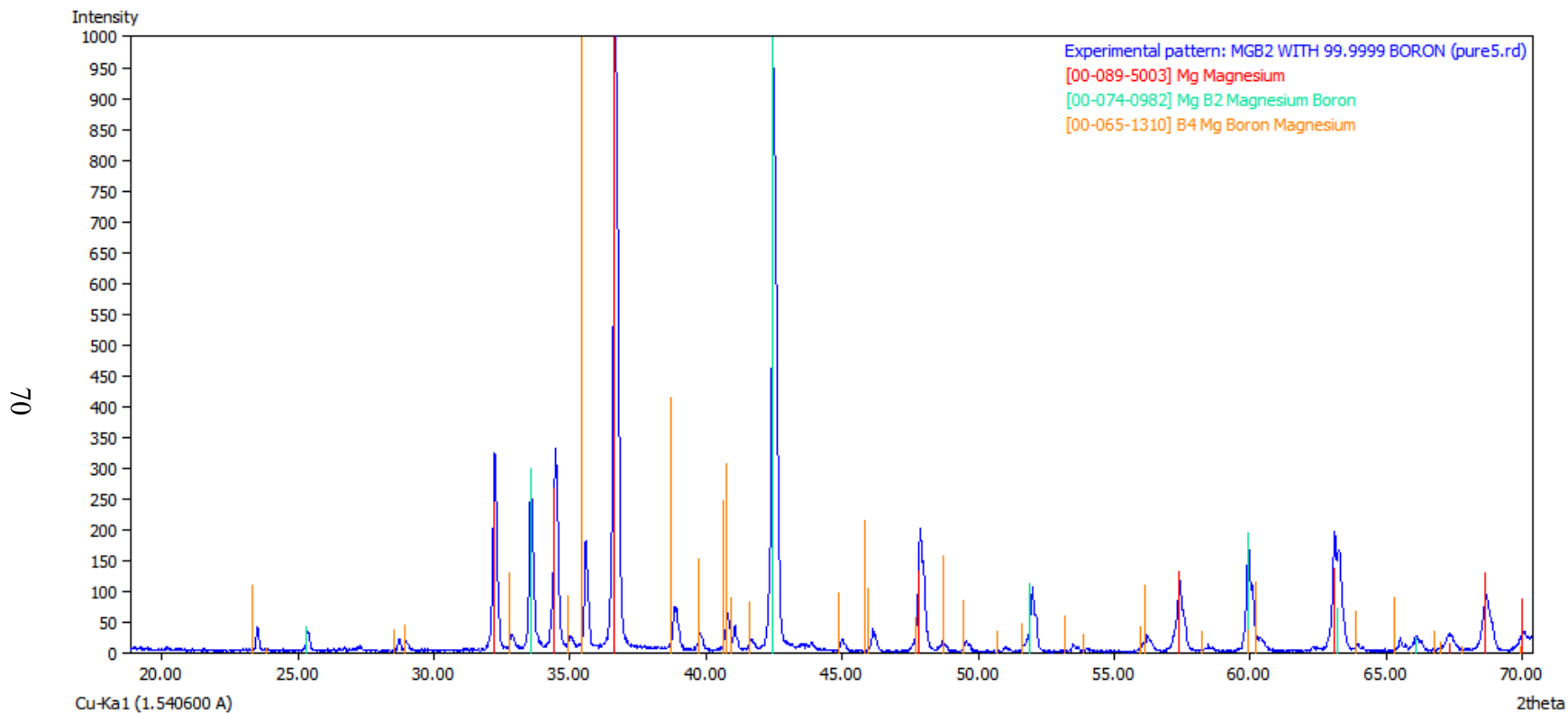


Figure 32. X-ray Diffraction of Mg/B Ingot with High Purity Boron

4.6.2 Low Purity Boron

The MgB_2 peritectic temperature was also measured using low purity boron. The boron (99.7%, -325 mesh, Sigma-Aldrich) was loaded into an MgO crucible along with magnesium turnings (99.98%, Sigma-Alrich). The mixture was ~40 at% magnesium and ~60 at% boron to produce an ingot that would be closer to the stoichiometric composition.

This run used two ramp/dwell/cool sequences to obtain two measurements of the peritectic temperature on the same ingot. Both sequences used a ramp rate of $10^\circ \text{C}/\text{min}$. for heating/cooling and a dwell at 1525°C for 15 minutes (Fig. 33). Manual power was used to bring the sample temperature up to $\sim 1000^\circ \text{C}$ when an exothermic reaction occurred that was due to the reaction of magnesium with boron (Fig. 33 inset). The power supply was then switched to automatic control at $\sim 1100^\circ \text{C}$ and the two sequences were completed without thermocouple failure. An endothermic event was observed at $\sim 1500^\circ \text{C}$ on the first run and $\sim 1490^\circ \text{C}$ on the second run as indicated by the lag in the sample temperature (Fig. 34). These two events were the only indication of a peritectic on heating, but it was not clear why the event shifted by $\sim 10^\circ \text{C}$ between the two runs. These two values were also considerably higher than the $\sim 1445^\circ \text{C}$ value that was obtained with the high purity boron run. There was a slight exothermic event on cooling for both runs which probably signified the reformation of MgB_2 on cooling (the derivative plot provided a clearer indication of the exotherm on cooling). As discussed earlier, peritectic

transformations have much slower kinetics on cooling than on heating so the weak exothermic signature was probably due to the slow kinetics on cooling.

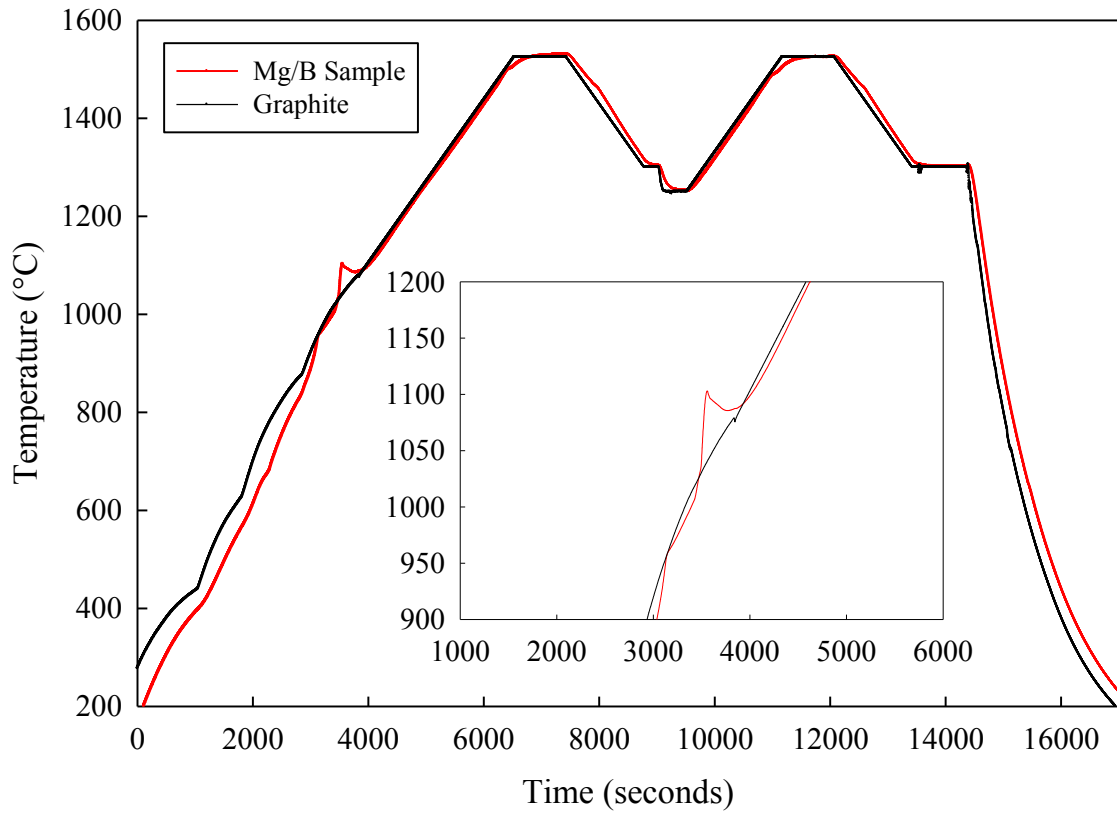


Figure 33. Programmed run of Mg/B elemental mixture with low purity boron

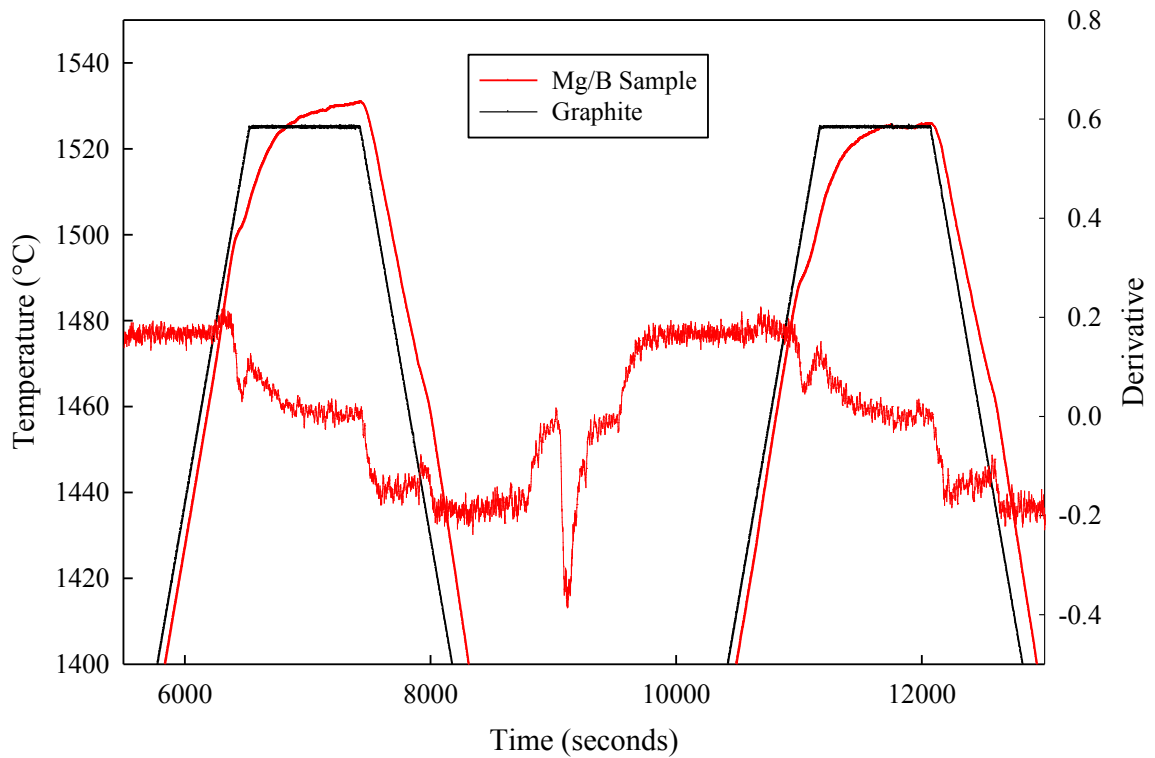


Figure 34. Programmed run of Mg/B elemental mixture with low purity boron and derivative

After cooling, the sample was weighed, sectioned and polished. Again, there was very little mass loss, less than 1 at% magnesium assuming all the weight loss was due to magnesium vapor. There was a considerable amount of porosity in the sample, but dark cores were easily discernible, although they were much smaller than the Mg/B ingot from high purity boron (Fig. 35). The larger MgB_4 cores in the high purity ingot were probably due to coarsening at high temperature whereas this ingot only went to ~ 1525 °C. The X-ray diffraction data confirmed that MgB_2 and Mg were present, but only a few peaks

matching MgB_4 were detectable (Fig. 36). This similarity to the other samples suggested that the dark cores were MgB_4 and this was confirmed with Electron Microprobe data collected by John Donovan at the University of Oregon (see Tables 1-2 and Figures 37 and 38). The compositions for both the dark phase and the light phase were very close to the expected stoichiometric compositions for MgB_4 and MgB_2 respectively. A considerable amount of oxygen was also detected which was unexpected, and the average oxygen level was higher in the MgB_2 than in the MgB_4 .

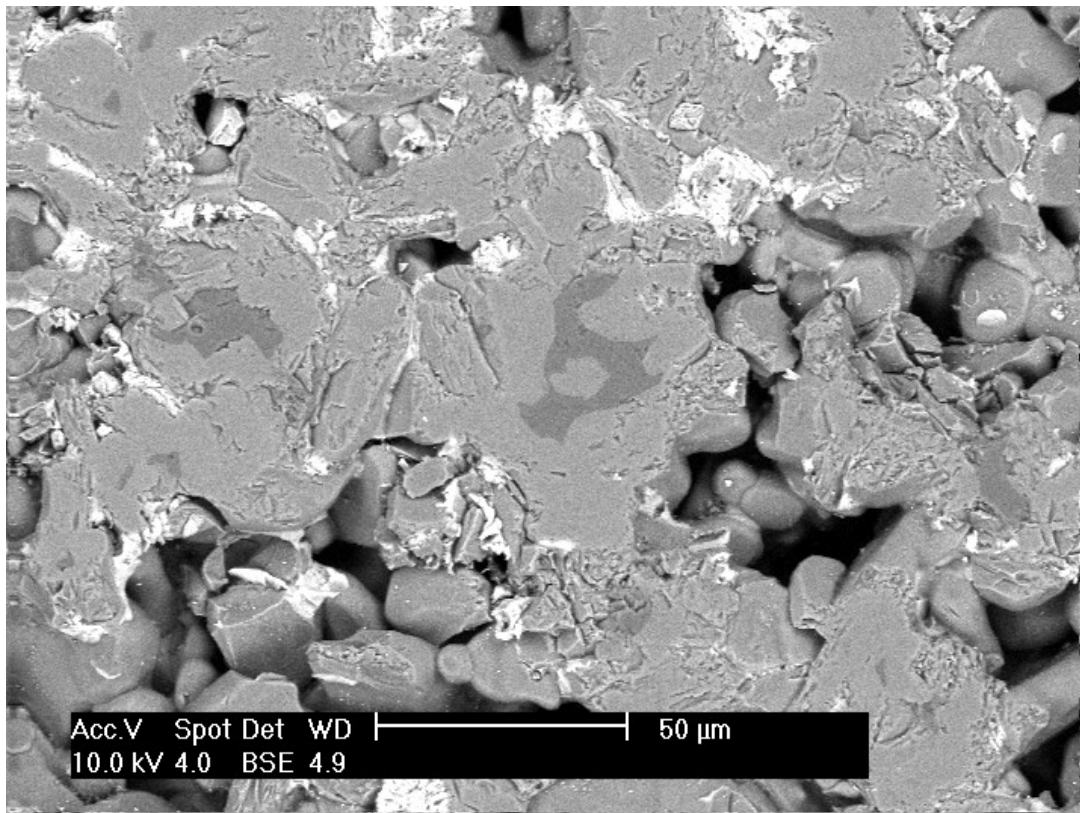


Figure 35. Backscatter SEM Image of Mg/B ingot with low purity boron

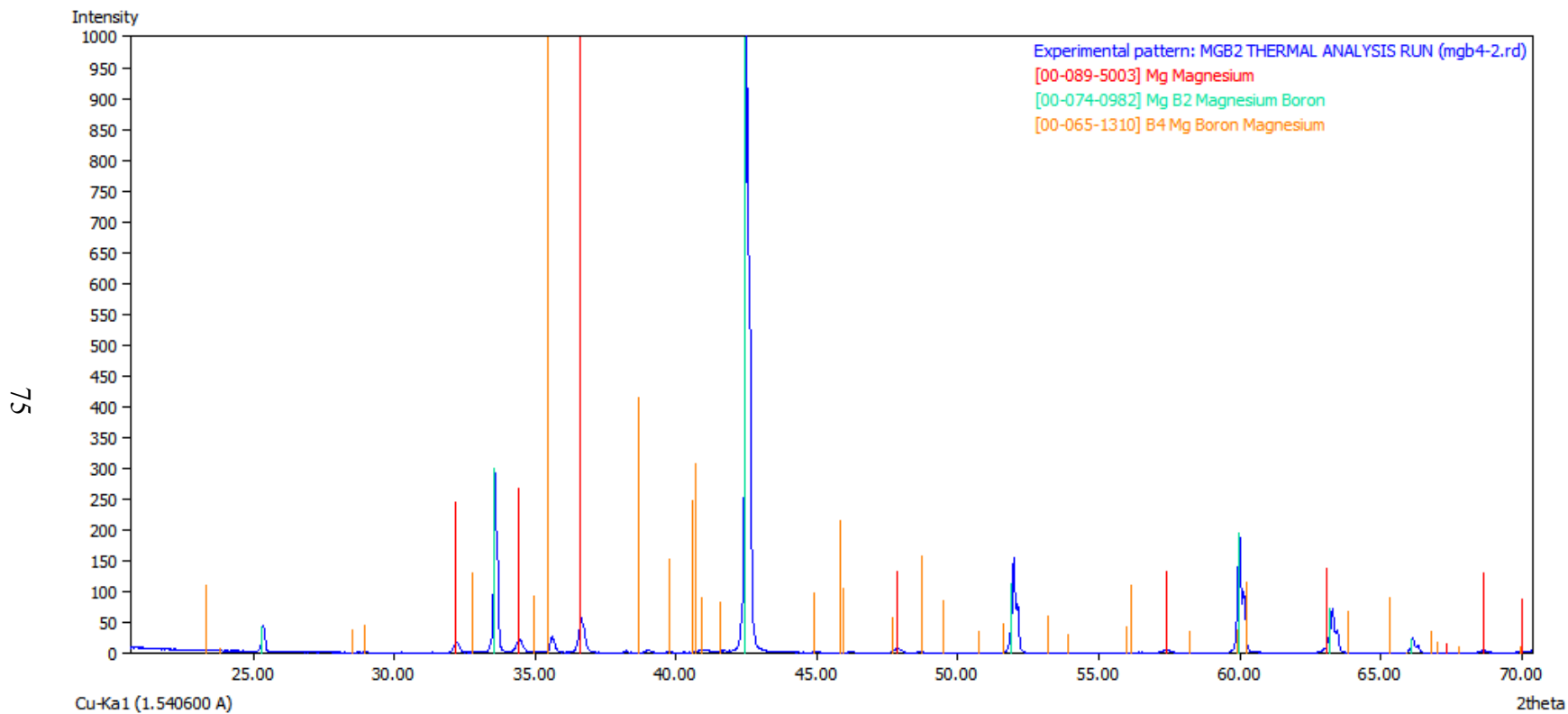


Figure 36. X-ray Diffraction of Mg/B Ingot with Low Purity Boron

Table 1. EPMA data on MgB₄ Phase

SPOT	Mg at%	B at%	O at%	TOTAL
108	20.4	79.3	0.3	100
109	20.2	79.5	0.3	100
110	20.2	79.5	0.3	100
111	20.3	79.4	0.2	99.9
112	20.4	79.3	0.3	100
113	20.4	79.3	0.3	100
114	20.5	79.2	0.3	100
115	20.5	79.2	0.3	100
116	20.3	79.4	0.3	100
117	20.2	79.5	0.4	100.1
Average	20.3	79.4	0.3	

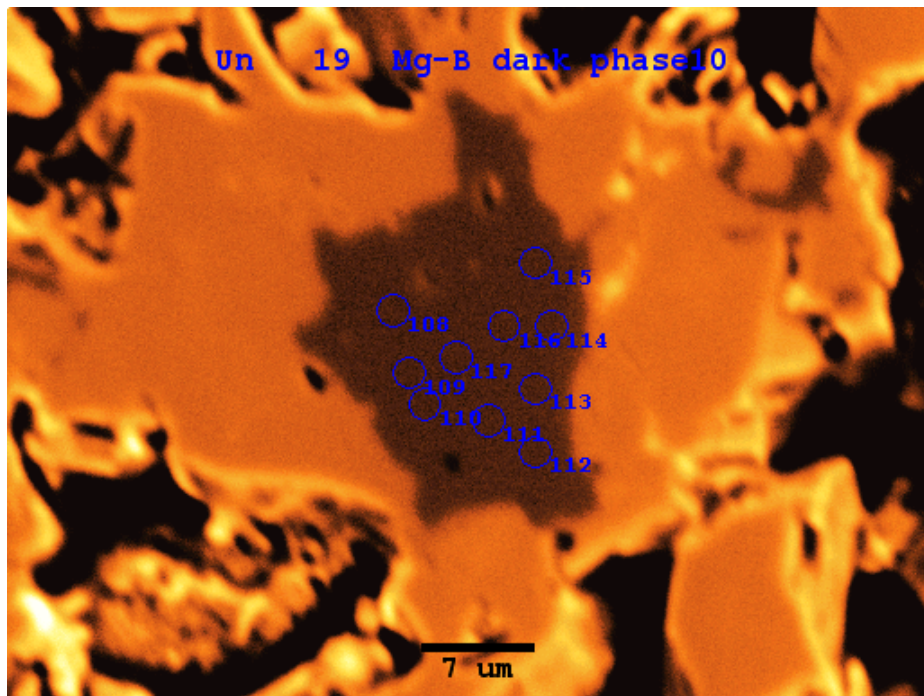


Figure 37. Location of EPMA Electron Beam (MgB₄ core)

Table 2. EPMA data on MgB₂ Phase

SPOT	Mg at%	B at%	O at%	TOTAL
140	32.5	67.1	0.4	100
141	32.6	66.9	0.5	100
142	32.7	66.7	0.6	100
143	32.4	67.2	0.4	100
144	32.5	66.7	0.8	100
145	31.9	67.8	0.4	100.1
146	32.0	67.6	0.4	100
147	33.7	65.9	0.4	100
148	33.8	65.8	0.4	100
149	34.3	64.8	0.9	100
150	32.2	67.3	0.5	100
Average	32.8	66.7	0.5	

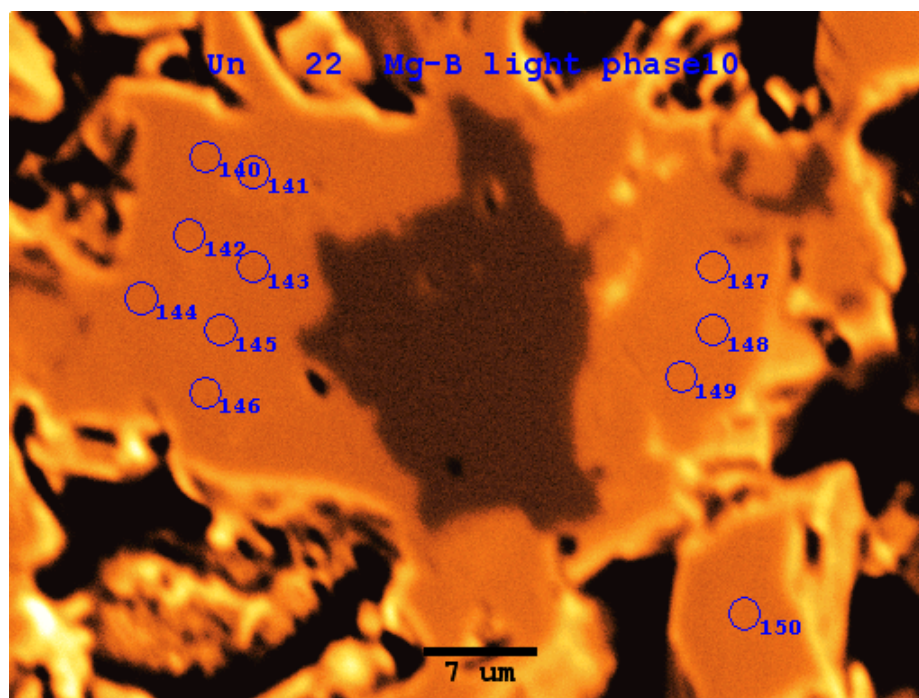


Figure 38. Location of EPMA Electron Beam (MgB₂)

The estimated peritectic temperatures are summarized in Table 3. It was unclear why the peritectic temperature was higher for the MgB₂ from the low purity boron as opposed to the high purity boron. The low purity boron was quoted to be 99.7% pure on a metals basis which did not include light elements such as carbon. Carbon is a common impurity for boron and is known to substitute on the boron site in the MgB₂ structure so a portion of the boron powder was sent to LECO Corporation for carbon analysis. They measured a carbon level of ~0.7 wt% so the actual purity was closer to 99%. The high purity boron was confirmed by Ceradyne to have less than 100 ppm carbon. That suggested it was the carbon in the low purity boron which increased the peritectic temperature for MgB₂. This highlights the need for high purity reagents in any phase diagram study. The change in the peritectic temperature also indicated that carbon changes the thermodynamic stability of MgB₂ compared to any competing phases. This may explain the widely different values estimated by Cook et al. and Brutti et al. for the decomposition temperature of MgB₂ at 0.1 MPa [32], [35]. It is not clear why the peritectic appeared to change from 1500 °C to 1490 °C between the first and second ramp/dwell/cool cycle. Perhaps some carbon segregation in the ingot was responsible or it could have been due to thermocouple drift.

Table 3. Estimated Peritectic Temperatures for MgB₂

Sample	Temperature (°C)
Mg/B with High Purity B	1445
Mg/B with Low Purity B	1490-1500

4.7 A.C. Susceptibility

The A.C. Susceptibility method was used to measure the superconducting transition temperature of all three ingots (ingot from MgB₂ powder, Mg/B with high purity boron, Mg/B with low purity boron). A 10 Oe (0.001 T) oscillating field was applied at 1000 Hz and all samples were zero-field-cooled. There was essentially no difference between the ingot from MgB₂ powder and the Mg/B ingot with low purity boron. This was surprising given the 0.7 wt% carbon in the low purity boron, but it is possible the carbon was distributed inhomogeneously. The high purity ingot had a broader superconducting transition which was unexpected since superconductors in high purity form tend to have very sharp superconducting transition temperatures. It was not clear why the transition was broader, but one possibility is strain effects given the very inhomogeneous nature of the high purity ingot since it had much larger MgB₄ cores (note the 200 μm scale bar in Fig. 31). These large cores were probably due to the high temperatures reached during the furnace run.

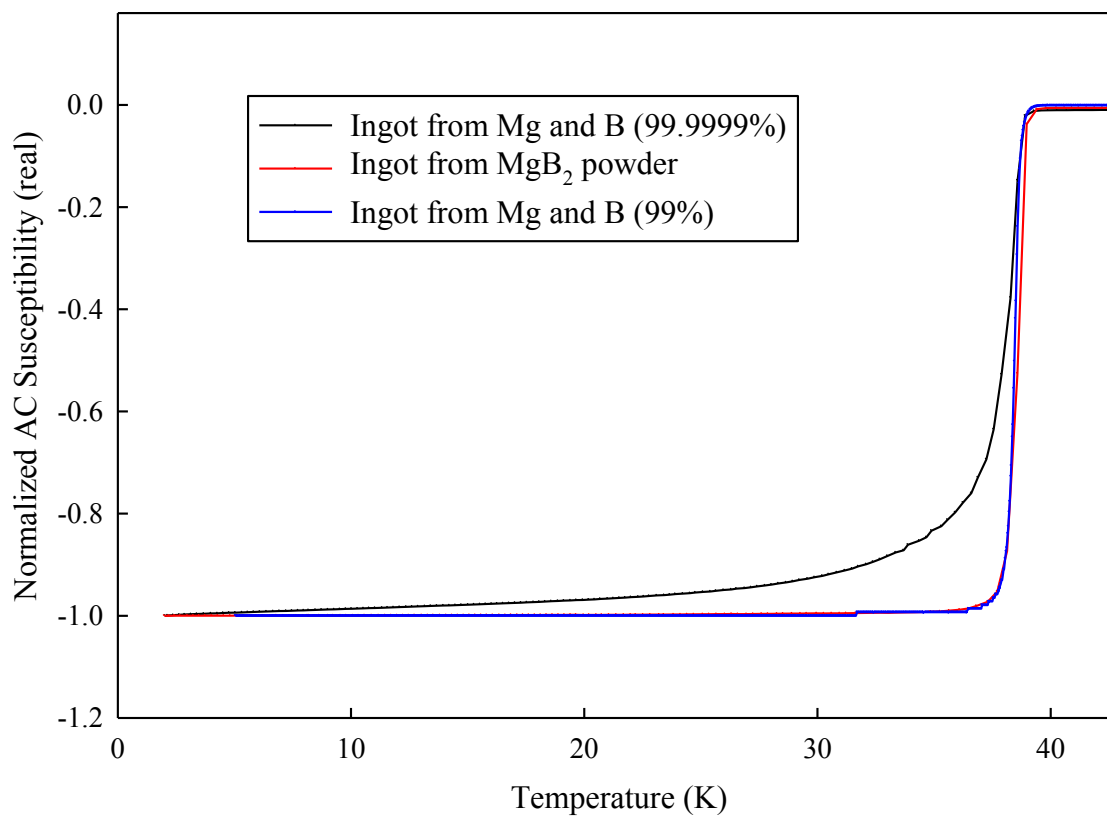


Figure 39. A.C. Susceptibility of all three ingots

4.8 Environmental Degradation of MgB₂ Ingots

While investigating the MgB₂ peritectic, it was noticed that the Mg/B ingots would slowly turn into powder over the course of several weeks if they were left on the counter or in the fume hood (Fig. 40). However, this degradation was only noticeable in the spring/summer, but not in the fall/winter. Also, degradation did not occur if the ingots were stored in a dessicator. These observations suggested that humidity was playing a

role since humidity is high in the summer for central Ohio (the lab was not humidity controlled).



Figure 40. Environmental degradation of Mg/B ingot from low purity boron

Some of the powder produced by this process was collected and the superconducting transition was measured using the A.C. Susceptibility method and compared to the original ingot (the Mg/B ingot made with low purity boron). The T_c onset had not changed, but the superconducting transition was much broader as indicated by the real component of the A.C. Susceptibility (Fig. 41). Also, the imaginary

component of the A.C. Susceptibility data indicated that the superconducting portion of the powder was inhomogeneous and the T_c distribution appeared to be bimodal (Fig. 42).

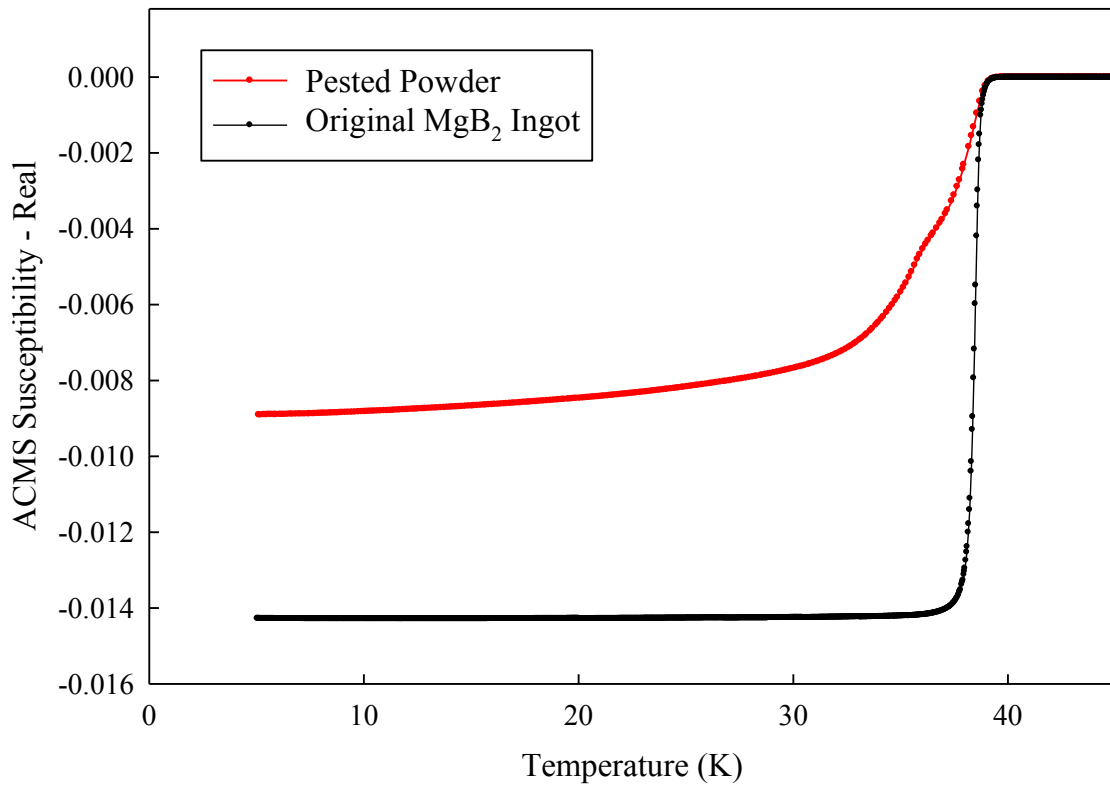


Figure 41. A.C. Susceptibility (real) of original ingot and pested powder (1000 Hz and 10 Oe applied field)

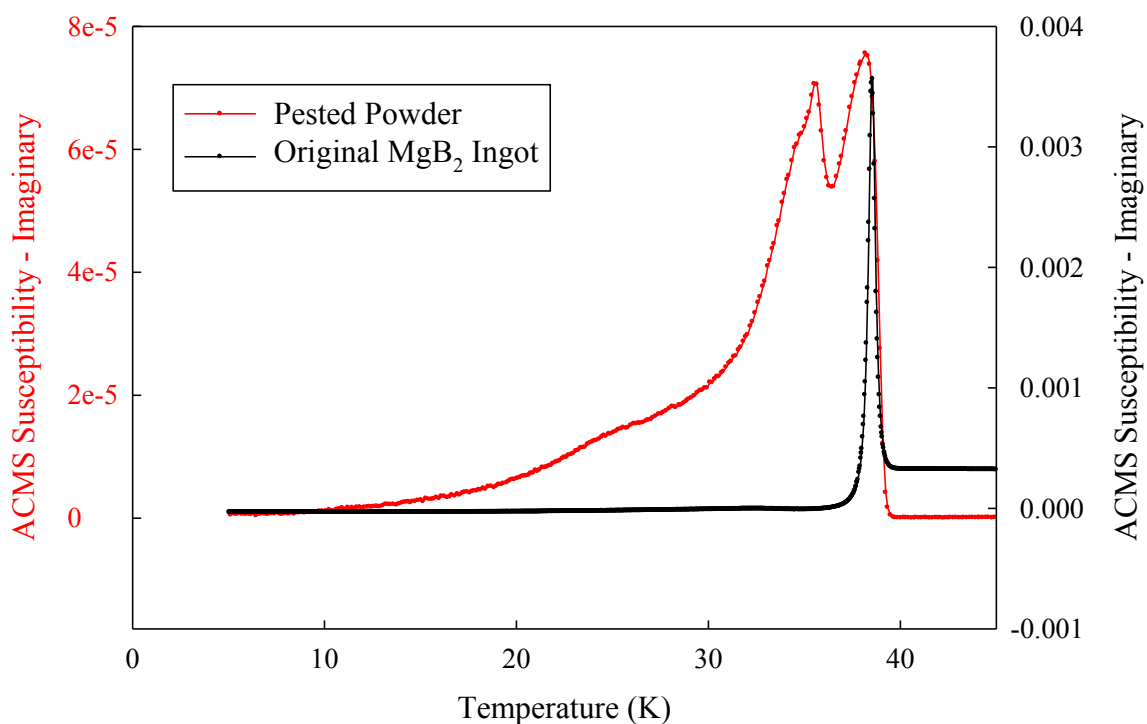


Figure 42. A.C. Susceptibility (imaginary) of original ingot and pested powder (1000 Hz and 10 Oe applied field)

This environmental degradation is probably an example of what is referred to in the literature as “pestering” or “pest degradation” [102]. Pestering refers to some process that transforms a solid material into a powder which may be due to several possible mechanisms. In this case, the summer/winter behavior suggests H₂O or H₂O-enhanced attack of grain boundaries in the material. The T_c measurements confirmed that some of the powder was still superconducting so at least some of the MgB₂ grains were still intact. An in-depth investigation of this phenomenon was not pursued since it was not central to the determination of the peritectic temperature.

CHAPTER 5: HOMOGENEOUS CARBON DOPING OF MgB₂

Homogeneous doping of MgB₂ remains a significant challenge that is not easy to accomplish with lower temperature synthesis methods. The most relevant dopant for MgB₂ continues to be carbon since it is the only dopant that significantly increases the upper critical field which is important for many potential applications. However, there is still uncertainty as to how much carbon can actually be introduced into MgB₂. Fortunately, the high pressure furnace makes it possible to synthesize much more homogeneous samples that can answer this question.

5.1 Synthesis

The carbon-doped MgB₂ samples were synthesized from B₄C powder (98%, <10 micron particle size, Sigma-Aldrich) and Mg turnings (99.98%, Sigma-Aldrich) in the same MgO crucibles as used above. It was not possible to use the STA method due to aggressive attack of the tantalum sheath of the sample thermocouple so a standard ramp, dwell, cool sequence was used with the graphite thermocouple as the control thermocouple. Three samples were prepared with a ramp of 20 °C/min. followed a dwell period of 10 min. at 1530 °C (sample 1), 1600 °C (sample 2), and 1700 °C (sample 3), followed by a 20 °C/min. cool. Those temperatures were based on the graphite thermocouple and thus were only approximate to the sample temperature. The molar

ratios of Mg:B₄C used for these samples were the following: 3:1 for the 1530 °C sample, 4:1 for the 1600 °C sample, and 5:1 for the 1700 °C sample. An increasing molar ratio of magnesium was used to ensure that even with magnesium losses at high temperature, there would be an excess of magnesium to react with the boron. For safety reasons, the high pressure furnace could not be operated above 1700 °C so that was the maximum temperature explored in this carbon doping study.

5.2 Microstructure

After cool down, the samples were sectioned and polished. Based on SEM images taken with the backscatter detector and X-ray diffraction data, the samples appeared to consist of 3 phases: Mg, MgB₂C₂ and MgB₂ with significantly shifted peaks so the phase was labeled as Mg(B_{1-x}C_x)₂ (Figs. 43-46). Interestingly, the (001) and (002) peaks were not significantly shifted indicating that only the *a* lattice parameter was changed. Backscatter electron yield is sensitive to average atomic number so the dark phase was identified as MgB₂C₂, the grey phase as Mg(B_{1-x}C_x)₂ and the white phase as Mg. The Mg phase was not readily discernible in the 1530 °C sample although the X-ray diffraction data indicated it was present. The grain size of the Mg(B_{1-x}C_x)₂ and MgB₂C₂ increased with temperature (notice the scale bars change from 5 μm to 20 μm to 50 μm). The microstructure of the 1700 °C sample was unique in that it had large needle-like grains for both the Mg(B_{1-x}C_x)₂ phase and MgB₂C₂ phase. This suggests that at sufficiently high temperatures there is preferential growth in certain crystallographic directions for both

phases. There was no indication that the $\text{Mg}(\text{B}_{1-x}\text{C}_x)_2$ phase went through a peritectic transition unlike the MgB_2 sample in the previous chapter that had 0.7 wt% carbon. These samples suggest that the addition of carbon raises the peritectic temperature for carbon doped MgB_2 even further, possibly even above 1700 °C. Also, the presence of MgB_2C_2 indicates that the $\text{Mg}(\text{B}_{1-x}\text{C}_x)_2$ must contain the maximum amount of carbon possible for MgB_2 , especially since the starting powder was B_4C and not a mixture of boron and carbon. Each B_4C particle must have reacted with the Mg and split into MgB_2C_2 and $\text{Mg}(\text{B}_{1-x}\text{C}_x)_2$ and the increase in grain size with temperature was just the result of coarsening.

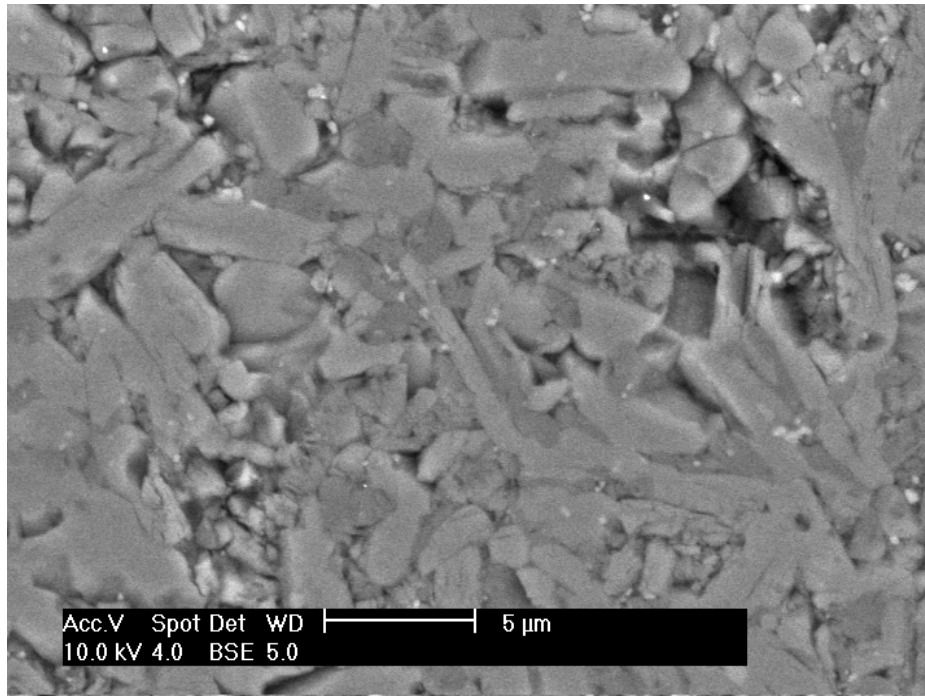


Figure 43. 1530 °C sample with $\text{Mg}(\text{B}_{1-x}\text{C}_x)_2$ (grey) and MgB_2C_2 (dark)

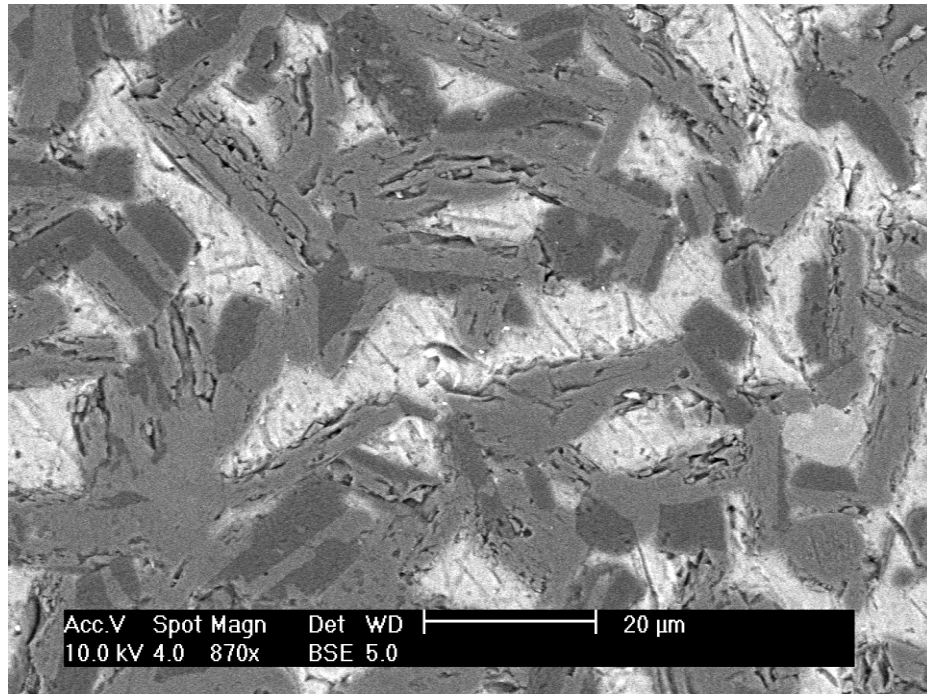


Figure 44. 1600 °C sample with Mg (white), Mg(B_{1-x}C_x)₂ (grey) and MgB₂C₂ (dark)

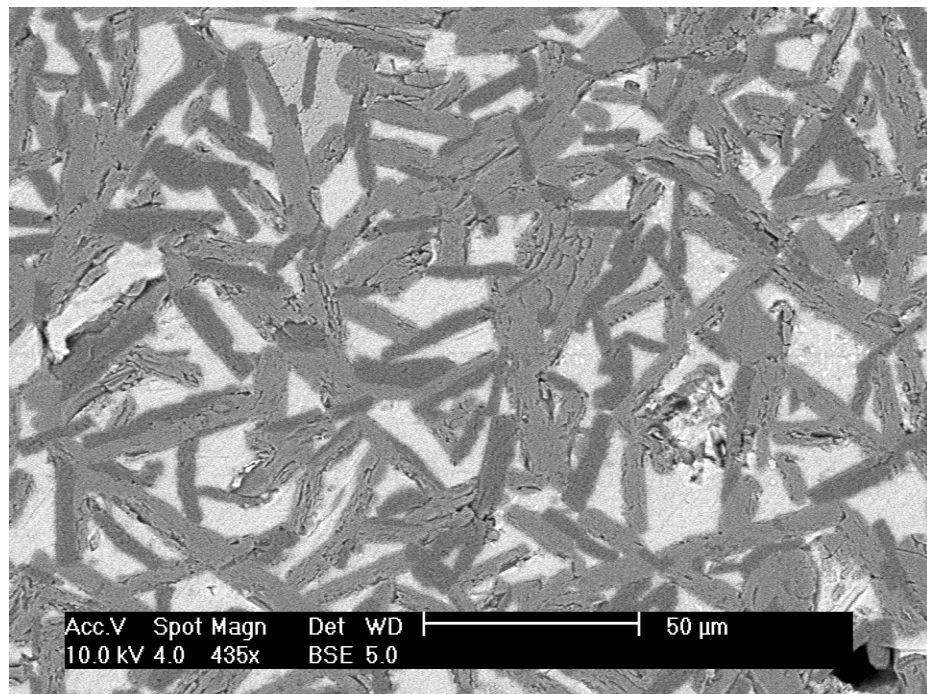


Figure 45. 1700 °C sample with Mg (white), Mg(B_{1-x}C_x)₂ (grey) and MgB₂C₂ (dark)

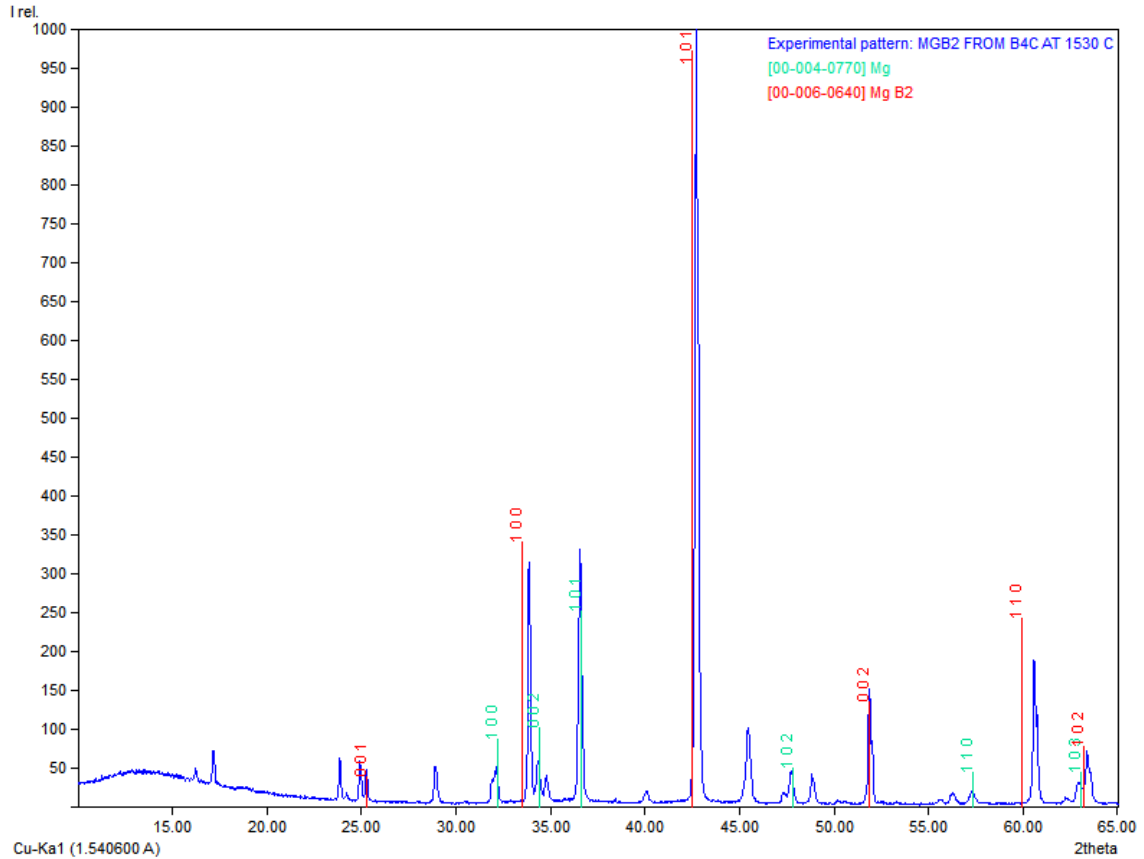


Figure 46. X-ray Diffraction of 1530 °C Ingot

The 1530 °C sample was characterized using EPMA by John Donovan at the University of Oregon. The results confirmed that the dark phase observed in the SEM was MgB_2C_2 (Table 4) and the grey phase was carbon-doped MgB_2 (Table 5). Silicon and oxygen were also detected but had a higher concentration in the MgB_2C_2 . Curiously, the measured carbon concentrations levels were greater than the boron concentration levels for the MgB_2C_2 and the Mg concentration levels were higher than the expected value of 20 at%. For the carbon-doped MgB_2 , the Mg concentration levels were higher than the theoretical value of 33.3% and the (B + C) concentrations did not add up to the

expected value of 66.6%. The average carbon concentration level was 5.9 at% although there was considerable scatter in the individual measurements for carbon.

Table 4. EPMA data on MgB_2C_2

SPOT	Mg at%	B at%	O at%	C at%	Si at%	Total	B + C
19	23.7	36.3	3.0	37.0	0.0	100	73.3
20	21.2	28.6	4.4	45.5	0.3	100	74.1
21	23.4	34.9	3.3	38.3	0.1	100	73.2
22	23.8	33.1	5.6	37.4	0.1	100	70.5
23	23.7	33.8	6.3	36.2	0.1	100.1	70
24	21.9	27.6	7.3	42.9	0.3	100	70.5
Average	23.0	32.4	5.0	39.6	0.2		71.9

Table 5. EPMA data on $Mg(B_{1-x}C_x)_2$

SPOT	Mg at%	B at%	O at%	C at%	Si at%	Total	B + C
25	37.7	56.1	1.8	4.4	0.0	100	60.5
26	37.6	54.1	1.9	6.3	0.1	100	60.4
27	35.9	54.3	1.8	7.9	0.1	100	62.2
28	36.9	55.3	2.2	5.7	0.0	100.1	61
29	37.1	55.3	2.1	5.4	0.0	99.9	60.7
Average	37.0	55.0	2.0	5.9	0		61.0

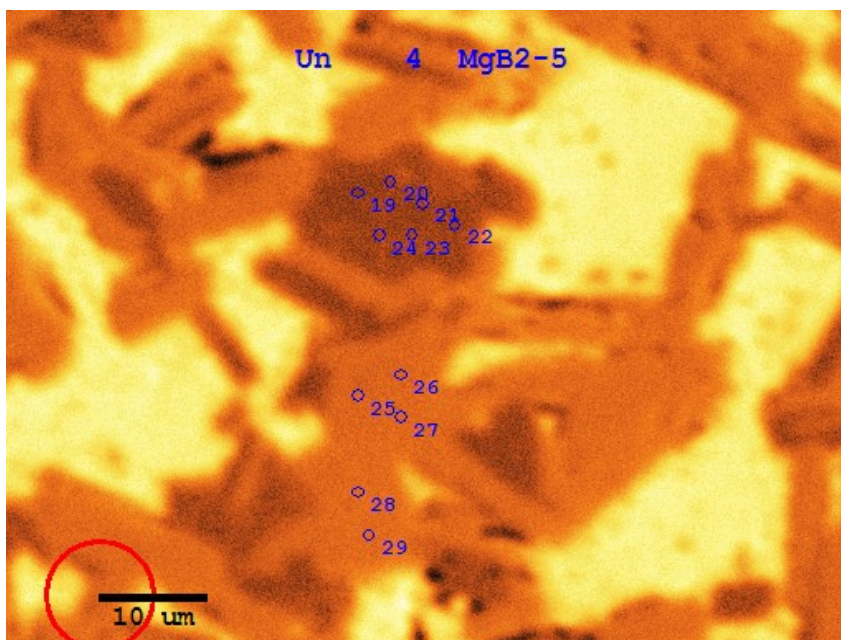


Figure 47. Location of EPMA Electron Beam for MgB_2C_2 and $\text{Mg}(\text{B}_{1-x}\text{C}_x)_2$

A limited TEM investigation was initiated on the 1530 °C sample. A $\sim 4 \mu\text{m} \times \sim 10 \mu\text{m}$ piece was extracted by Dan Huber using the Focused Ion Beam on the Helios 600 instrument in the Center for Electron Optics Facility (CEOF). Imaging was done by Henk Colijn on the Tecnai F20 TEM using High Angular Annular Dark Field (HAADF) imaging. The sample appeared to contain several $\text{Mg}(\text{B}_{1-x}\text{C}_x)_2$ and MgB_2C_2 grains, but there were also several inclusions which were not expected (Fig. 48). Further analysis using EDS indicated that these inclusions were most likely MgO (Fig. 49-50). Since this sample was milled from the ingot at random, it suggested that the entire sample was probably filled with oxide inclusions (and most likely the 1600 °C and 1700 °C samples as well). These oxide inclusions were not detected by X-ray diffraction but they may explain the oxygen detected in EPMA for both the MgB_2C_2 and $\text{Mg}(\text{B}_{1-x}\text{C}_x)_2$. Any oxide

inclusions buried below the surface would still contribute an oxygen x-ray signal assuming they were close enough to the surface. The oxide inclusions could just be the result of using a fine B_4C powder which probably contained a surface oxide on each particle. That surface oxide (perhaps B_2O_3) may have been reduced by Mg to form MgO which is one possible origin for these oxide inclusions. It is also possible that the oxygen detected via EPMA on the MgB_2/MgB_4 ingot was due to oxide inclusions.

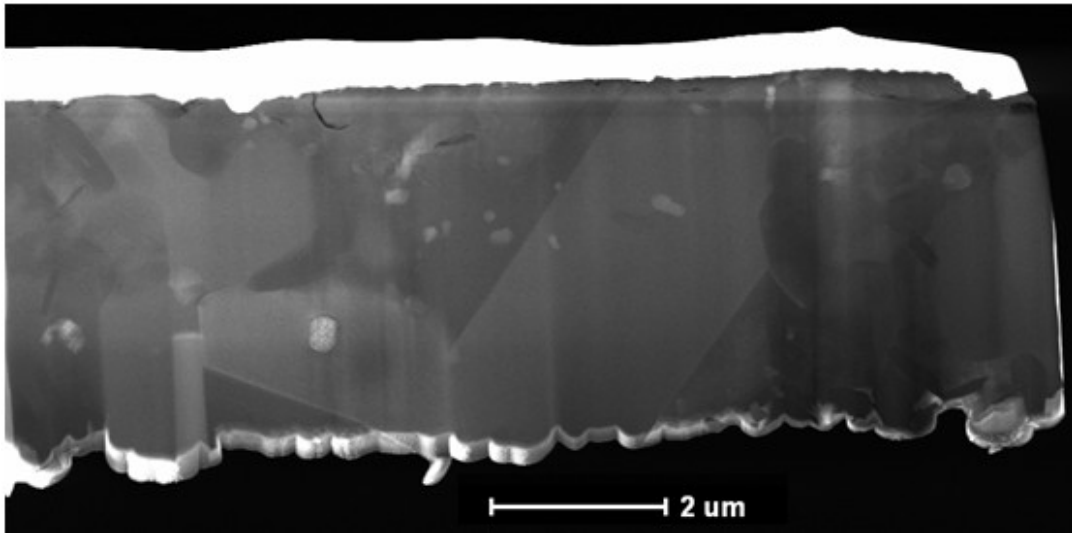


Figure 48. TEM image of sample from 1530 °C Ingot (HAADF)

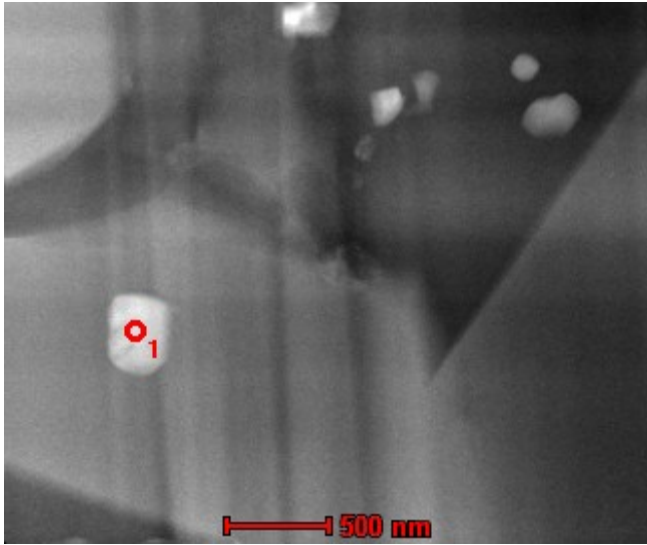


Figure 49. Oxide Inclusion in TEM

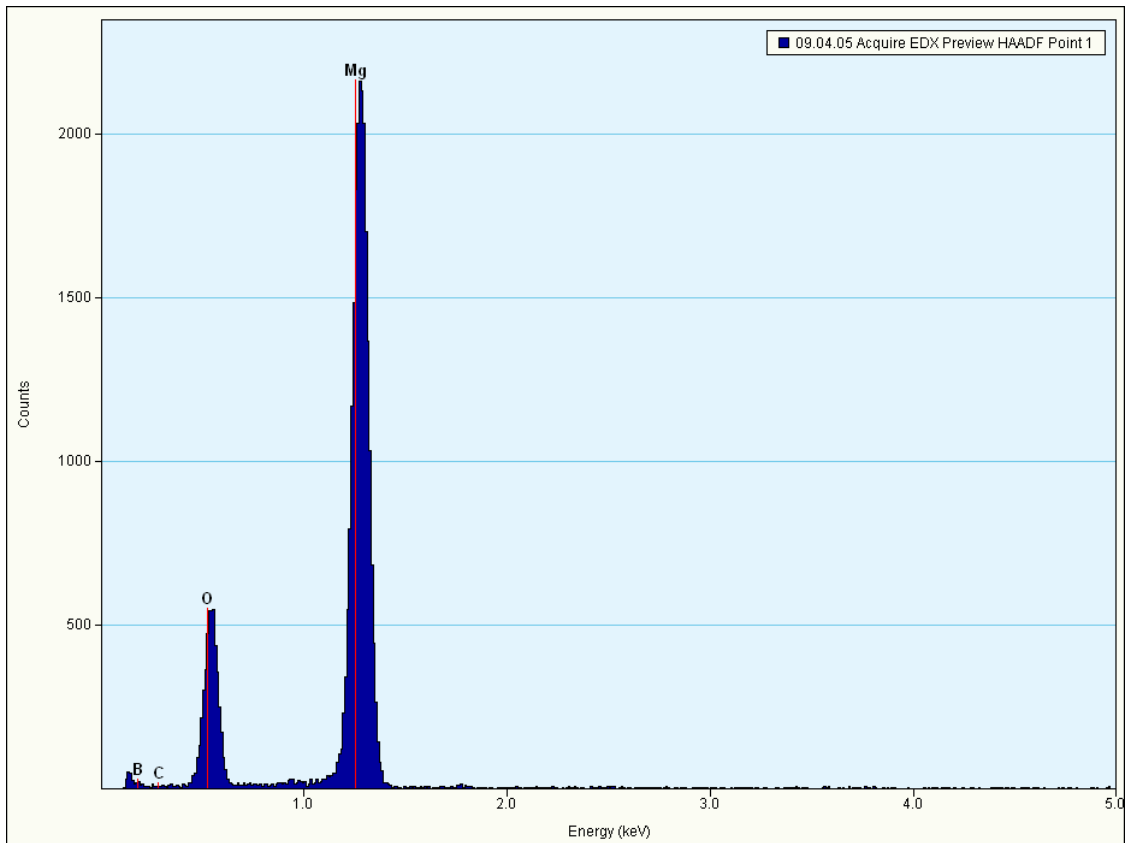


Figure 50. EDS Analysis of MgO Inclusion

5.3 Superconducting Properties

The superconducting properties of these ingots were studied using A.C. Susceptibility and Vibrating Sample Magnetometry. All three samples had essentially the same superconducting behavior so only data from the 1700 °C sample will be shown. The A.C. Susceptibility data was collected upon warming the sample at 0.5 K/min. using a 10 Oe (0.001 T) alternating magnetic field at 1000 Hz. Data was also collected for a series of background (static) magnetic fields in 0.5 T increments after zero field cooling the sample for each run. The T_c dropped to ~23 K at zero field which was a substantial drop from that of pure MgB₂, which has a T_c of ~39 K (Fig. 51). The 23 K value was close to the T_c measured by Avdeev et al. who reacted B₄C with Mg at 1200 °C for 24 hours (their reported T_c was ~22 K) [71]. As the background magnetic field increased, the T_c decreased and the transition broadened (Fig. 51). The imaginary portion also showed a peak (Fig. 52). However, looking back to the real portion of the curve, an interesting phenomena was seen. For some intermediate DC fields (2.5-5.0 T), the data taken on warming suggested that the superconducting portion of the sample increased which was unusual. This was reproducible with all three samples and did not change with sample orientation. The “bump” was initially surprising, but can be understood by looking at complementary M-H information as measured using VSM.

The VSM measurements were collected using a constant measurement of the magnetic response of a sample as the magnetic field was swept from positive to negative

and back again. Data was collected at 5, 10, and 15 K using a sweep rate of 100 Oe/sec. or 0.01 T/sec. (Figs. 52-53). The loops were fairly reversible, but did show irreversible signatures at lower fields, as is common. However, the M-H loops also showed small increases in the irreversible magnetization at higher fields (between 3.5-6.5 T in the 5 K data), an effect which is sometimes referred to as a “fishtail” effect. These regions were significantly smaller at 10 K and shifted to lower fields (2.5-4.5 T). At 15 K, there was no indication of a second region of irreversibility. The presence of the fishtail effect explains the unusual A.C. Susceptibility data which was measuring the same sample response but at constant magnetic field and changing temperature instead of VSM which was constant temperature but changing magnetic field. This can be understood if one realizes that the A.C. susceptibility curve reports the local slope of an effective M-H loop which is probed with the aid of the background DC field that is applied at the same time as the A.C. signal. That is, as the DC background field approached the field of the fishtail effect, the local slope (and the AC susceptibility value) changed, dropping down again once the DC field moved through the fishtail region. In any case, this indicates some additional flux pinning in this field range. One possible cause of this extra pinning is that there may have been small regions of material inside the carbon doped MgB₂ (pins) that had different properties than the bulk (possibly precipitates or second phase particles). These areas may have been superconducting themselves or superconducting due to proximity effect, but at high field they transitioned to the normal state before the bulk of the superconductor. If these inhomogeneous areas were of the right size, they then would have provided flux pinning sites which would explain the small second loop seen in the

VSM data. However, the main focus of this study was to measure the solubility limit for carbon in MgB₂ so an in depth investigation into this fishtail effect was not pursued. Future work may entail the study of this unusual behavior in these carbon doped samples and possibly how to control it so flux pinning can be enhanced.

Finally, A.C. Susceptibility data was used to extract the upper critical field, B_{c2} , from the carbon doped 1700 °C ingot and the MgB₂ made from high purity boron (Fig. 55). Unfortunately, only a limited amount of data was collected on the high purity ingot, but data up to 8 Tesla was collected on the 1700 °C carbon doped sample. These B_{c2} values are based on taking the 90% value of the transition to the normal state in the real portion of the A.C. Susceptibility signal. The carbon doped sample had a steeper slope ($dB_{c2}/dT = -0.77$ in 7-8 Tesla range) suggesting that carbon was effective at increasing the upper critical field which is consistent with the reported effects of carbon doping.

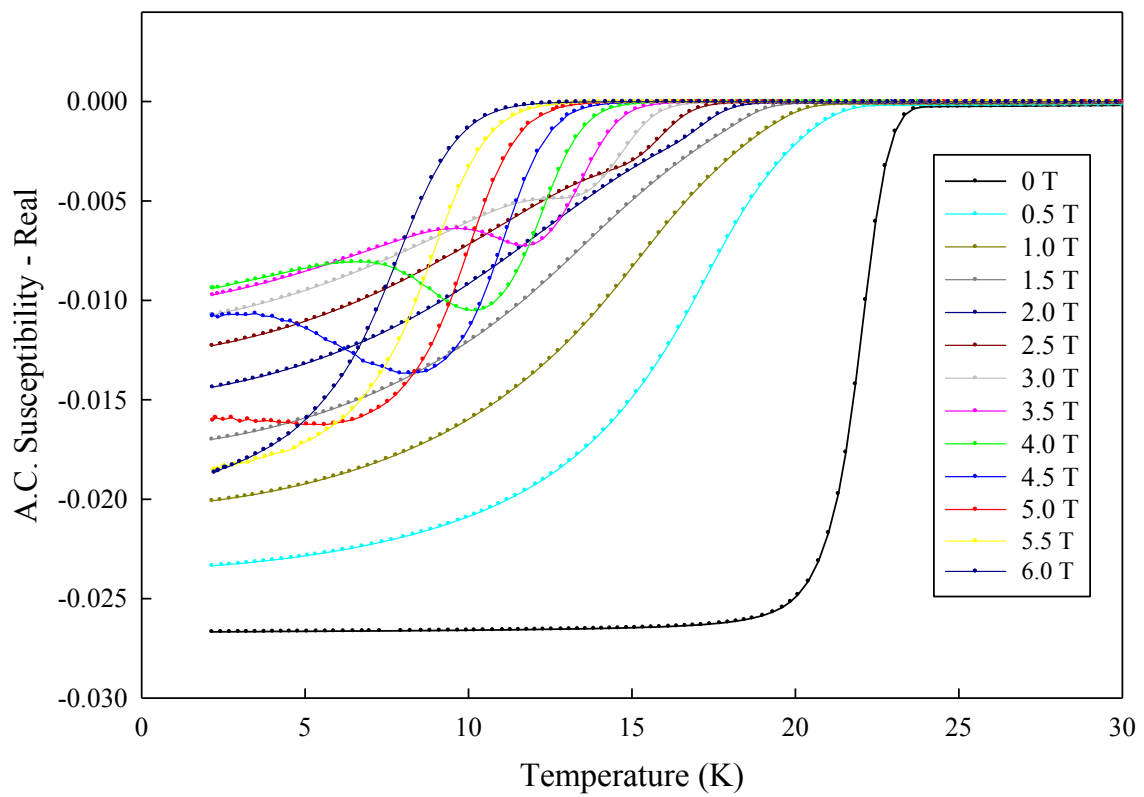


Figure 51. A.C. Susceptibility (real) of 1700 °C Ingot

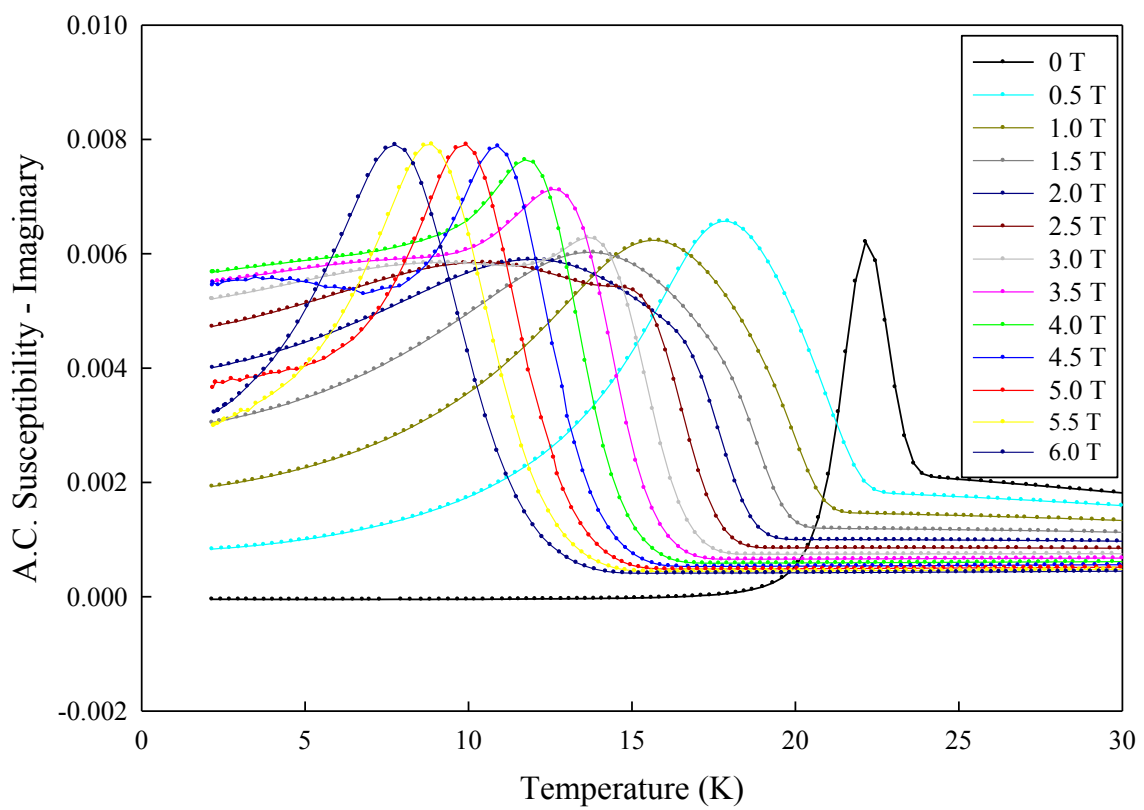


Figure 52. A.C. Susceptibility (imaginary) of 1700 °C Ingot

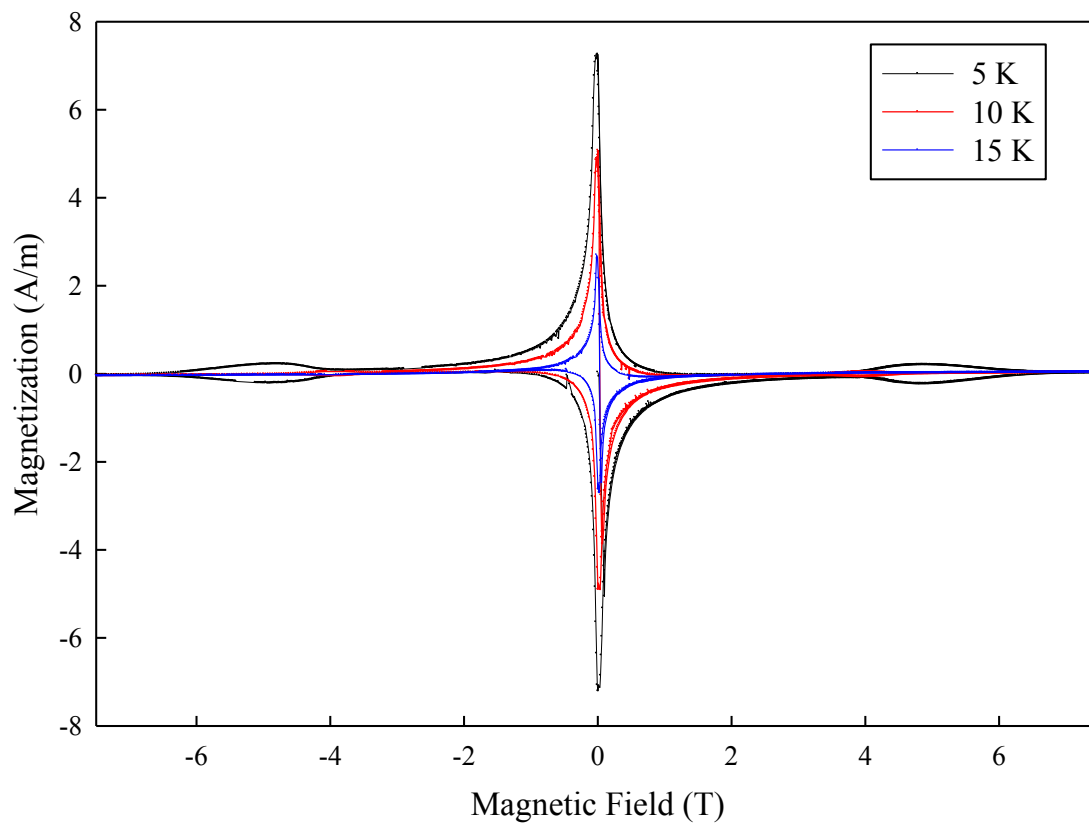


Figure 53. VSM M-H loop of 1700 °C Ingot

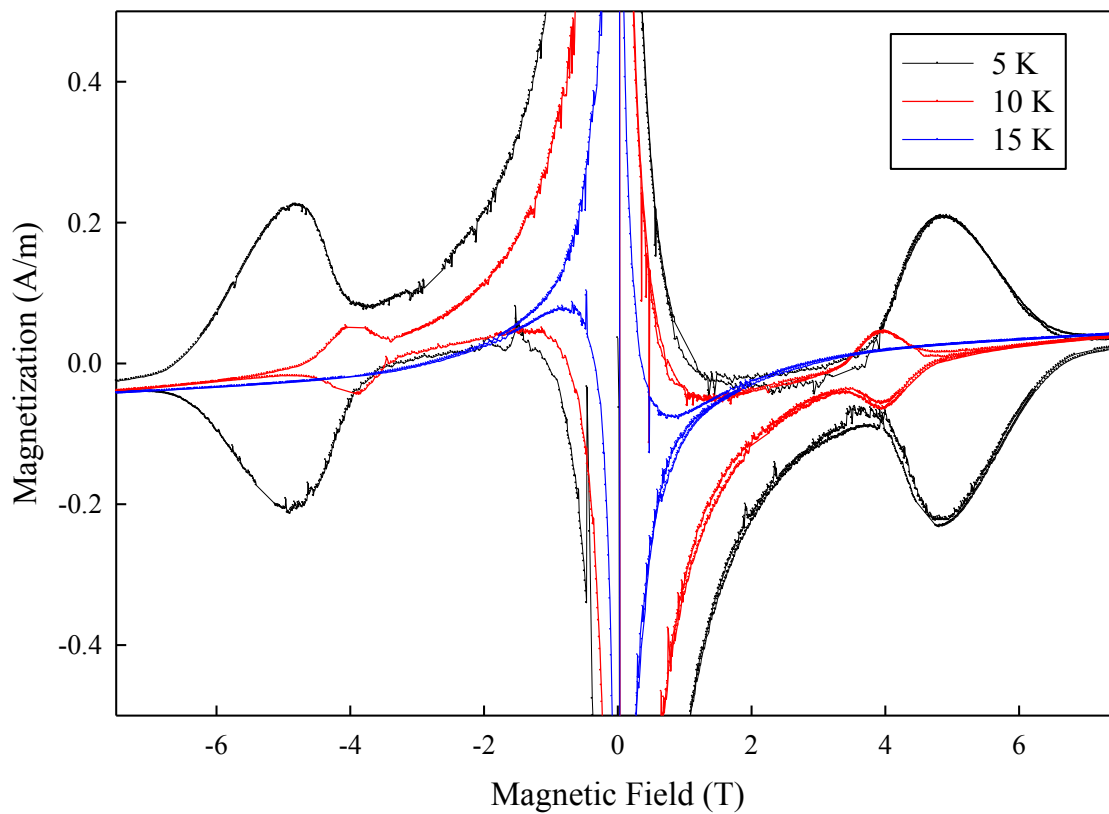


Figure 54. VSM M-H loop of 1700 °C Ingot (zoom)

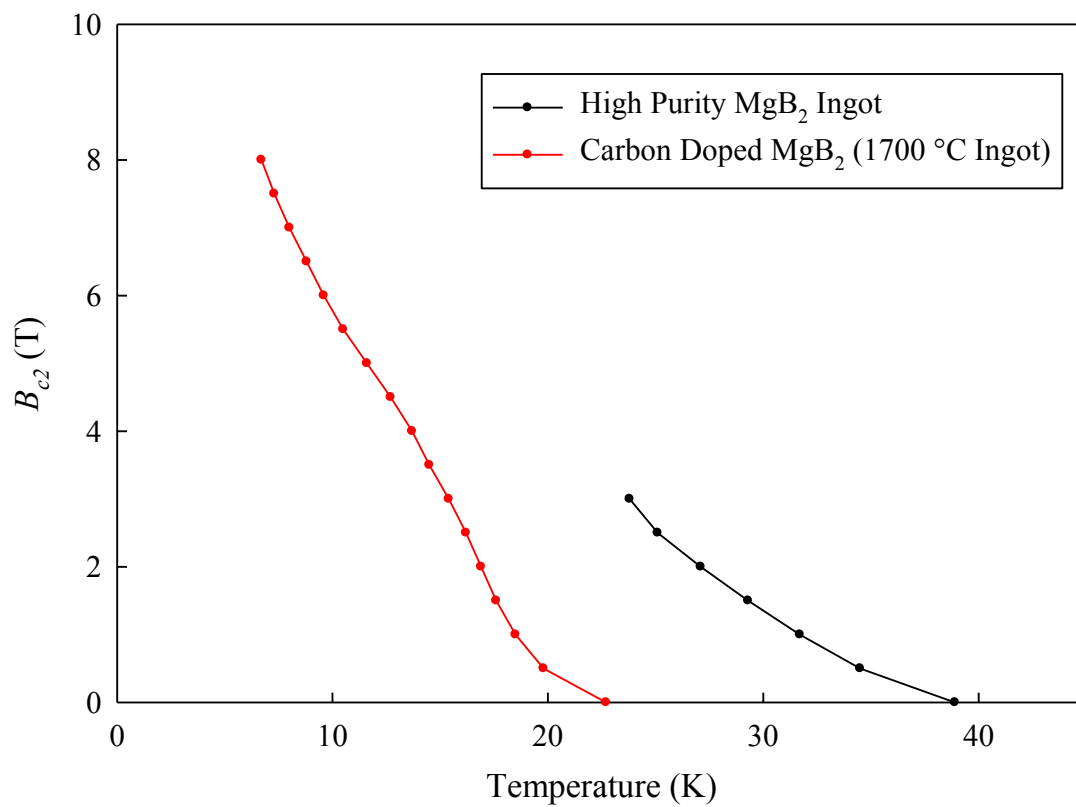


Figure 55. Upper Critical Field of Carbon Doped MgB₂ and pure MgB₂

SUMMARY AND CONCLUSIONS

The DSC study of the low temperature formation of MgB_2 from Mg/B and MgH_2/B powders indicated the sensitivity of the reaction to the purity of the magnesium powder. The Mg/B powder mixture had a low temperature exothermic reaction at ~ 425 °C that was initiated by the decomposition of Mg(OH)_2 on the surface of the Mg. The reaction of Mg/B with Mg from MgH_2 only had one exothermic reaction event that began at ~ 575 - 600 °C. A Kissinger analysis using DSC data with different ramp rates was used to estimate an apparent activation energy of ~ 239 kJ/mole. However, the DSC instrument only measured the overall heat flow in the sample so this activation energy may encompass multiple reaction steps and hence multiple activation energies.

The limitations of low temperature synthesis led to the development of a high pressure induction furnace which made it possible to not only create better MgB_2 samples but also enabled the first measurement of the incongruent melting temperature of MgB_2 . This measurement used a custom implementation of the Smith Thermal Analysis (STA) method that was successfully demonstrated with Al and AlB_2 powder at standard pressure (0.1 MPa). The measurement with MgB_2 powder at high pressure (10 MPa) did not provide a clear measurement of the incongruent melting temperature, but it did indicate a definite transition similar to the AlB_2 powder. The large amount of MgO contamination in the ingot from MgB_2 powder led to the use of elemental mixtures instead. Unfortunately, there were no successful STA runs using elemental mixtures of Mg and B, but a standard ramp/dwell/cool run of the high pressure furnace was successful at

detecting the incongruent melting temperature (peritectic) in MgB_2 at ~ 1445 °C using high purity boron. This value was based on a temperature ramp of 20 °C/min. so the actual peritectic temperature was probably even lower. A measurement was also made with a Mg/B elemental mixture using low purity boron, but the peritectic was at a higher temperature of ~ 1490 °C. The increase in the peritectic temperature was most likely due to a carbon impurity level in the boron of ~ 0.7 wt%.

The maximum carbon doping limit in MgB_2 was also studied. Carbon is known to substitute on the boron site in the MgB_2 structure and is the only dopant that significantly increases the upper critical field. Thus several samples were synthesized in the high pressure furnace using B_4C and Mg in order to determine the maximum amount of carbon that can dope into MgB_2 . Three samples were prepared at 1530 °C, 1600 °C and 1700 °C and they all had the same three phases: Mg, MgB_2C_2 and carbon doped MgB_2 . The presence of MgB_2C_2 indicated that the solubility limit for carbon in MgB_2 had been reached. Electron Probe Microanalysis at the University of Oregon confirmed that carbon was in the MgB_2 at ~ 5.9 at%. Further analysis with TEM indicated that the 1530 °C sample contained a significant amount of MgO inclusions. Also, measurements using A.C. Susceptibility and Vibrating Sample Magnetometry indicated that these samples may have contained small defects within the carbon doped MgB_2 that led to flux pinning effects at 5 K and 10 K.

Although this study was able to answer some basic questions regarding the materials science of MgB_2 , it also left many unanswered questions. For future studies, it would be beneficial to understand how the carbon doped ingot microstructure affects the

superconducting properties at high field. It may also be useful to study the MgB_2C_2 phase for any effects it may have on the carbon-doped MgB_2 phase. Finally, the high pressure furnace now makes it possible to synthesize much more homogeneous doped samples so a new investigation should be started that focuses on dopant solubility and dopant effects on superconducting properties.

APPENDIX A: SMITH THERMAL ANALYSIS PROTOCOL

Step 1: Both thermocouples (graphite and sample) were checked for continuity and polarity. Also, the thermocouple compensation wire was checked for polarity before bolting together the pressure vessel by making sure the red wire was the negative terminal on the thermocouple connectors. Another quick check was to use a cigarette lighter or handheld soldering iron to apply heat to the tip of the thermocouple and verify that the temperature increased. If the thermocouple wire were reversed, then the reading will decrease and an alarm will be initiated.

Step 2: After the vessel was bolted together, evacuated and backfilled with 99.998% argon, the induction power supply was connected to the copper connectors at the top of the vessel. Then the Haskris water chiller was started to check for leaks. The thermocouples were connected to Cu/Cu junctions in a deionized water ice bath in a small dewar (the Cu/Cu junctions were connected to the thermocouple inputs on the temperature controller). An ice bath was used as the cold junction reference since the on-board cold junction compensation circuit was erratic due to room temperature fluctuations. Also, the iTools software was started on the computer and used to establish communication with the temperature controller.

Step 3: After turning on the Lepel induction power supply, manual power was used to slowly heat up the graphite susceptor. The graphite thermocouple was then checked to make sure it was the PV input on the temperature controller (the graphite

thermocouple should respond faster to heating of the graphite susceptor). If the two thermocouples were mixed up, then the two connectors were swapped in the ice bath.

Step 4: After reaching a steady temperature, manual control was turned off and automatic control was turned on with a set point on the temperature controller close to whatever value had been reached under manual control.

Step 5: Once the temperature stabilized under automatic control, the auto-tuning algorithm was turned on to optimize the Proportional-Integral (PI) constants used in the Proportional-Integral-Derivative (PID) control algorithm. The derivative part of the algorithm was turned off since it sometimes caused instability. This step was skipped if auto-tuning had previously been used under similar conditions to obtain PI constants.

Step 6: Automatic control was turned off and manual control turned back on with roughly the same output as the previous step to keep the temperature roughly constant.

Step 7: The temperature difference between the sample and graphite was noted since it represented the “natural” equilibrium temperature difference. Ideally, the temperature difference would be zero but this can be difficult to achieve with induction heating (and it may depend on thermocouple placement). To change from temperature control to temperature difference control, the iTools software was used to subtract the sample temperature from the graphite temperature using an on-board MATH block. This temperature difference was then set as the input to the feedback control loop. Also, the feedback loop was changed from Reverse Acting to Direct Acting. Consult the user’s manual for how to make these changes on the Eurotherm 3504 controller.

Step 8: The iTools software was used to start OPC Scope which was used to log time/temperature data at one second intervals. The system was switched to automatic control and a temperature difference set point was entered. If the set point was the same as the natural temperature difference, then no heating or cooling would occur. However, if the set point was lower than the equilibrium value, then the system would ramp up in temperature. If the set point was higher, then the system would ramp down in temperature. The average heating or cooling rate is governed by how far the set point is from the natural temperature difference.

APPENDIX B: STANDARD RAMP/DWELL/COOL PROTOCOL

Steps 1-5: The protocol for steps 1-5 was the same as with the Smith Thermal Analysis Protocol (see above).

Step 6: Once the auto-tuning algorithm was finished, a program was entered for a ramp/dwell/cool sequence. Before the sequence was started, the set point was set to 0 °C since the controller reverts back to the pre-existing set point once the sequence is finished (i.e. if the set point was 1000 °C when the sequence started, then when the sequence finishes the controller will immediately try to go back to 1000 °C, hence it is better to change the set point to a low value before starting a sequence). Also, it is important that the ramp/dwell/cool cycle finish before the gas temperature reaches 75-80 °C, otherwise the power supply must be turned off so the gas temperature does not exceed the safe operating limits of the pressure vessel. In general, this means ramp rates of at least 10-20 °C/min. must be used on heating if high temperatures (>1500 °C) will be reached under pressure.

LIST OF REFERENCES

- [1] J. Nagamatsu, N. Nakagawa, T. Muranaka, Y. Zenitani, and J. Akimitsu, "Superconductivity at 39 K in magnesium diboride," *Nature*, vol. 410, no. 6824, pp. 63-64, 2001.
- [2] M. E. Jones and R. E. Marsh, "The Preparation and Structure of Magnesium Boride MgB₂," *J. Am. Chem. Soc.*, vol. 76, no. 5, pp. 1434-1436, 1954.
- [3] V. Russell, R. Hirst, F. A. Kanda, and A. J. King, "An X-ray study of the magnesium borides," *Acta Crystallographica*, vol. 6, no. 11-12, p. 870, 1953.
- [4] Y. Ma, Y. Wang, and A. R. Oganov, "Absence of superconductivity in the high-pressure polymorph of MgB₂," *Phys. Rev. B*, vol. 79, no. 5, p. 054101, 2009.
- [5] J. D. Jorgensen, D. G. Hinks, and S. Short, "Lattice properties of MgB₂ versus temperature and pressure," *Physical Review B*, vol. 63, no. 22, p. 224522, 2001.
- [6] J. M. An and W. E. Pickett, "Superconductivity of MgB₂: Covalent Bonds Driven Metallic," *Physical Review Letters*, vol. 86, no. 19, pp. 4366-4369, 2001.
- [7] J. Kortus, I. I. Mazin, K. D. Belashchenko, V. P. Antropov, and L. L. Boyer, "Superconductivity of Metallic Boron in MgB₂," *Physical Review Letters*, vol. 86, no. 20, pp. 4656-4659, 2001.
- [8] H. J. Choi, D. Roundy, H. Sun, M. L. Cohen, and S. G. Louie, "The origin of the anomalous superconducting properties of MgB₂," *Nature*, vol. 418, no. 6899, pp. 758-760, 2002.
- [9] K. D. Belashchenko, M. Schilfgaard, and V. P. Antropov, "Coexistence of covalent and metallic bonding in the boron intercalation superconductor MgB₂," *Physical Review B*, vol. 64, no. 9, p. 092503, 2001.
- [10] H. Mori, S. Lee, A. Yamamoto, S. Tajima, and S. Sato, "Electron density distribution in a single crystal of Mg_{1-x}B₂ [x=0.045(5)]," *Physical Review B*, vol. 65, no. 9, p. 092507, 2002.
- [11] S. L. Bud'ko, G. Lapertot, C. Petrovic, C. E. Cunningham, N. Anderson, and P. C. Canfield, "Boron Isotope Effect in Superconducting MgB₂," *Physical Review Letters*, vol. 86, no. 9, pp. 1877-1880, 2001.
- [12] D. G. Hinks and J. D. Jorgensen, "The isotope effect and phonons in MgB₂," *Physica C*, vol. 385, no. 1-2, pp. 98-104, 2003.
- [13] Y. Eltsev et al., "Anisotropic resistivity and Hall effect in MgB₂ single crystals," *Physical Review B*, vol. 66, no. 18, p. 180504, 2002.
- [14] U. Welp et al., "Superconducting transition and phase diagram of single-crystal MgB₂," *Physical Review B*, vol. 67, no. 1, p. 012505, Jan. 2003.
- [15] U. Welp et al., "Superconducting phase diagram of single-crystal MgB₂," *Physica C*, vol. 385, no. 1-2, pp. 154-161, 2003.
- [16] M. Angst et al., "Anisotropy of the superconducting state properties and phase diagram of MgB₂ by torque magnetometry on single crystals," *Physica C*, vol. 385, no. 1-2, pp. 143-153, 2003.

- [17] V. G. Kogan and S. L. Bud'ko, "Anisotropy parameters of superconducting MgB₂," *Physica C*, vol. 385, no. 1-2, pp. 131-142, 2003.
- [18] M. Eisterer, "Magnetic properties and critical currents of MgB₂," *Superconductor Science and Technology*, vol. 20, no. 12, p. R47-R73, 2007.
- [19] D. C. Larbalestier et al., "Strongly linked current flow in polycrystalline forms of the superconductor MgB₂," *Nature*, vol. 410, no. 6825, pp. 186-189, 2001.
- [20] M. M. R. Naslain, A. Guette, and M. Barret, "Sur le diborure et le tétraborure de magnésium. Considérations cristallographiques sur les tétraborures," *Journal of Solid State Chemistry*, vol. 8, no. 1, pp. 68-85, 1973.
- [21] A. Pediaditakis, M. Schroeder, V. Sagawe, T. Ludwig, and H. Hillebrecht, "Binary Boron-Rich Borides of Magnesium: Single-Crystal Investigations and Properties of MgB₇ and the New Boride Mg₅B₄₄," *Inorg. Chem.*, vol. 49, no. 23, pp. 10882-10893, 2010.
- [22] A. Guette, M. Barret, R. Naslain, P. Hagenmuller, L.-E. Tergenius, and T. Lundström, "Crystal structure of magnesium heptaboride Mg₂B₁₄," *Journal of The Less-Common Metals*, vol. 82, no. C, pp. 325-334, 1981.
- [23] V. Adasch, K. Hess, T. Ludwig, N. Vojteer, and H. Hillebrecht, "Synthesis and crystal structure of MgB₁₂," *Journal of Solid State Chemistry*, vol. 179, no. 9, pp. 2916-2926, 2006.
- [24] S. Brutti, M. Colapietro, G. Balducci, L. Barba, P. Manfrinetti, and A. Palenzona, "Synchrotron powder diffraction Rietveld refinement of MgB₂₀ crystal structure," *Intermetallics*, vol. 10, no. 8, pp. 811-817, 2002.
- [25] V. Adasch, K. Hess, T. Ludwig, N. Vojteer, and H. Hillebrecht, "Synthesis, crystal growth and structure of Mg containing β -rhombohedral boron: MgB_{17.4}," *Journal of Solid State Chemistry*, vol. 179, no. 9, pp. 2900-2907, 2006.
- [26] G. Giunchi, L. Malpezzi, and N. Masciocchi, "A new crystalline phase of the boron-rich metal-boride family: the Mg₂B₂₅ species," *Solid State Sciences*, vol. 8, no. 10, pp. 1202-1208, 2006.
- [27] Y. G. Zhao et al., "Influence of the starting composition Mg_{1-x}B₂ on the structural and superconducting properties of the MgB₂ phase," *Physica C*, vol. 366, no. 1, pp. 1-5, 2001.
- [28] A. Serquis et al., "Influence of microstructures and crystalline defects on the superconductivity of MgB₂," *Journal of Applied Physics*, vol. 92, no. 1, pp. 351-356, 2002.
- [29] A. Serquis, Y. T. Zhu, E. J. Peterson, J. Y. Coulter, D. E. Peterson, and F. M. Mueller, "Effect of lattice strain and defects on the superconductivity of MgB₂," *Applied Physics Letters*, vol. 79, no. 26, pp. 4399-4401, Dec. 2001.
- [30] D. G. Hinks, J. D. Jorgensen, H. Zheng, and S. Short, "Synthesis and stoichiometry of MgB₂," *Physica C*, vol. 382, no. 2-3, pp. 166-176, 2002.
- [31] E. H. Copland and N. S. Jacobson, "Thermodynamic activity measurements with Knudsen cell mass spectrometry," *The Electrochemical Society Interface*, vol. 10, no. 2, pp. 28-31, 2001.

- [32] S. Brutti, A. Ciccioli, G. Balducci, G. Gigli, P. Manfrinetti, and A. Palenzona, "Vaporization thermodynamics of MgB₂ and MgB₄," *Applied Physics Letters*, vol. 80, no. 16, pp. 2892-2894, 2002.
- [33] S. Brutti, G. Balducci, G. Gigli, A. Ciccioli, P. Manfrinetti, and A. Palenzona, "Thermodynamic and kinetic aspects of decomposition of MgB₂ in vacuum: Implications for optimization of synthesis conditions," *Journal of Crystal Growth*, vol. 289, no. 2, pp. 578-586, 2006.
- [34] G. Balducci et al., "Thermodynamics of the intermediate phases in the Mg-B system," *Journal of Physics and Chemistry of Solids*, vol. 66, no. 2-4, pp. 292-297, 2005.
- [35] L. P. Cook, R. Klein, W. Wong-Ng, Q. Huang, R. A. Ribeiro, and P. C. Canfield, "Thermodynamics of MgB₂ by calorimetry and Knudsen thermogravimetry," *IEEE Transactions on Applied Superconductivity*, vol. 15, no. 2, pp. 3227-3229, 2005.
- [36] M. Chase, "NIST-JANAF thermochemical tables, 4th edition," *J. Phys. Chem. Ref. Data*, vol. 9, 1998.
- [37] G. K. Moiseev and A. L. Ivanovskii, "Thermodynamic Properties and Thermal Stability of Magnesium Borides," *Inorganic Materials*, vol. 41, no. 10, pp. 1061-1066, 2005.
- [38] Z. Liu, Y. Zhong, D. G. Schlom, X. X. Xi, and Q. Li, "Computational thermodynamic modeling of the Mg-B system," *Calphad*, vol. 25, no. 2, pp. 299-303, 2001.
- [39] S. Kim, D. S. Stone, J. Cho, C. Jeong, C. Kang, and J. Bae, "Phase stability determination of the Mg-B binary system using the CALPHAD method and ab initio calculations," *Journal of Alloys and Compounds*, vol. 470, no. 1-2, pp. 85-89, 2009.
- [40] P. C. Canfield et al., "Superconductivity in Dense MgB₂ Wires," *Physical Review Letters*, vol. 86, no. 11, pp. 2423-2426, 2001.
- [41] J. D. DeFouw and D. C. Dunand, "Mechanisms and kinetics of MgB₂ synthesis from boron fibers," *Acta Materialia*, vol. 56, no. 19, pp. 5751-5763, 2008.
- [42] B. A. Glowacki, M. Majoros, M. Vickers, J. E. Evetts, Y. Shi, and I. McDougall, "Superconductivity of powder-in-tube MgB₂ wires," *Superconductor Science and Technology*, vol. 14, no. 4, p. 193, 2001.
- [43] S. D. Bohnenstiehl et al., "Wind and React MgB₂ Rotor Coils," *AIP Conference Proceedings*, vol. 986, no. 1, pp. 382-387, 2008.
- [44] C. E. J. Dancer, P. Mikheenko, A. Bevan, J. S. Abell, R. I. Todd, and C. R. M. Grovenor, "A study of the sintering behaviour of magnesium diboride," *Journal of the European Ceramic Society*, vol. 29, no. 9, pp. 1817-1824, 2009.
- [45] T. Wenzel, K. G. Nickel, J. Glaser, H.-J. Meyer, D. Eyidi, and O. Eibl, "Electron probe microanalysis of Mg-B compounds: stoichiometry and heterogeneity of superconductors," *Physica Status Solidi (a)*, vol. 198, no. 2, pp. 374-386, 2003.
- [46] D. Eyidi, O. Eibl, T. Wenzel, K. G. Nickel, M. Giovannini, and A. Saccone, "Phase analysis of superconducting polycrystalline MgB₂," *Micron*, vol. 34, no. 2, pp. 85-96, 2003.
- [47] S. Zhou, Y. Zhang, and S. X. Dou, "Effects of B₂O₃ in precursor B powder on MgB₂ critical current density," *Physica C*, vol. 470, no. 1, p. S635-S636, 2010.

- [48] J. Jiang, B. J. Senkowicz, D. C. Larbalestier, and E. E. Hellstrom, "Influence of boron powder purification on the connectivity of bulk MgB₂," *Superconductor Science and Technology*, vol. 19, no. 8, p. L33, 2006.
- [49] G. Giunchi, "The Superconducting Properties of High Density Bulk MgB₂ Obtained by Reactive Liquid Mg Infiltration," *AIP Conference Proceedings*, vol. 824, no. 1, pp. 813-819, 2006.
- [50] R. A. Ribeiro, S. L. Bud'ko, C. Petrovic, and P. C. Canfield, "Effects of boron purity, Mg stoichiometry and carbon substitution on properties of polycrystalline MgB₂," *Physica C*, vol. 385, no. 1-2, pp. 16-23, 2003.
- [51] S. K. Chen, K. A. Yates, M. G. Blamire, and J. L. MacManus-Driscoll, "Strong influence of boron precursor powder on the critical current density of MgB₂," *Superconductor Science and Technology*, vol. 18, no. 11, p. 1473, 2005.
- [52] R. Schmitt, J. Glaser, T. Wenzel, K. G. Nickel, and H.-J. Meyer, "A reactivity study in the Mg-B system reaching for an improved synthesis of pure MgB₂," *Physica C*, vol. 436, no. 1, pp. 38-42, 2006.
- [53] X. X. Xi, "MgB₂ thin films," *Superconductor Science and Technology*, vol. 22, no. 4, p. 043001, 2009.
- [54] X. X. Xi et al., "MgB₂ thin films by hybrid physical-chemical vapor deposition," *Physica C*, vol. 456, no. 1-2, pp. 22-37, 2007.
- [55] X. X. Xi et al., "In situ growth of MgB₂ thin films by hybrid physical-chemical vapor deposition," *Applied Superconductivity, IEEE Transactions on*, vol. 13, no. 2, pp. 3233-3237, 2003.
- [56] Dai et al., "High-field properties of carbon-doped MgB₂ thin films by hybrid physical-chemical vapor deposition using different carbon sources," *Superconductor Science and Technology*, vol. 24, no. 12, p. 125014, 2011.
- [57] J. Karpinski et al., "MgB₂ single crystals: high pressure growth and physical properties," *Superconductor Science and Technology*, vol. 16, no. 2, p. 221, 2003.
- [58] J. Karpinski et al., "Single crystal growth of MgB₂ and thermodynamics of Mg-B-N system at high pressure," *Physica C*, vol. 385, no. 1-2, pp. 42-48, 2003.
- [59] J. Karpinski, N. D. Zhigadlo, S. Katrych, R. Puzniak, K. Rogacki, and R. Gonnelli, "Single crystals of MgB₂: Synthesis, substitutions and properties," *Physica C*, vol. 456, no. 1-2, pp. 3-13, 2007.
- [60] S. Lee, "Crystal growth of MgB₂," *Physica C*, vol. 385, no. 1-2, pp. 31-41, 2003.
- [61] S. Lee, A. Yamamoto, H. Mori, Y. Eltsev, T. Masui, and S. Tajima, "Single crystals of MgB₂ superconductor grown under high-pressure in Mg-B-N system," *Physica C*, vol. 378-381, no. 1, pp. 33-37, 2002.
- [62] D. Souptel, G. Behr, W. Löser, W. Kopylov, and M. Zinkevich, "Crystal growth of MgB₂ from Mg-Cu-B melt flux and superconducting properties," *Journal of Alloys and Compounds*, vol. 349, no. 1-2, pp. 193-200, 2003.
- [63] N. R. Werthamer, E. Helfand, and P. C. Hohenberg, "Temperature and Purity Dependence of the Superconducting Critical Field, H_{c2}. III. Electron Spin and Spin-Orbit Effects," *Physical Review*, vol. 147, no. 1, pp. 295-302, 1966.
- [64] R. J. Cava, H. W. Zandbergen, and K. Inumaru, "The substitutional chemistry of MgB₂," *Physica C*, vol. 385, no. 1-2, pp. 8-15, 2003.

- [65] S. Margadonna, K. Prassides, I. Arvanitidis, M. Pissas, G. Papavassiliou, and A. N. Fitch, "Crystal structure of the $Mg_{1-x}Al_xB_2$ superconductors near $x=0.5$," *Phys. Rev. B*, vol. 66, no. 1, p. 014518, 2002.
- [66] S. X. Dou et al., "Enhancement of the critical current density and flux pinning of MgB_2 superconductor by nanoparticle SiC doping," *Applied Physics Letters*, vol. 81, no. 18, pp. 3419-3421, 2002.
- [67] E. W. Collings, M. D. Sumption, M. Bhatia, M. A. Susner, and S. D. Bohnenstiehl, "Prospects for improving the intrinsic and extrinsic properties of magnesium diboride superconducting strands," *Superconductor Science and Technology*, vol. 21, no. 10, p. 103001, 2008.
- [68] J. H. Kim, S. Zhou, M. S. A. Hossain, A. V. Pan, and S. X. Dou, "Carbohydrate doping to enhance electromagnetic properties of MgB_2 superconductors," *Applied Physics Letters*, vol. 89, no. 14, pp. 142505-3, Oct. 2006.
- [69] J. H. Kim et al., "Systematic study of a $MgB_2 + C_4H_6O_5$ superconductor prepared by the chemical solution route," *Superconductor Science and Technology*, vol. 20, no. 7, p. 715, 2007.
- [70] R. A. Ribeiro, S. L. Bud'ko, C. Petrovic, and P. C. Canfield, "Carbon doping of superconducting magnesium diboride," *Physica C*, vol. 384, no. 3, pp. 227-236, 2003.
- [71] M. Avdeev, J. D. Jorgensen, R. A. Ribeiro, S. L. Bud'ko, and P. C. Canfield, "Crystal chemistry of carbon-substituted MgB_2 ," *Physica C*, vol. 387, no. 3-4, pp. 301-306, 2003.
- [72] J. V. Marzik et al., "Plasma synthesized doped B powders for MgB_2 superconductors," *Physica C*, vol. 423, no. 3-4, pp. 83-88, 2005.
- [73] M. A. Susner et al., "Enhanced critical fields and superconducting properties of pre-doped B powder-type MgB_2 strands," *Superconductor Science and Technology*, vol. 24, no. 1, p. 012001, 2011.
- [74] J. Karpinski et al., " MgB_2 single crystals substituted with Li and with Li-C: Structural and superconducting properties," *Physical Review B*, vol. 77, no. 21, p. 214507, 2008.
- [75] R. H. T. Wilke et al., "Superconductivity in MgB_2 doped with Ti and C," *Physica C*, vol. 418, no. 3-4, pp. 160-167, 2005.
- [76] Meng, R. L. et al., "The synthesis and performance of MgB_2 ," *Materials Research Society Symposia Proceedings*, vol. 689, pp. 39-46, 2002.
- [77] W. Goldacker, S. I. Schlachter, B. Obst, and M. Eisterer, "In situ MgB_2 round wires with improved properties," *Superconductor Science and Technology*, vol. 17, no. 9, p. S490, 2004.
- [78] J. H. Kim, W. K. Yeoh, M. J. Qin, X. Xu, and S. X. Dou, "The doping effect of multiwall carbon nanotube on MgB_2/Fe superconductor wire," *Journal of Applied Physics*, vol. 100, no. 1, p. 013908, 2006.
- [79] "E698 - Standard Test Method for Arrhenius Kinetic Constants for Thermally Unstable Materials Using Differential Scanning Calorimetry and the Flynn/Wall/Ozawa Method." ASTM, 2011.

- [80] J. F. Smith and R. L. Smythe, "Vapor pressure measurements over calcium, magnesium and their alloys and the thermodynamics of formation of CaMg₂," *Acta Metallurgica*, vol. 7, no. 4, pp. 261-267, 1959.
- [81] P. J. Anderson and R. F. Horlock, "Thermal decomposition of magnesium hydroxide," *Trans. Faraday Soc.*, vol. 58, pp. 1993-2004, 1962.
- [82] H. E. Kissinger, "Variations of Peak Temperature with Heating Rate in Differential Thermal Analysis," *Journal of Research of the National Bureau of Standards*, vol. 57, no. 4, pp. 217-221, 1956.
- [83] H. E. Kissinger, "Reaction Kinetics in Differential Thermal Analysis," *Analytical Chemistry*, vol. 29, no. 11, pp. 1702-1706, 1957.
- [84] J. O. Bockris, J. L. White, and J. D. Mackenzie, Eds., *Physicochemical Measurements at High Temperatures*. New York, NY: Academic Press, Inc., 1959.
- [85] "E230/E230M - Standard Specification and Temperature-Electromotive Force (emf) Tables for Standardized Thermocouples." ASTM, 2011.
- [86] C. S. Smith, "A simple method of thermal analysis permitting quantitative measurements of specific and latent heats," *Trans. Am. Inst. Met. Eng.*, vol. 137, pp. 236-245, 1940.
- [87] A. Saccone, D. Macciò, J. A. J. Robinson, F. H. Hayes, and R. Ferro, "Smith thermal analysis of selected Pr-Mg alloys," *Journal of Alloys and Compounds*, vol. 317-318, pp. 497-502, 2001.
- [88] A. Saccone, D. Macciò, S. Delfino, F. H. Hayes, and R. Ferro, "Mg-Ce Alloys. Experimental investigation by Smith thermal analysis," *Journal of Thermal Analysis and Calorimetry*, vol. 66, no. 1, pp. 47-57, 2001.
- [89] P. J. Horrocks, F. H. Hayes, and M. H. Rand, "Phase diagram and thermodynamics of the indium-cadmium system," *Calphad*, vol. 14, no. 2, pp. 185-191, 1990.
- [90] P. J. Horrocks, F. H. Hayes, and N. D. Moulson, "A Smith thermal analysis and DSC study of the In-Cd system," *Thermochimica Acta*, vol. 204, no. 1, pp. 25-33, 1992.
- [91] F. H. Hayes, R. D. Longbottom, E. Ahmad, and G. Chen, "On the Al-Si, Al-Ge, and Al-Ge-Si systems and their application to brazing in high power semiconductor devices," *Journal of Phase Equilibria*, vol. 14, no. 4, pp. 425-431, 1993.
- [92] F. H. Hayes, W. T. Chao, and J. A. J. Robinson, "Phase diagrams of (gold+binary solder) ternary alloy systems by smith thermal analysis," *Journal of Thermal Analysis and Calorimetry*, vol. 42, no. 4, pp. 745-758, 1994.
- [93] W. C. Hagel, G. M. Pound, and R. F. Mehl, "Calorimetric study of the austenite: pearlite transformation," *Acta Metallurgica*, vol. 4, no. 1, pp. 37-46, 1956.
- [94] R. Ferro and A. Saccone, "Thermal analysis and alloy phase diagrams," *Thermochimica Acta*, vol. 418, no. 1-2, pp. 23-32, 2004.
- [95] R. Ferro, G. Cacciamani, and G. Borzone, "Remarks about data reliability in experimental and computational alloy thermochemistry," *Intermetallics*, vol. 11, no. 11-12, pp. 1081-1094, 2003.

- [96] E. L. Charsley, P. G. Laye, G. M. B. Parkes, and J. J. Rooney, "Development and applications of a sample controlled DSC system," *Journal of Thermal Analysis and Calorimetry*, vol. 105, no. 2, pp. 699-703, 2011.
- [97] H. B. Dong and J. D. Hunt, "A Novel Single-pan Scanning Calorimeter. Measurement of thermophysical properties of metallic alloys," *Journal of Thermal Analysis and Calorimetry*, vol. 64, no. 1, pp. 341-350, 2001.
- [98] O. Sorensen and J. Rouquerol, *Sample Controlled Thermal Analysis: Origin, Goals, Multiple Forms, Applications and Future*. Springer, 2004.
- [99] D. Mirković, J. Gröbner, R. Schmid-Fetzer, O. Fabrichnaya, and H.-L. Lukas, "Experimental study and thermodynamic re-assessment of the Al-B system," *Journal of Alloys and Compounds*, vol. 384, no. 1-2, pp. 168-174, 2004.
- [100] A. Prince, *Alloy Phase Equilibria*. Elsevier, 1966.
- [101] W. J. Boettinger and U. R. Kattner, "On differential thermal analyzer curves for the melting and freezing of alloys," *Metallurgical and Materials Transactions A*, vol. 33, no. 6, pp. 1779-1794, 2002.
- [102] J. H. Westbrook and D. L. Wood, "'PEST' degradation in beryllides, silicides, aluminides, and related compounds," *Journal of Nuclear Materials*, vol. 12, no. 2, pp. 208-215, 1964.